UNIVERSITY OF CALIFORNIA
RIVERSIDE

Molecular Beam Epitaxy Growth of Hexagonal Boron Nitride/Graphene Heterostructures, Hexagonal Boron Nitride Layers and Cubic Boron Nitride Nanodots

A Dissertation submitted in partial satisfaction
of the requirements for the degree of

Doctor of Philosophy

in

Materials Science and Engineering

by

Alireza Khanaki

December 2017

Dissertation Committee:
Dr. Jianlin Liu, Chairperson
Dr. Elaine Haberer
Dr. Cengiz Ozkan

The Dissertation of Alireza Khanaki is approved:

Committee Chairperson

University of California, Riverside

ACKNOWLEDGEMENTS

I would like to express the deepest appreciation to my advisor, Prof. Jianlin Liu, who has the attitude and the substance of a genius. He continually and convincingly conveyed a spirit of hardworking and adventure in regard to research and scholarship. Without his guidance and persistent help this dissertation would not have been possible. Besides my advisor, I would like to thank my final dissertation defense committee members, Dr. Elaine Haberer and Dr. Cengiz Ozkan, for their time, insightful comments and encouragements.

With a special mention to my friends and fellow labmates in the Quantum Structures Laboratory: Dr. Zheng Zuo, Dr. Zhongguang Xu, Dr. Renjing Zheng, Dr. Monzur Morshed, Dr. Mohammad Suja, Dr. Sunayna Bashar, Dr. Longxing Su, Mr. Hao Tian, Mr. Yanwei He, Mrs. Zhenjun Cui, and Mr. Wenhao Shi who helped me a lot during my PhD studies. It was fantastic to work with every one of you. In addition, I would like to thank Dr. Roger Lake and Mr. Protik Das for their consistent support of my project through simulation studies. And, special thanks to Mr. Mike Longerborne and Dr. Jian-Guo Zheng for being always helpful in dealing with difficult technical/research situations. I am also grateful to the following university staff: William Bingham, Lorena Roman, Jeff Lefler, Stan Sheldon, and Maggie Souder for helping me in every possible way.

Finally, I would like to thank my parents, brother and sister for their unconditional love and supports throughout the past four years. I am also very grateful to my uncle's family (Naser Khanaki and Shahnaz Tafreshi) and friends, in particular, Alireza Sohrabi and Mohammadreza Aminikashani who have supported me along the way.

Previously Published Material Acknowledgment:

1. The results in Chapter 1 were published in:

   1.1. Zheng R., Xu Z., **Khanaki A.**, Tian H., Zuo Z. and Liu J. Low-temperature growth of graphene on iron substrate by molecular beam epitaxy. *Thin Solid Films* **627** 39 (2017).

   1.2. Xu Z., Zheng R., **Khanaki**, **A.**, Zuo Z. and Liu J. Direct growth of graphene on in situ epitaxial hexagonal boron nitride flakes by plasma-assisted molecular beam epitaxy. *Appl. Phys. Lett.* **107** 213103 (2015).

   1.3. Zheng R., **Khanaki A.**, Cui. Y., Tian H., Xu Z. and Liu J. Precipitation growth of graphene under exfoliated hexagonal boron nitride to form heterostructures on cobalt substrate by molecular beam epitaxy. *Appl. Phys. Lett.* **111** 011903 (2017).

2. The results in Chapter 2 were published in:

   2.1. Zuo Z. Xu Z., Zheng R., **Khanaki A.**, Zheng J.-G. and Liu J. In-situ epitaxial growth of graphene/h-BN van der Waals heterostructures by molecular beam epitaxy. *Sci. Rep.* **5** 14760 (2015).

   2.2. Xu Z., **Khanaki A.**, Tian H., Zheng R., Zheng J.-G. and Liu J. Direct growth of hexagonal boron nitride/graphene heterostructures on cobalt foil substrates by plasma-assisted molecular beam epitaxy. *Appl. Phys. Lett.* **109** 043110 (2016).

   2.3. **Khanaki A.**, Tian H., Xu Z., Zheng R., Cui Z., He Y., Yang J. and Liu J. Effect of high carbon incorporation in Co substrates on the epitaxy of hexagonal boron

nitride/graphene heterostructures. *Accepted in Nanotechnology* (2017). https://doi.org/10.1088/1361-6528/aa9c58

3. The results in Chapter 3 were published or are under review in:

   3.1. Xu Z., Tian H., **Khanaki A.**, Zheng R., Suja M. and Liu J. Large-area growth of multi-layer hexagonal boron nitride on polished cobalt foils by plasma-assisted molecular beam epitaxy. *Sci. Rep.* **5** 43100 (2017).

   3.2. Tian H., **Khanaki A. (co-first author)**, Das P., Zheng R., He Y., Cui Z., Shi W., Xu Z., Lake R. and Liu, J. The role of carbon interstitials in transition metal substrates on controllable synthesis of high-quality large-area two-dimensional hexagonal boron nitride layers. *Under review in Nanoletter* (2017).

4. The results in Chapter 4 were published in:

   4.1 **Khanaki A.**, Xu Z., Tian H., Zheng R., Zuo Z., Zheng J.-G. and Liu J. Self-assembled cubic boron nitride nanodots. *Sci Rep*. **7** 4087 (2017).

I dedicate my dissertation work to
my parents (Mansour Khanaki and Nasrin Moazzen),
my brother (Mohammadreza khanaki) and my sister (Neda Khanaki)

ABSTRACT OF THE DISSERTATION

Molecular Beam Epitaxy Growth of Hexagonal Boron Nitride/Graphene Heterostructures, Hexagonal Boron Nitride Layers and Cubic Boron Nitride Nanodots

by

Alireza Khanaki

Doctor of Philosophy, Graduate Program in Materials Science and Engineering
University of California, Riverside, December 2017
Dr. Jianlin Liu, Chairperson

Low-dimensional materials continue to attract and involve the minds and labor of scientists and engineers around the world as they are offering a set of fascinating properties which can be controlled by composition, size, and morphology. In this thesis, our focus is to explore the growth and characterization of some of such low-dimensional materials with molecular beam epitaxy (MBE) method. A technologically relevant example of low-dimensional systems is two-dimensional (2D) materials including graphene (G) and h-BN. To date, it is still challenging to reliably grow high-quality uniform 2D h-BN and h-BN/G heterostructures in a wafer scale mainly due to their complicated growth process.

In this first project, i.e., Chapter 2, we perform a systematic study of h-BN/G heterostructure growth on cobalt (Co) foil substrate in an MBE system and investigate the growth mechanisms of individual G and h-BN layers in the structure. We demonstrate with the increase of C incorporation in Co, three distinct h-BN/G growth regions can be observed: (1) the C saturation is not attained at the growth temperature (900 °C) and G is grown only by precipitation during cooling process to form a “G network” underneath the h-BN film; (2) the Co substrate is just saturated by C atoms at the growth temperature and

a part of G growth occurs isothermally to form G islands and another part by precipitation, resulting in a non-uniform h-BN/G film; and region (3): a continuous layered G structure is formed at the growth temperature and precipitated C atoms add additional G layers to the system, leading to a uniform h-BN/G film. We show that in all three growth regions, a 3-hrs h-BN growth at 900 ºC leads to h-BN film with a thickness of 1~2 nm, regardless of the underneath G layers' thickness or morphology.

Following the growth of h-BN/G heterostructures, in the next project, i.e, Chapter 3, we demonstrate that the dissolution of C atoms into heated Co substrate can also facilitate the growth of 2D h-BN and alter its morphology from 2D layer-plus-3D islands to homogeneous 2D few-layers. A high breakdown electric field of 12.5 MV/cm was achieved for a continuous 3-layer h-BN. Density functional theory calculations reveal that the interstitial C atoms can increase the adsorption of B and N atoms on the Co (111) surface, and in turn, promote the growth of 2D h-BN.

In the last project, i.e., Chapter 4, we discuss the growth and characterization of another low-dimensional form of BN family materials, namely, cubic boron nitride nanodots (c-BN NDs) which offers a variety of novel opportunities in battery, biology, deep ultraviolet light emitting diodes, sensors, filters, and other optoelectronic applications. To date, the attempts towards producing c-BN NDs were mainly performed under extreme high-temperature/high-pressure conditions and resulted in c-BN NDs with micrometer sizes, a mixture of different BN phases, and containing process-related impurities/contaminants. To enhance device performance for those applications by taking advantage of size effect, pure, sub-100 nm c-BN NDs are necessary. In this chapter, we

demonstrate the self-assembled growth of sub-100 nm c-BN NDs on Co and Ni foil substrates by plasma-assisted MBE for the first time. We found that the nucleation, formation, and morphological properties of c-BN NDs can be closely correlated with the nature of substrate including catalysis effect, lattice-mismatch-induced strain, and roughness, and growth conditions, in particular, growth time and growth temperature. The mean lateral size of c-BN NDs on cobalt scales from 175 nm to 77 nm with the growth time. The growth mechanism of c-BN NDs on metal substrates is concluded to be Volmer-Weber (VW) mode. A simplified two-dimensional numerical modeling shows that the elastic strain energy plays a key role in determining the total formation energy of c-BN NDs on metals.

Table of Contents

List of Figures

List of Tables

Chapter 1: Introduction

1.1. Two-dimensional van der Waals materials

Richard P. Feynman inspired generations of scientists to explore "the bottom" during his lecture "There's Plenty of Room at the Bottom" [1]. With his questions such as "What could we do with layered structures with just the right layers? Feynman was probably the first to motivate researchers all around the world studying the materials structure and properties at their finest scale. On the other hand, as the semiconductor industries are nearing the limits of performance improvements for the current technologies dominated by silicon (Si), there is a constant search for new, inexpensive and nontraditional materials whose properties can be controlled by the electric field. As a result, a tremendous amount of research, funding and resources have been invested to explore novel nanoscale materials with unprecedented properties and applications.

One prominent category of these newly discovered materials is two-dimensional (2D) van der Waals (vdW) materials. 2D vdW (or 2D for short) materials are crystalline materials consisting of a single or few layers of atoms (consisting of two or more covalently bonding elements) [2]. This layered structure has strong in-plane chemical bonds and weak interaction in the out-of-plane direction (i.e., among different layers), which makes it possible to directly grow or cleave bulk materials to prepare monolayers or few-layers of most 2D materials. Many of these materials are stable at ambient conditions, and there are strategies for handling those that are not. Surprisingly, the properties of such 2D materials are often very different from those of their 3D counterparts. The first 2D material to be

included is graphene, a zero-overlap semimetal [3]. The family of 2D crystals has grown to include metals (e.g., $NbSe_2$), semiconductors (e.g., MoS_2), and insulators [e.g., hexagonal boron nitride (h-BN)] [4]. Table 1 summarizes the family of 2D materials.

Table 1.1. 2D crystal family. The assorted colors indicate the different stability under ambient conditions (room temperature in air): blue (stable), green (probably stable), pink (stable in inert atmosphere), grey (little further information). 'Others' indicates that many other 2D crystals such as borides, carbides, nitrides and so forth [4] (adapted with copyright permission).

<table>
<tr><td>Graphene family</td><td>Graphene</td><td colspan="2">hBN
'white graphene'</td><td>BCN</td><td>Fluorographene</td><td>Graphene oxide</td></tr>
<tr><td rowspan="2">2D chalcogenides</td><td colspan="2" rowspan="2">MoS_2, WS_2, $MoSe_2$, WSe_2</td><td colspan="2" rowspan="2">Semiconducting dichalcogenides:
$MoTe_2$, WTe_2,
ZrS_2, $ZrSe_2$ and so on</td><td colspan="2">Metallic dichalcogenides:
$NbSe_2$, NbS_2, TaS_2, TiS_2, $NiSe_2$ and so on</td></tr>
<tr><td colspan="2">Layered semiconductors:
GaSe, GaTe, InSe, Bi_2Se_3 and so on</td></tr>
<tr><td rowspan="2">2D oxides</td><td>Micas, BSCCO</td><td colspan="2">MoO_3, WO_3</td><td rowspan="2" colspan="2">Perovskite-type:
$LaNb_2O_7$, $(Ca,Sr)_2Nb_3O_{10}$,
$Bi_4Ti_3O_{12}$, $Ca_2Ta_2TiO_{10}$ and so on</td><td>Hydroxides:
$Ni(OH)_2$, $Eu(OH)_2$ and so on</td></tr>
<tr><td>Layered Cu oxides</td><td colspan="2">TiO_2, MnO_2, V_2O_5,
TaO_3, RuO_2 and so on</td><td>Others</td></tr>
</table>

1.1.1. Graphene (G)

In 2004, Novoselov, Geim and colleagues were first to observe the electric field effect in a naturally occurring 2D material, named as graphene (G) [5]. Graphene refers to a single layer of carbon (C) atoms densely packed into a hexagonal structure (Figure 1.1). Novoselov and his colleagues demonstrated that it was indeed possible to isolate and measure electronic transport on individual layers of sp^2-hybridized C.

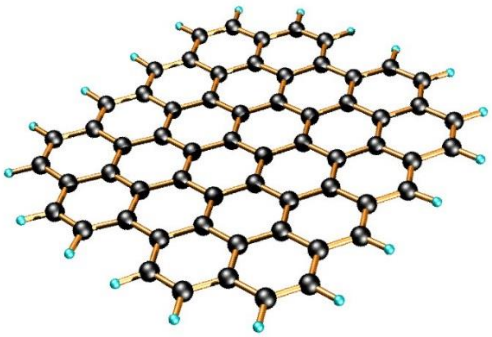

Figure 1.1. Idealized structure of a single G sheet (adapted from OpenStax CNX website).

This was a very exciting news to the scientific community since for a long period of time the theoreticians have predicted that G could not exist in nature by itself [6]. This, therefore, attracted researchers' attentions from all around the world to investigate properties of G. Although at the time G was probably meant to function only as the next generation nanomaterial in the modern electronics, thousands of research articles published later to show other exotic physiochemical properties of G and its applications in variety of

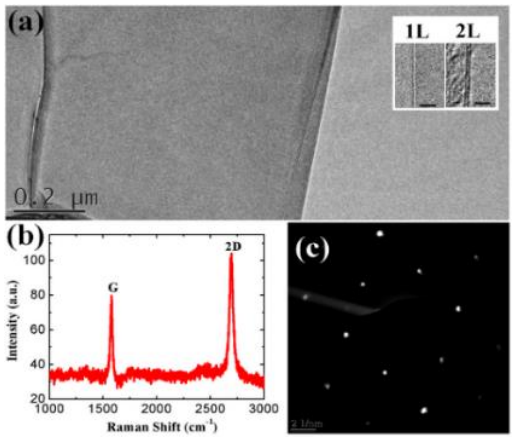

Figure 1.2. (a) Plan-view TEM image of G film grown by MBE. The inset shows the cross-sectional images of the single and bi-layer G, respectively (the scale bar is 2 nm), (b) Raman spectrum, (c) diffraction pattern of the G film, indicating high quality [9] (adapted with copyright permission).

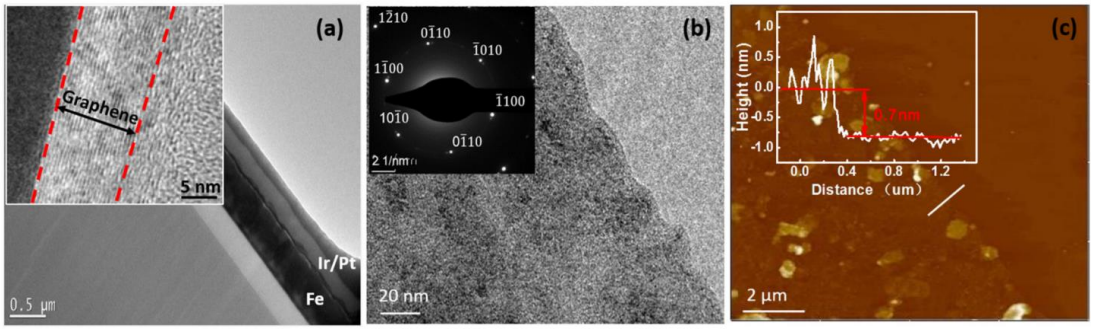

Figure 1.3. (a) Cross-sectional TEM image of G sample grown on Fe thin film substrate. The inset is a higher-magnification TEM image of a local thicker film region. (b) Plan-view TEM image of a transferred G film from the same sample. The inset is its SAED pattern. (c) AFM image of a transferred G film on SiO_2. The inset shows a line scan profile, indicating a graphene thickness of about 0.7 nm [10].

engineering and science fields [7,8]. In our group, we have demonstrated molecular beam epitaxy (MBE) growth of single/bilayer G on Co thin film [9] (Figure 1.2) and few-layer G on iron (Fe) thin film substrates [10] (Figure 1.3). Recently, Bolotin et. al showed that suspended G has an extremely high electrical conductivity which can be utilized in ultra-fast electronic devices [11]. Very recently, the methods towards an industrial-level production of high-quality G layers were established. Nevertheless, obtaining such high performances in many electronic devices requires G to be placed on an excellent insulating material [12,13].

1.1.2. Hexagonal boron nitride (h-BN)

It took researchers several years to discover that perfect complementary material to G is 2D hexagonal boron nitride (h-BN). H-BN is a single layer of boron (B) and nitrogen (N) atoms packed into a hexagonal structure (Figure 1.4), just like that of G. H-BN has a wide bandgap of ~5.9 eV, extremely flat surface (root mean square (RMS) roughness < 0.2

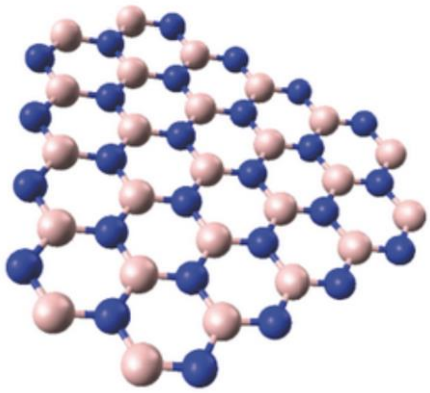

Figure 1.4. Idealized structure of a single hexagonal boron nitride (h-BN) sheet. Blue and pink atoms are representative of boron and nitrogen atoms (adapted from Blue Maze website).

nm) and free of dangling bond or surface charge trap, and excellent dielectric properties ($\varepsilon \approx 3–4$ and $V_{breakdown} \geq 3$ MV/cm) [14-18]. Furthermore, its very high thermal and chemical stabilities allow devices to operate under extreme conditions. These remarkable properties of 2D h-BN define this material as an excellent 2D dielectric and an effective wide bandgap semiconductor. As a 2D dielectric, its similar hexagonal lattice structure to G and other 2D materials such as transition metal dichalcogenides (TMD) has made h-BN an ideal candidate for all electronic devices where nanoscale supporting, insulating, capping, or gating layers are needed [19-21]. For example, early studies showed that G/h-BN stacked layers can outperform current Si-based electronics [22]. As a wide bandgap semiconductor, h-BN has potential applications for deep ultraviolet optics and high-voltage power electronics as well [23]. Therefore, it has become an immense interest among researchers to synthesize h-BN films and its heterostructures with other 2D materials such G (i.e., h-BN/G). Tremendous efforts have been made and much success has been achieved so far.

Nevertheless, unlike G, due to the multicomponent nature of h-BN structure (B and N), the reliable and large-scale synthesis of high-quality h-BN remains challenging.

1.1.3. Hexagonal boron nitride/graphene heterostructures (h-BN/G)

Two-dimensional (2D) materials offer a platform that allows creation of stacked or in-plane layers (so-called heterostructures) with a variety of properties (Figure 1.5) [19]. Since 2010, the methods of preparing h-BN/G heterostructures have become a hot topic of research and more and more reliable methods have been introduced [24,25]. Currently, most 2D heterostructures have been achieved by direct stacking of individual monolayer flakes/layers of different materials using methods such as wet transfer, dry transfer, and liquid phase exfoliation [26]. Although these methods can result in crystalline flakes and layered samples, the thickness and size of such samples are difficult to control. Therefore, all epitaxial vertical heterostructures with controllable thickness, size and well-defined

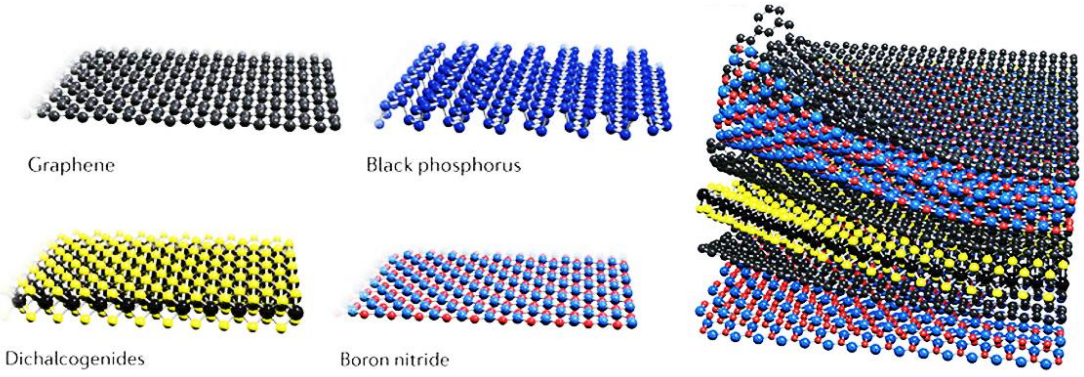

Figure 1.5. Formation of 2D heterostructures [24] (adapted with copyright permission).

orientation are indispensable toward practical applications. On this matter, both chemical vapor deposition (CVD) and molecular beam epitaxy (MBE) have been widely used for the growth of h-BN/G heterostructures on different substrates, especially, transition metals. Nevertheless, in-situ epitaxial growth of dissimilar van der Waals materials including h-BN/G heterostructures also remains challenging.

Besides the MBE growth of G and h-BN, our group has also demonstrated the MBE growth of h-BN/G vertical and lateral heterostructures. For instance, in our group, we achieved vertical h-BN/G heterostructures with different h-BN and G thicknesses, sizes and morphologies [27,28]. In addition, lateral h-BN/G heterostructure was also obtained in our group by first growing h-BN flakes on Co thin film substrate followed by the growth of G [29]. Interestingly, the growth rate of G on the metal substrate, h-BN flakes or existing G layer was found to be quite different under the same growth conditions, leading to lateral h-BN/G heterostructure. Figure 1.6 shows a Raman mapping of such a sample and the inset is the typical Raman spectra in respective regions, which clearly show the in-plane

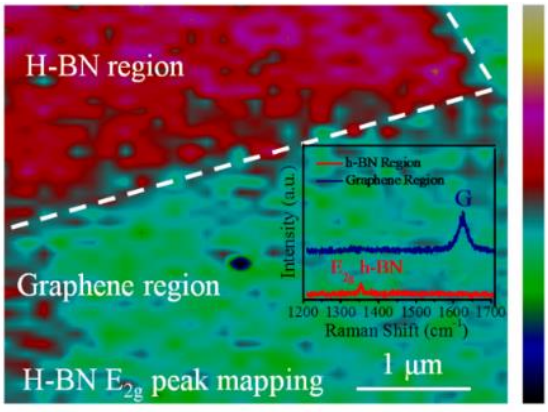

Figure 1.6. Raman mapping of a h-BN/G lateral heterostructure on Co thin film. The inset shows Raman spectra for respective regions [29].

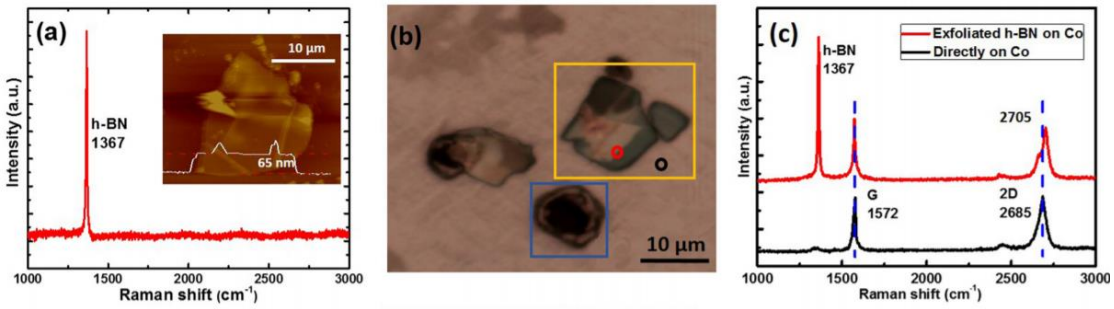

Figure 1.7. Characterizations of an as grown G/exfoliated h-BN heterostructure on Co thin film substrate. (a) Raman spectrum of a typical exfoliated h-BN flake on Co substrate. The inset is an AFM image of the substrate. (b) OM image of an as-grown sample. Yellow square and blue square are marked on the image to indicate the h-BN flake and heat-induced hole, respectively. (c) Raman spectra of as-grown sample, which are measured on the part shown in the red and black circles in (b) [30].

heterostructure characteristics. Recently, we have demonstrated G/h-BN vertical heterostructures by growing G onto the substrates which consist of exfoliated h-BN flakes on Co thin films in a MBE system [30] (Figure 1.7). We showed that under certain growth conditions, G can be grown in a gap between the Co thin film substrate and the h-BN flakes, making a thin G layer underneath thick h-BN flake (i.e., G/h-BN). Our growth method can provide a convenient path to produce G/h-BN heterostructures, which avoids high temperature and long duration needed for h-BN growth. Nevertheless, as of now, we are at about the same level as we were with G growth 10 years ago. Given the fast progress of G research and technology over the past years, we can expect similar advances in the production of such heterostructures (e.g., h-BN/G), making G-based devices more achievable.

1.2. Cubic boron nitride (c-BN)

Cubic boron nitride (c-BN) is another important allotrope of BN materials. It has sphalerite (zincblende) crystal structure (Figure 1.8), and is the second hardest material next to diamond [31]. C-BN was first synthesized in 1957, but it is only in the last 15 years that commercial production of c-BN has developed [32]. C-BN has a number of highly desirable mechanical, thermal, electrical, and optical properties. Because of this, there has been an extensive worldwide effort to synthesize thin films of c-BN. C-BN has significant technological potential for thin-film applications. Having a Vickers hardness of about 5000 kg mm^{-2}, and hence is a natural candidate for hard, protective coatings. It also has a high resistance to oxidation (at temperatures as high as 1300 ºC) which makes it even more attractive for tooling applications. C-BN is transparent in the infrared and visible parts of the spectrum, and thus is sought after as a protective coating for optical elements. Because of its wide bandgap (E_g = ~6 eV) and good thermal conductivity, c-BN also has the

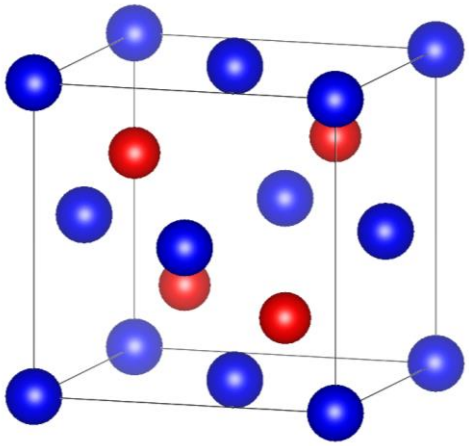

Figure 1.8. Idealized sphalerite structure of a cubic boron nitride (c-BN) unit cell. Blue and red atoms are representative of boron (B) and nitrogen (N) atoms, respectively.

potential for the high-temperature and high-power electronic applications. Furthermore, c-BN has been doped both p- and n-type, and can be passivated with an oxide layer [31,32]. In fact, a photodiode emitting in the UV has been made from a p-n junction formed in bulk c-BN. Table 1.2 compares some of the most important structural differences and properties of c-BN and h-BN [25,26,31,32].

Table 1.2. Comparison of crystalline c-BN and h-BN. Some properties of c-BN and h-BN within the basal planes (∥) and perpendicular to them (⊥) [25,26,31,32].

Material	c-BN	h-BN
Density (g/cm^3)	3.45	~2.1
Group of symmetry	F43m	$P6_3mmc$
Lattice constant, a	3.6157 A	2.5040 A
Mohs hardness (GPa)	9.5	1.5
Thermal conductivity (W/(m·K))	740	600 ∥, 30 ⊥
Thermal expansion (10^{-6}/°C)	1.2	−2.7 ∥, 38 ⊥
Dielectric constant (static)	7.1	5.06 ∥, 6.85 ⊥
Bandgap (eV)	~6.2	~5.8

1.3. Molecular beam epitaxy (MBE)

Molecular Beam Epitaxy (MBE) is a technique to grow high-quality uniform crystalline thin films of materials in an ultrahigh vacuum (UHV) conditions with a precise control of thickness, composition and morphology. It also provides unique capability to study crystal growth in real-time and on a sub-nanometer scale thanks to its in-situ unique

characterizations tools such as reflection high-energy electron diffraction (RHEED). MBE was invented in the late 1960s at Bell Telephone Laboratories (BTL) by J. R. Arthur and Alfred Y. Cho [33], and it has been widely used in the manufacture of semiconductor materials and devices. The first epitaxial GaAs films on GaAs substrates were grown by BTL researchers [34]. Since then, MBE research has produced many unique structures not available from alternative techniques, and MBE is now moving from the research laboratory to pilot production applications. MBE holds a clear advantage over other growth methods in terms of heterostructure growth and the non-equilibrium incorporation of dopants followed by thermal activation to achieve extrinsic semiconductors. It is also worth mentioning that vdW epitaxy was first demonstrated using the MBE process [35].

In MBE molecular or atomic beams (fluxes) of film constituents, or their compounds, are formed by evaporating high-purity materials from heated crucibles (effusion cells) or through plasma generators and/or gas crackers. The beams pass through shuttered apertures and impinge on a heated, mono- or poly-crystalline substrate where they react to form the semiconductor film. A separate cell is often used for each constituent. Film growth rate depends on the material arrival rates and substrate temperature. These can be adjusted very precisely, leading to extremely accurate film growth control. Substrate temperatures in MBE are substantially lower than alternative growth techniques, so interlayer diffusion is held to a minimum. Beams can also be shut off in less than a second using pneumatic shutters. In combination, these factors permit accurate and repeatable growth of epitaxial layers as thin as a few monolayers with very abrupt interfaces.

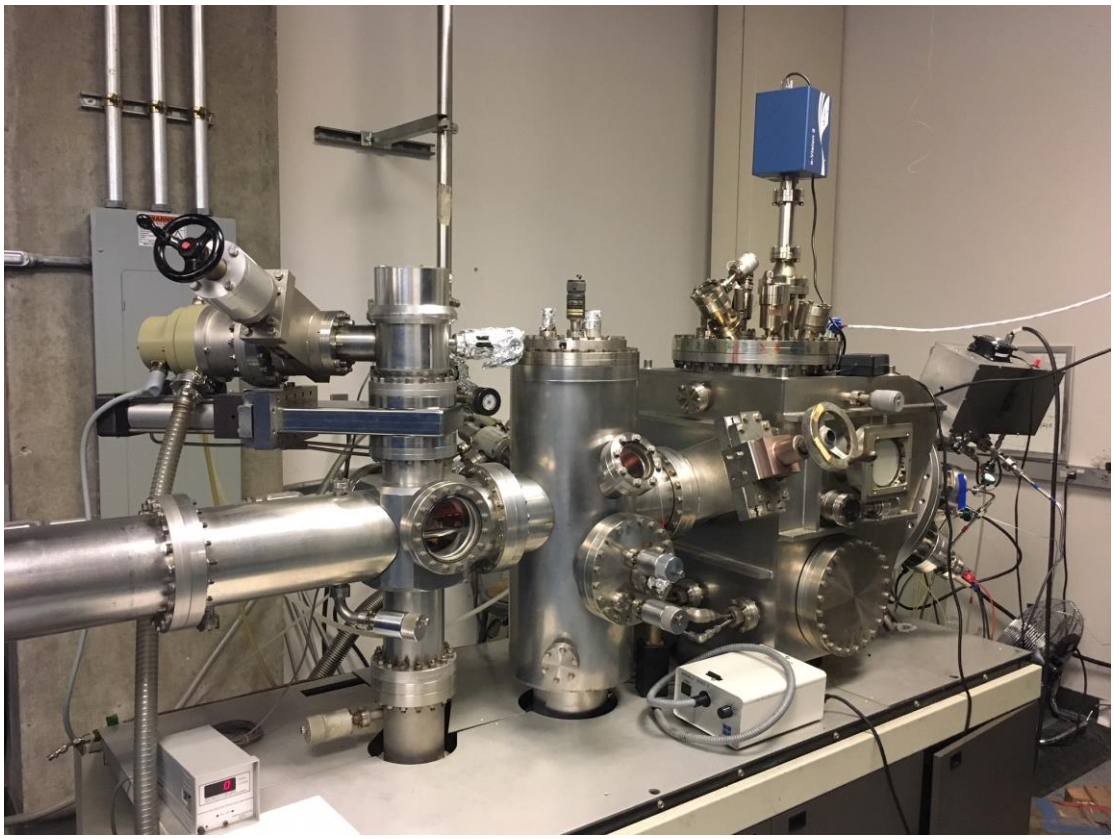

Figure 1.9. A modified 425B Perkin Elmer MBE system in Quantum Structures Laboratory (QSL) at University of California, Riverside (UCR).

In the Quantum Structures Laboratory (QSL), we use a PHI Model 425B Perkin Elmer MBE System (Figure 1.9). For G growth, we use acetylene (C_2H_2) gas and crack it through a gas thermal cracker. The cracker is a spring-shaped tungsten filament with a gas line coming through. A DC power supply provides power to heat the filament. The tip of the cracker can reach up to ~1200 °C. The bonds of C_2H_2 gas molecules that coming through the cracker are broken at high temperature, and C atoms impinge onto the heated substrate for epitaxial G growth. For boron (B) growth, we use a B_2O_3 Knudsen effusion cell approach. At a high cell temperature of ~1200 °C, B_2O_3 is decomposed into B atoms

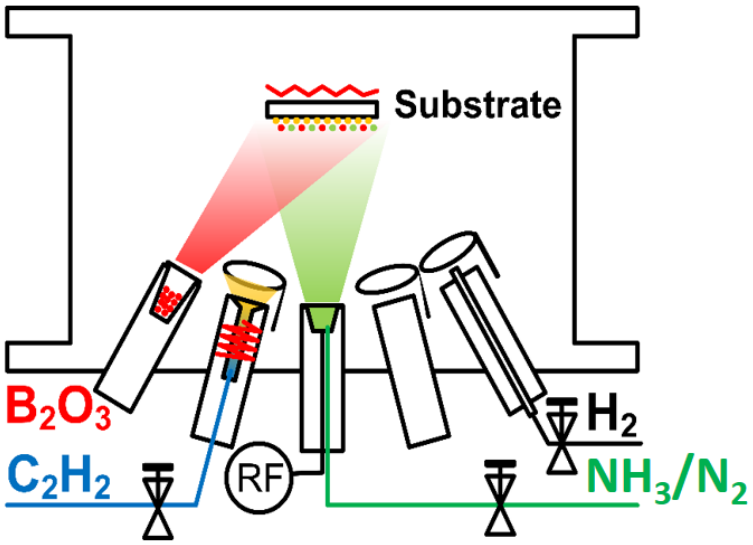

Figure 1.10. Schematic drawing of the MBE growth chamber process in QSL.

and oxygen molecules. B atoms hit the substrate for material growth while oxygen molecules are pumped away by a turbomolecular pump. For nitrogen (N) growth, a radio frequency or electron cyclotron resonance (ECR) plasma generator system is used to form N gas or NH_3 gas plasma. The N source is tuned by either a gas flow meter or ECR/RF current. Figure 1.10 shows a schematic drawing of the MBE growth chamber in QSL.

1.4. Chapters arrangement

In this dissertation, we will discuss the growth and characterization of three different low-dimensional materials and structures with molecular beam epitaxy (MBE) technique. First, in chapter 2, we are going to discuss the epitaxial growth of hexagonal boron nitride/graphene heterostructures (h-BN/G) with high incorporation of C atoms in Co substrate. We will show how the amount of dissolved C atoms in Co and accordingly G growth mechanism can alter the properties and quality of h-BN/G heterostructures in

different growth regions. We will also discuss in detail the effect of individual G or h-BN layers on each other's growth, morphology and thickness.

Following the h-BN/G heterostructure growth and analysis, in chapter 3, we will discuss our new approach of utilizing C atoms to promote the growth of uniform, high quality 2D h-BN layers. We show that the tuning of interstitial C concentration in heated Co substrate can bring a new dimension of control of the substrate surface for the growth and morphology/thickness control of 2D h-BN in addition to other regular growth parameters. Also, for better understanding of our new growth mechanism, we provide DFT calculations on changes in binding energies of B and N atoms when the Co substrate is carburized.

In Chapter 4, we shift the topic to the self-assembled growth and characterization of sub-100 nm c-BN NDs through MBE method. We will discuss the growth mechanism of c-BN NDs on Co and Ni metal foil substrates and show experimentally and theoretically how the nucleation, formation, and morphological properties of c-BN NDs are related with the nature of substrate including catalysis effect, lattice-mismatch-induced strain, roughness, and growth conditions, in particular, growth time and growth temperature. Lastly, in chapter 5, we conclude the dissertation work with a short summary.

1.4. References:

[1] Feynman R. P. There's plenty of room at the bottom. *Eng. Sci.* **23.5** 22 (1960).

[2] Novoselov K. S., Jiang D., Schedin F., Booth T. J., Khotkevich V. V., Morozov S. V. and Geim A. K. Two-dimensional atomic crystals. *Proc. Natl. Acad. Sci. U.S.A* **102**, 10451 (2005).

[3] Allen M. J., Tung V. C. and Kaner R. B. Honeycomb carbon: a review of graphene. *Chem. Rev.* **110** 132 (2009).

[4] Geim A. K. and Grigorieva I. V. Van der Waals heterostructures. *Nature* **499** 419 (2013).

[5] Novoselov S. K., Geim A. K., Morozov S. V., Jiang D., Zhang Y., Dubonos S. V., Grigorieva I. V. and Firsov A. A. Electric field effect in atomically thin carbon films. *Science* **306** 666 (2004).

[6] Geim A. K. and Novoselov K. S. The rise of graphene. *Nat. Mater.* **6** 183 (2007).

[7] Choi W., Lahiri I., Seelaboyina R. and Kang Y. S. Synthesis of graphene and its applications: a review. *Crit. Rev. Solid State Mater. Sci.* **35** 52 (2010).

[8] Zhang Y. I., Zhang L. and Zhou C. Review of chemical vapor deposition of graphene and related applications. *Acc. Chem. Res.* **46** 2329 (2013).

[9] Zhan N., Wang G. and Liu J. L. Cobalt-assisted large-area epitaxial graphene growth in thermal cracker enhanced gas source molecular beam epitaxy. *Appl. Phys. A* **105** 341 (2011).

[10] Zheng R. J., Khanaki A., Tian H., He Y., Cui Y. T., Xu Z. and Liu J. L. Precipitation growth of graphene under exfoliated hexagonal boron nitride to form heterostructures on cobalt substrate by molecular beam epitaxy. *Appl. Phys. Lett.* **111** 011903 (2017).

[11] Bolotin K. I., Sikes K. J., Jiang Z., Klima M., Fudenberg G., Hone J., Kim P. and H. Stormer L. Ultrahigh electron mobility in suspended graphene. *Solid State Commun.* **146** 351 (2008).

[12] Lin Y. M., Valdes-Garcia A., Han S. J., Farmer D. B., Meric I., Sun Y., Wu Y., Dimitrakopoulos C., Grill A., Avouris P. and Jenkins K. A. Wafer-scale graphene integrated circuit. *Science* **332** 1294 (2011).

[13] Lee Y., Bae S., Jang H., Jang S., Zhu S., Sim S. H., Song Y. I., Hong B. H. and Ahn. J.-H. Wafer-scale synthesis and transfer of graphene films. *Nano Lett.* **10** 490 (2010).

[14] Nag A., Raidongia K., Hembram K. P. S. S., Datta R., Waghmare U. V. and Rao C. N. R. Graphene analogues of BN: novel synthesis and properties. *ACS Nano* **4** 1539 (2010).

[15] Liu L., Feng Y. P. and Shen Z. X. Structural and electronic properties of h-BN. *Phys. Rev. B* **68** 104102 (2002).

[16] Watanabe K., Taniguchi T. and Kanda H. Direct-bandgap properties and evidence for ultraviolet lasing of hexagonal boron nitride single crystal. *Nat. Mat.* **3** 404 (2004).

[17] Hattori Y., Taniguchi T., Watanabe K. and Nagashio K. Layer-by-layer dielectric breakdown of hexagonal boron nitride. *ACS Nano* **9** 916 (2015).

[18] Kim S. M., Hsu A., Park M. H., Chae S. H., Yun S. J., Lee J. S., Cho D. H., Fang W., Lee C., Palacios T. and Dresselhaus M. Synthesis of large-area multilayer hexagonal boron nitride for high material performance. *Nat. Commun*. **6** 8662 (2015).

[19] Novoselov K. S. A., Mishchenko A., Carvalho A. and Castro Neto A. H. 2D materials and van der Waals heterostructures. *Science* **353** 9439 (2016).

[20] Xia W., Dai L., Yu P., Tong X., Song W., Zhang G. and Wang Z. Recent progress in van der Waals heterojunctions. *Nanoscale* **9** 4324 (2017).

[21] Schulman D. S., Arnold A. J., Razavieh A., Nasr J. and Das S. The prospect of two-dimensional heterostructures: a review of recent breakthroughs. *IEEE Nanotechnol. Mag.* **11** 6 (2017).

[22] Liu Z., Song L., Zhao S., Huang J., Ma L., Zhang J., Lou J. and Ajayan P. M. Direct growth of graphene/hexagonal boron nitride stacked layers. *Nano Lett.* **11** 2032 (2011).

[23] Bourrellier R., Meuret S., Tararan A., Stéphan O., Kociak M., Tizei L. H. and Zobelli A. Bright UV single photon emission at point defects in h-BN. *Nano Lett.* **16** 4317 (2016).

[24] Liu Y., Weiss N. O., Duan X., Cheng H. C., Huang Y., and Duan X. Van der Waals heterostructures and devices. *Nat. Rev. Mater*. **1** 16042 (2016).

[25] Bhimanapati G. R. *et al.* Recent advances in two-dimensional materials beyond graphene. *ACS Nano* **9** 11509 (2015).

[26] Wang J., Ma F. and Sun M. Graphene, hexagonal boron nitride, and their heterostructures: properties and applications. *RSC Adv.* **7** 16801 (2017).

[27] Zuo Z., Xu Z., Zheng R., Khanaki A., Zheng J.-G. and Liu J. L. In-situ epitaxial growth of graphene/h-BN van der Waals heterostructures by molecular beam epitaxy. *Sci. Rep.* **5** 14760 (2015).

[28] Xu Z., Khanaki A., Tian H., Zheng R. J., Suja M., Zheng J. –G. and Liu J. L. Direct growth of hexagonal boron nitride/graphene heterostructures on Co foil substrates by plasma-assisted molecular beam epitaxy. *Appl. Phys. Lett.* **109** 043110 (2016).

[29] Xu Z., Zheng R., Khanaki A., Zuo Z. and Liu J. L. Direct growth of graphene on in situ epitaxial hexagonal boron nitride flakes by plasma-assisted molecular beam epitaxy. *Appl. Phys. Lett.* **107** 213103(2015).

[30] Zheng R. J., Khanaki A., Tian H., He Y. W., Cui Y. T., Xu Z. G. and Liu J. L. Precipitation growth of graphene under exfoliated hexagonal boron nitride to form heterostructures on cobalt substrate by molecular beam epitaxy. *Appl. Phys. Lett*. **111** 011903 (2017).

[31] Mirkarimi P. B., McCarty K. F. and Medlin D. L. Review of advances in cubic boron nitride film synthesis. *Mater. Sci. Eng*. *R* **21** 47 (1997).

[32] Vel L., Demazeau G. and Etourneau J. Cubic boron nitride: synthesis, physicochemical properties and applications. *Mater. Sci. Eng. B* **10** 149 (1991).

[33] McCray W. P. MBE deserves a place in the history books. *Nat. Nanotechnol*. **2** 259 (2007).

[34] Chang C. A., Ludeke R., Chang L. L. and Esaki L. Molecular-beam epitaxy (MBE) of $In_{1-x}Ga_xAs$ and $GaSb_{1-y}As_y$. *Appl. Phys. Lett*. **31** 759 (1997).

[35] Koma A., Sunouchi K. and Miyajima T. Fabrication of ultrathin heterostructures with van der Waals epitaxy. *J. Vac. Sci. Technol. B* **3** 724 (1985).

Chapter 2: Effect of high carbon incorporation in Co substrates on the epitaxy of hexagonal boron nitride/graphene heterostructures

2.1. Introduction

As a two-dimensional (2D) material, hexagonal boron nitride (h-BN) possesses excellent properties including high band gap energy (~5.9 eV), extremely flat surface (root mean square (RMS) roughness < 0.2 nm) and free of dangling bond or surface charge trap, excellent dielectric properties ($\varepsilon \approx 3–4$ and $V_{breakdown} \approx 12$ MV/cm) and high chemical resistivity [1-5]. In addition, its complementary electronic properties and similar hexagonal lattice structure to graphene (G) and other 2D systems such as transition metal dichalcogenides have made h-BN an ideal candidate for all electronic devices where nanoscale supporting, insulating, capping, or gating layers are needed [6-8]. In particular, h-BN/G stacked layers have recently attracted much attention since such heterostructure system can be used not only to study fundamental physics of G, e.g., Hofstadter butterfly effect, but also to develop next-generation nanoelectronic devices with superior performances, e.g. tunneling devices [9-15].

So far, h-BN/G heterostructures have been mostly prepared by assembling G and h-BN layers exfoliated from highly ordered pyrolytic graphite (HOPG) and h-BN bulk crystals, respectively [16,17]. Although these high-quality structures made by mechanical exfoliation are the best to showcase the material characteristic and/or device performance, all epitaxial vertical heterostructures with controllable thickness, size and well-defined orientation are indispensable toward practical applications. On this matter, both chemical

vapor deposition (CVD) and molecular beam epitaxy (MBE) have been used widely for the growth of h-BN/G heterostructures on different substrates, especially, transition metals such as Cu [18-28]. For example, Liu et al demonstrated the CVD growth of h-BN/G stacks on Cu foil via a two-step process [18]. Gao et al also reported the CVD growth of vertically stacked h-BN/G heterostructures on Cu foil using temperature-triggered (>900 ºC) chemical switching approach [19].

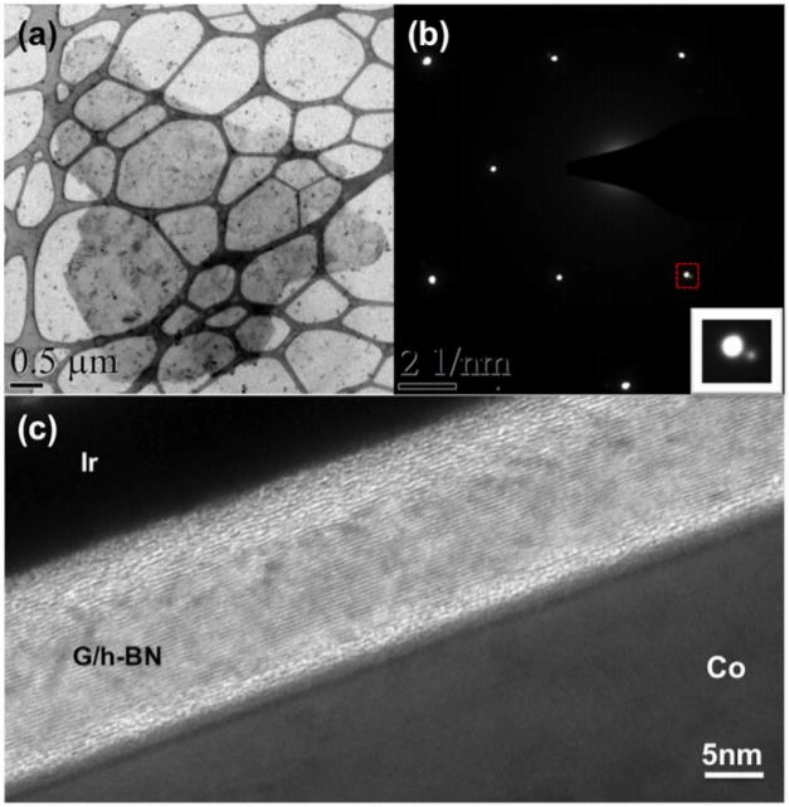

Figure 2.1. (a) Plan-view TEM image of transferred G/h-BN heterostructure. (b) SAED pattern of the same sample. Diffraction patterns with six-fold symmetry are observed. The inset is enlarged image of the red square area marked in (b). Two diffraction spots are observed, revealing the (100) plane distance of 2.13 Å and 2.06 Å, respectively. (c) Cross-sectional TEM image of the sample. The thickness of the heterostructure is about 15 nm [27].

Among all transition metal substrates, Co benefits from having a high melting point temperature (1495 ºC in 1 atm) which minimizes the amount of substrate evaporation during annealing step and high-temperature growth process. This is very crucial when a thin transition metal (foil or thin film) is aimed to use as a substrate, in particular, when a long growth duration is required for the 2D material growth, as this is often the case for h-BN and h-BN/G heterostructures. Also, metal substrates with a higher carbon (C) solubility such as Co (~1.5% at 900 ºC) allow one to work with a wider range of C concentration and within a wider range of growth temperatures. For instance, in our group, we grew h-BN/G heterostructures with few-layer h-BN flakes and single-layer G with less than 1° miss-match angle (Figure 2.1) [27] as well as continuous large-area few-layer h-BN and thick graphitic structure (Figure 2.2) [28] based on Co substrates with different substrate surface conditions, growth temperature, growth time, and other growth parameters. A summary of recent advances on the growth of vertical h-BN/G heterostructures is provided in Table 2.1.

Because many parameters such as source, substrate, growth pressure, growth temperature and substrate cooling rate play roles in the growth of these h-BN/G heterostructures, two major growth mechanisms, namely, precipitation growth and direct layer-by-layer epitaxy, have been observed. Nevertheless, to date, it is still challenging to precisely and reliably control the thickness, morphology and quality of h-BN and G layers, and their alignment across the wafer scale due to the complicated growth processes. In addition, either h-BN/G growth mechanism on the transition metal substrates or the effect of individual G or h-BN layers on each other's growth, morphology and thickness remains

unclear. Therefore, to further elucidate the growth conditions for precise control of different types of h-BN/G heterostructures, in this chapter, we systematically study the effect of high C incorporations in Co on the growth mode/morphology of the epitaxial h-BN/G heterostructures. Three different growth regions of h-BN/G heterostructures are identified based on the concentration of dissolved C atoms in Co and G growth mode. Moreover, the epitaxial relationship between the top h-BN film and bottom G layers in h-BN/G heterostructures is clarified.

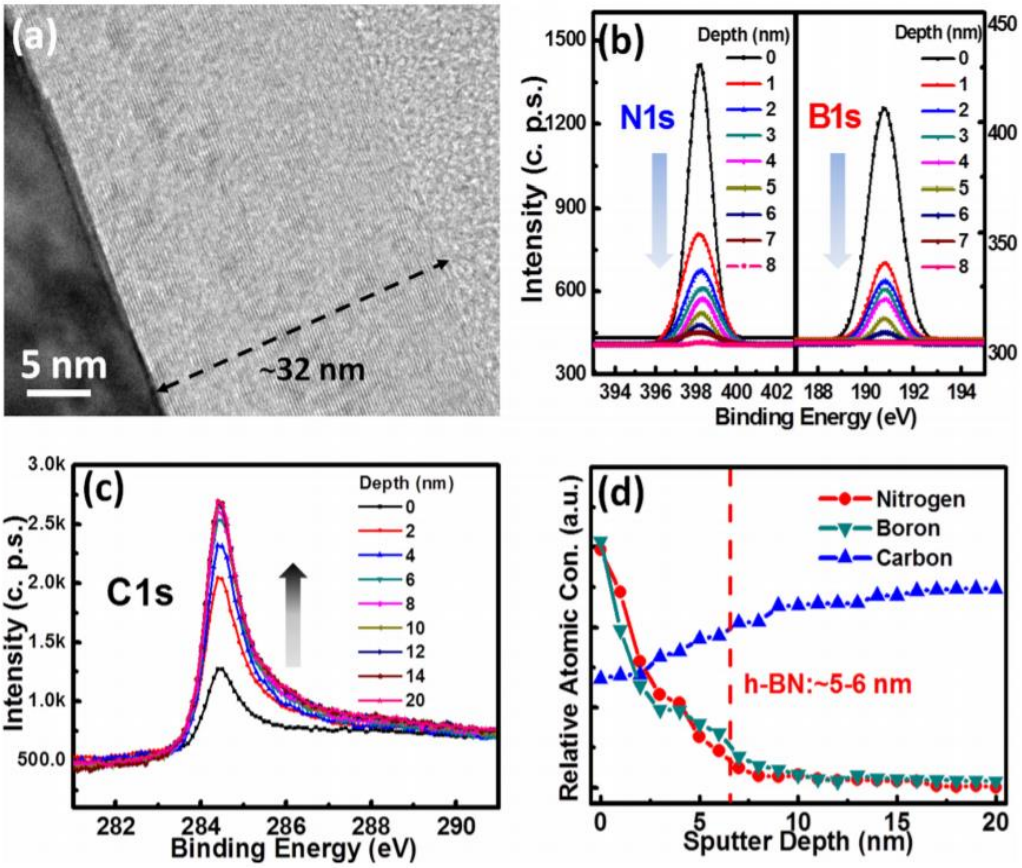

Figure 2.2. (a) Cross-sectional TEM image of the as-grown h-BN/G heterostructure on cobalt foil. Evolution of (b) N1s, B1s and (c) C1s peaks as a function of sputtering depth in the depth-profile XPS characterization. (d) Relative atomic concentration of B, C and N versus sputtering depth [28].

Table 2.1. Summary of the recent reports on the growth of vertical h-BN/G and G/h-BN heterostructures.

Type	Method	Substrate	Growth Temperature (°C)	Thicknesses	Ref
h-BN/G	CVD	Cu foil	G: 950 h-BN: 1000	G:1.0-3.5 nm h-BN: 3.2-20 nm	[18]
G/h-BN	CVD	Cu foil	850	G: ML h-BN: ML	[19]
h-BN/G/h-BN	CVD	Cu foil	1050	$h\text{-}BN_{top}$: 2 nm h-BN: ML $h\text{-}BN_{bottom}$:10 nm	[20]
G/h-BN	G: MBE	h-BN bulk	1500	G: ML h-BN: Bulk	[21]
h-BN/G	G: E-evaporation h-BN: MBE	Ni thin film	730-835	h-BN: 3ML G: 2-3ML	[22]
G/h-BN	G: MBE	h-BN flakes on SiO_2 & Al_2O_3	500 - 1000	h-BN: ML	[23]
G/h-BN	ALD for h-BN MBE for G	Co thin film	h-BN: 327 G: 527	G: 1-7 ML h-BN: 5ML	[24]
G/h-BN	MBE for G	h-BN flake on Co thin film	720-800	G: 2ML h-BN: 3ML	[25]
G/h-BN	MBE	Co foil	850	G: MLL h-BN: ML	[26]
h-BN/G	MBE	Co thin film	870-900	G: MLL h-BN: MLL	[27]
h-BN/G	MBE	Co foil	850	G: 26–27 nm h-BN: 5–6 nm	[28]
G/h-BN	h-BN: IBSD G: CVD	Cu foil	G: 1000 h-BN: 1050	G: 1 ML h-BN: 1ML	[56]

h-BN/G: h-BN was grown on top of G, **G/h-BN**: G was grown on top of h-BN
ML: Monolayer, **MLL**: Multilayer

2.2. Experimental details

Commercial Co foil (Alfa Aesar, 0.1 mm thick, 99.95% purity) was used as the substrate. As-received Co foils were polished by an SBT 920 Lapping and Polishing workstation. Then, Co foils were cut into 1 cm×1 cm pieces, degreased with acetone and IPA, etched by diluted HCl solution (10%) for 2 minutes to remove the native oxides, and rinsed with deionized water. After blown-dry using a nitrogen gun, the fresh substrates were immediately loaded onto substrate holders and transferred to the growth chamber.

A plasma-assisted MBE (Perkin-Elmer) system was used for the sample growth. A Knudsen effusion cell filled with B_2O_3 powder (Alfa Aesar, 99.999% purity) was used as boron (B) source. Nitrogen plasma (Airgas, 99.9999% purity) generated by an electron cyclotron resonance (ECR) system and high-purity ammonia (American Gas Group, 99.9995% purity) were used as nitrogen (N) sources. Acetylene gas (C_2H_2, Airgas, 99.999% purity) was used as C source. The substrates were heated to 800~950 ºC and annealed at the growth temperature under a 10-sccm (standard cubic centimeters per minute) flow of hydrogen gas for 15 minutes. Then, at the same substrate temperature, 3-sccm acetylene gas was introduced into the chamber for a duration of 5 seconds~3 minutes for different samples, and immediately after that, h-BN growth was started. During the growth, B cell temperature was maintained at 1150 ºC; a mixture of nitrogen source consisting of N_2 gas flowed at 10 sccm through an ECR plasma generator and NH_3 gas leaked at a flow rate of 5 sccm through a needle valve was introduced into the chamber. The ECR current was set at 60 mA. The growth lasted from 15 minutes to 3 hours for

different samples. The substrate heating/cooling rate was ~10 ºC/min for all samples. A schematic of the typical growth process is provided in Figure 2.3.

Raman characterizations were performed using a HORIBA LabRam system equipped with a 60-mW, 532-nm green laser. Scanning electron microscopy (SEM) images were acquired using an FEI NNS450 SEM system in secondary electron mode. X-ray photoelectron spectroscopy (XPS) characterization was conducted using a Kratos AXIS ULTRA XPS system equipped with an Al Kα monochromatic X-ray source and a 165-mm mean radius electron energy hemispherical analyzer. The depth-profile XPS characterization was performed on a 3×3 mm^2 area of the sample using a 2-keV Ar ion beam sputter with an etching rate of 1 nm per minute. Atomic force microscopy (AFM)

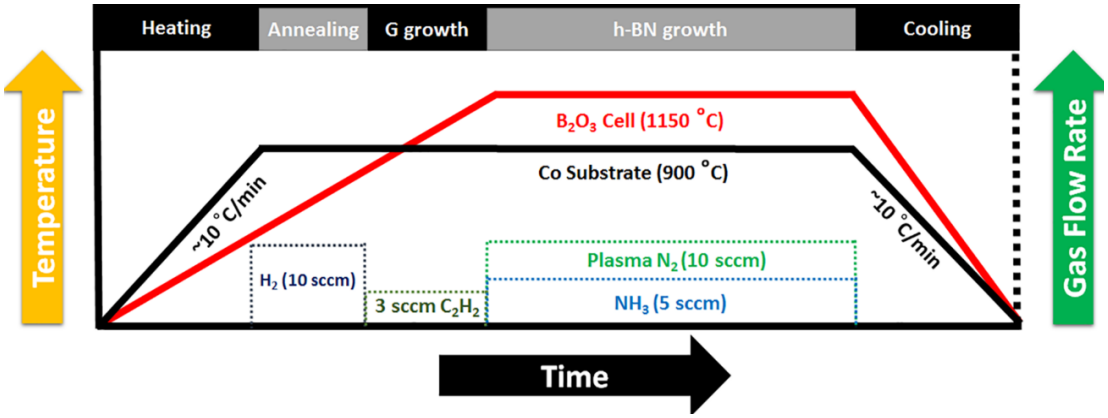

Figure 2.3. Typical growth conditions of h-BN/G heterostructure samples in regions 1-3. To carry out the growth of h-BN/G heterostructure samples, Co substrate was first heated up to 850~950 ºC and annealed for 15 minutes with 10 sccm H_2 gas. Then, the substrate was treated with C (3-sccm C_2H_2 gas) for a duration of 5 sec~3 min for different samples, and immediately after that, h-BN growth was started. During the h-BN growth, B cell temperature was maintained at 1150 ºC. A mixture of N sources consisting of N_2 gas flowed at 10 sccm through an ECR plasma generator and NH_3 gas leaked at a flow rate of 5 sccm through a needle valve was introduced into the chamber. The h-BN growth lasted from 15 min to 3 hrs for different samples. The substrate heating/cooling rate was ~10 ºC/min for all samples.

images were obtained using a Veeco D5000 AFM system in tapping mode. TEM images and selected area electron diffraction (SAED) patterns were acquired using a FEI Tecnai12 system. TEM sample was prepared by picking a transferred h-BN/G film using a 200 mesh Cu grid covered with Quantifoil carbon film with Orthogonal Array of 1.2 μm diameter holes.

For AFM and TEM measurements, samples were transferred using a typical wet transferring method. The as-grown samples were spin-coated first with PMMA (495 A4). Then, we put the samples directly into $FeCl_3$/HCl solution to etch the Co foil substrate for approximately a day. Thereafter, the stacked PMMA/h-BN/G was transferred into 10% HCl and DI water to rinse out the residual etchant. Then, the floating PMMA/h-BN/G was taken out by desired substrates (SiO_2/Si or sapphire) and left to dry in air for at least 12 hours. Then, a few drops of PMMA were deposited again on the transferred film and soaked for another two hours. These additional drops of PMMA soften the previous PMMA layer and enhance the attachment of h-BN/G on the substrate. PMMA was removed by dipping the sample into acetone bath. Finally, the sample was dried at 40 °C on a hot plate for a couple of hours.

Co(contact)/h-BN/G/Co(foil) two-terminal devices were fabricated by a standard photolithography and lift-off process. A Co layer of 50 nm was patterned as top square contacts with an edge length of 25 μm on the surface of as-grown h-BN/G film. Current-voltage (I-V) characteristics were obtained by an Agilent 4155C semiconductor parameter analyzer equipped with probing tips having a diameter of 5μm (Signatone, SE-TL).

2.3. Results and discussion

Figure 2.4 summarizes the growth of h-BN/G heterostructure system on Co foil substrate when the C treatment time changes and h-BN growth conditions are the same (3 hours at 900 °C). Note that C starts to dissolve in Co at around 600 °C ($T_{0\%C}$) and the solubility increases up to ~1.5% at 900 °C [29], i.e. a designated growth temperature (T_{growth}) in the schematic (Figure 2.4(a)). The temperature-dependent growth of h-BN/G heterostructures indicated that the substrate temperature is an important growth parameter to influence the morphology and coverage of h-BN. As it appears in the Figures 2.4 and 2.5, the proper substrate temperature to grow a continuous h-BN/G film is 850~900 °C. Below this temperature, for example 800 °C, the h-BN/G film is not continuous and consists of many thick h-BN ad-layers (bright features, as shown in Figure 2.5(a)). The diffusion length of B and N atoms is relatively low (i.e., high activation/barrier energy) due to the lack of thermal energy and, therefore, B and N atoms tend to bond locally and grow more vertically rather laterally. On the other hand, as the growth temperature exceeds 900 °C, for example, 950 °C, high desorption rate of B and N atoms from Co substrate surface can become the dominant phenomenon and fails the growth of continuous h-BN/G film (Figure 2.5(c)). Thus, the growth temperature of 850~900 °C with 30-sec C treatment time seems to be the conditions to grow continuous and uniform h-BN/G films.

Thermodynamically, G growth on Co can start at temperatures above ~700 °C [30, 31]. The black hatching areas in Figure 2.4(a) show the C concentration in Co substrate at different growth regions (i.e., 1, 2, and 3), and the black horizontal dashed lines display the C solubility levels in Co substrate at designated temperatures (i.e., $T_{0\%C}$, T_G and T_{growth}).

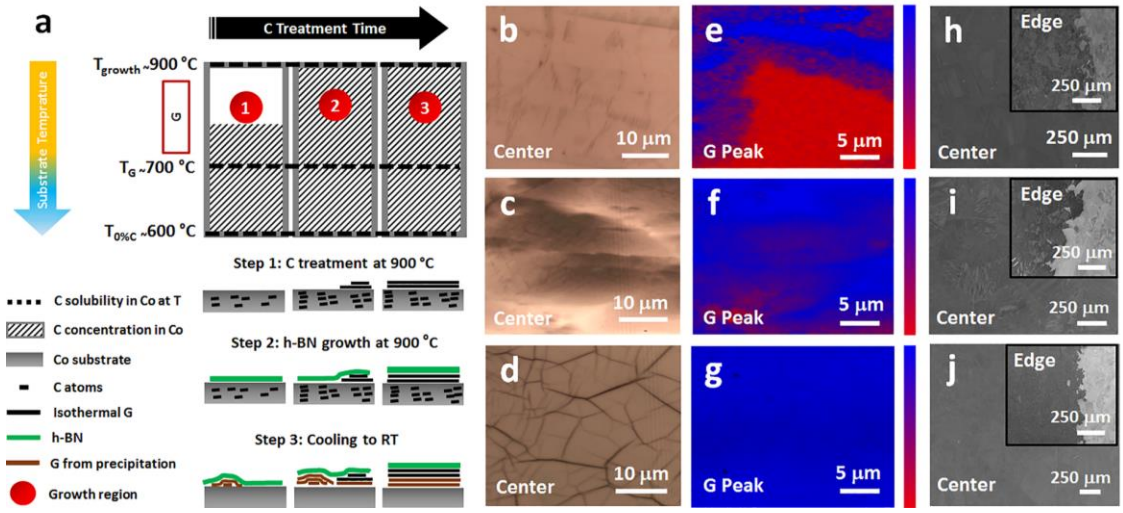

Figure 2.4. H-BN\G heterostructure growth regions on Co substrate. (a) Schematic of h-BN/G growth steps on Co substrate with different C treatment time and same h-BN growth conditions (3 hrs at 900 °C). Three growth regions are identified based on the C treatment time and G growth mode/morphology in h-BN/G samples. (b-d) OM images, (e-g) graphene G peak intensity mapping, and (h-j) SEM images of the samples with 30-sec, 1.5-min, and 3-min C treatment time, which are representative samples in regions 1, 2, and 3, respectively.

The growth regions in Figure 2.4(a) are identified based on the C treatment time, and subsequently, G growth mode/morphology in the h-BN/G samples. Samples with 30-sec, 1.5-min, and 3-min C treatment time are selected as representative samples for regions 1, 2, and 3, respectively, and their optical microscopy (OM), graphene G peak Raman intensity mapping, and SEM images are shown in Figure 2.4(b-j).

Region 1 is where C solubility or saturation of Co is not reached at the growth temperature of 900 °C, hence, G is formed only by precipitation during substrate cooling process, leading to a "G network" underneath the h-BN film. The dark regions in the optical microscopy (OM) image of Figure 2.4(b) for a 30-sec C sample and corresponding Raman intensity mapping of graphene G peak in Figure 2.4(e) display the nature of the G network.

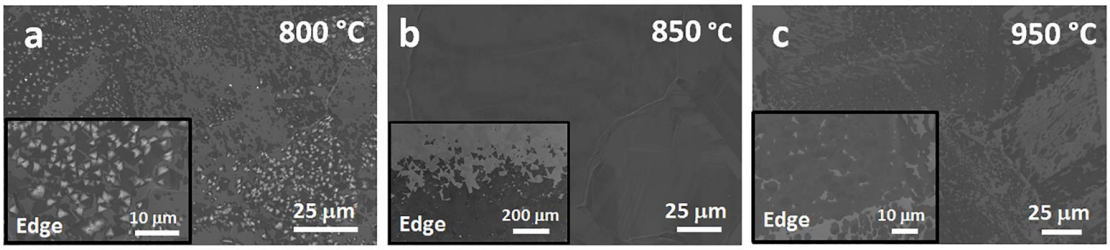

Figure 2.5. H-BN/G temperature-dependent growth with the same 30-sec C treatment time. SEM images of as-grown h-BN/G samples from center and edge areas at (a) 800 °C, (b) 850 °C, and (c) 950 °C. With the same other growth conditions, a growth temperature window, which covers 900 °C, was identified for the formation of continuous high-quality h-BN films in the heterostructures.

Because of this specific morphology, G does not cover a big portion of the Co substrate surface in region 1 samples. This is related to the local accumulation of precipitated C atoms around edge areas of the h-BN flakes (grain boundaries) which is discussed in detail later. This morphology was observed when the C treatment time changed between 5 to 45 seconds.

Region 2 is where the Co substrate is just saturated by C atoms at the growth temperature and, therefore, a part of G growth now occurs isothermally via C saturation-precipitation mechanism [32, 34]. Similar to region 1, another part of G growth in this region occurs later by precipitation when reducing the substrate temperature. Since in region 2 the isothermal G growth is limited only to the formation of a few G flakes/islands, a non-uniform G growth underneath h-BN film is obtained, as seen in the OM image of Figure 2.4(c) for 1.5-min C treatment time sample and corresponding Raman intensity mapping of graphene G peak in Figure 2.4(f). Despite the non-uniform morphology in

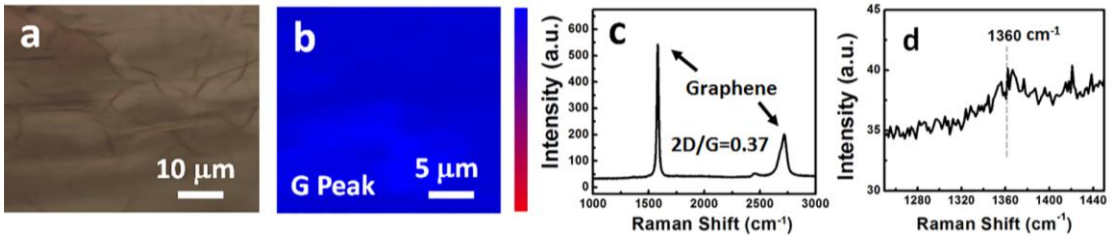

Figure 2.6. OM image and Raman results of G reference sample in region 2. To obtain this sample, the Co substrate was heated up to 900 °C and treated by 3-min C (3 sccm), and then the substrate was cooled to room temperature. (a) OM image and (b) typical Raman spectrum of the G reference sample. (c) typical Raman spectrum showing a 2D/G ratio of ~0.37, and (d) a shorter-range Raman spectrum between 1250 and 1450 cm^{-1} showing a very weak peak at ~ 1360 cm^{-1}.

region 2 samples, based on the Raman mapping results in Figure 2.4(f), the G almost fully covers the Co surface. This was further verified by G reference sample where 1.5-min C treatment time was used to grow only G at 900 °C (Figure 2.6). This morphology was observed when the C treatment time changed between 45 seconds and 2 minutes.

Further introduction of excess C at the growth temperature with the C treatment time exceeding 2 minutes leads the growth mode into region 3. In this region, isothermally grown G has already covered the entire substrate surface at the growth temperature, and after the formation of continuous h-BN on the isothermally grown continuous G layer, additional G layers are formed under the structure during the cooling process, resulting in a uniform heterostructure consisting of thick G and thin h-BN (Figure 2.4(d,g,j) of the sample with 3-min C treatment time). Figure 2.7 shows OM image, graphene G peak Raman intensity mapping and typical Raman spectrum of the G reference sample with 3-min C treatment time. A 2D/G intensity ratio of ~0.35 was calculated and no graphene D peak was observed in the spectrum (Figure 2.7(d)), suggesting the high-quality growth of

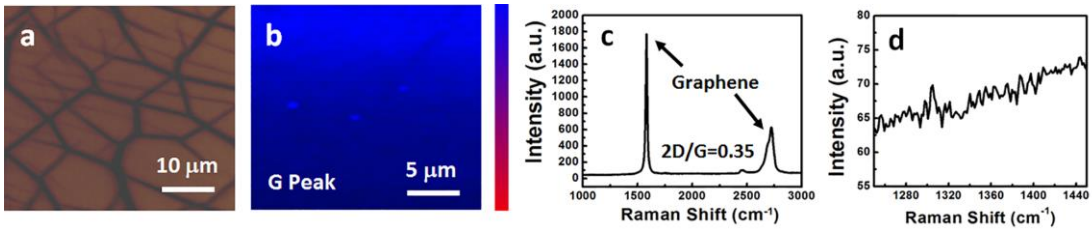

Figure 2.7. OM image and Raman results of G reference sample in region 3. To obtain this sample, the Co substrate was heated up to 900 °C and treated by 3-min C (3 sccm), and then the substrate was cooled to room temperature. (a) OM image, (b) graphene G peak Raman intensity mapping, (c) typical Raman spectrum of the G reference sample in region 3 with a 2D/G intensity ratio of ~0.35 and (d) a shorter-range Raman spectrum between 1250 and 1450 cm^{-1} showing no apparent graphene D-peak in the reference sample.

thick G layers. Figure 2.8 shows additional OM images of the samples to further indicate the evolution of the G morphology in these regions. Finally, in all three regions, h-BN is

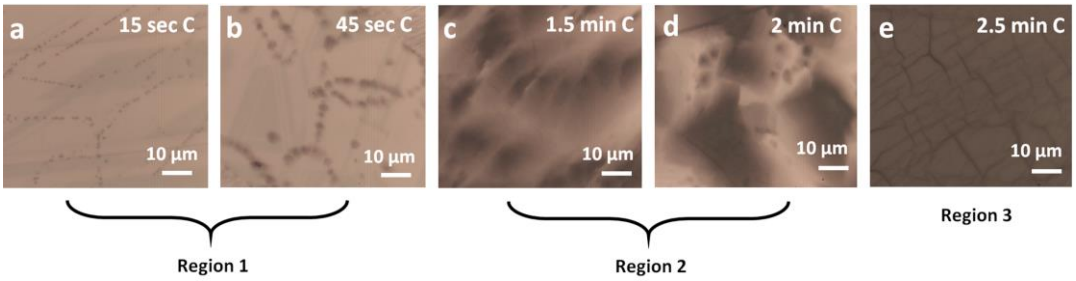

Figure 2.8. Additional OM images of h-BN/G samples with different C amounts. OM images of h-BN/G samples with (a) 15-sec and (b) 45-sec C treatment time showing the enlargement of G network morphology in typical region 1 samples. By increasing the C treatment time to 1.5 min (c), a mixture of G network morphology and G islands (initially formed at the growth temperature) can be seen. The G morphology evolves towards the formation of more G islands by using 2-min C treatment time (d). This mixture morphology is typical of region 2 samples. By further increasing the C treatment time to 2.5 min (e), the formation of G layers at the growth temperature leads to a thick uniform G film underneath h-BN in region 3 samples.

solely deposited at the growth temperature (a condition we referred as isothermally grown or epitaxial), i.e., it is not formed by precipitation mechanism during substrate cooling period. This is because the solubility of both B and N in Co are extremely low [35].

Figure 2.9 shows detailed characterization results of typical region 1 samples. In the SEM images of h-BN/G samples with 5-, 30- and 45-sec C treatment time (Figure 2.8(a-c)), distinct G network morphology appears with a darker color compared to the surrounding area as G produces less secondary electrons compared to the Co metal substrate [36]. The width of G network changes from 5~10 μm for 5-sec C treatment time sample, to 11~13 μm for 30 -sec C treatment time sample, and to 12~16 μm for 45-sec C treatment time sample. It seems that the width of G network increases notably from 5-sec to 30-sec C treatment time and then remains about the same values from 30-sec to 45-sec treatment time, which can be an indication of Co saturation by dissolved C atoms within 45 seconds of C treatment at the growth temperature of 900 °C.

To better understand the h-BN/G network morphology, we transferred the sample with 30-sec C treatment time onto SiO_2/Si substrate and performed AFM measurement (Figure 2.9(d)). The measured AFM line profile reveals that the h-BN film thickness is ~ 2.1 nm and h-BN/G network is ~12.4 nm, suggesting a G network thickness of ~10.3 nm. Figure 2.9(e) and (f) show Raman spectra of h-BN and h-BN/G network areas (1) and (2), respectively, marked in the AFM image in Figure 2(d). It can be clearly seen that the point (1) only shows the h-BN E_{2g} vibrational mode at 1367 cm^{-1} (Figure 2.9(e)), while point 2 shows the co-existence of h-BN and multilayer G peaks (Figure 2.9(f)) [25-28]. Raman results suggest that h-BN is continuous although G is not in the region 1 samples. Figure

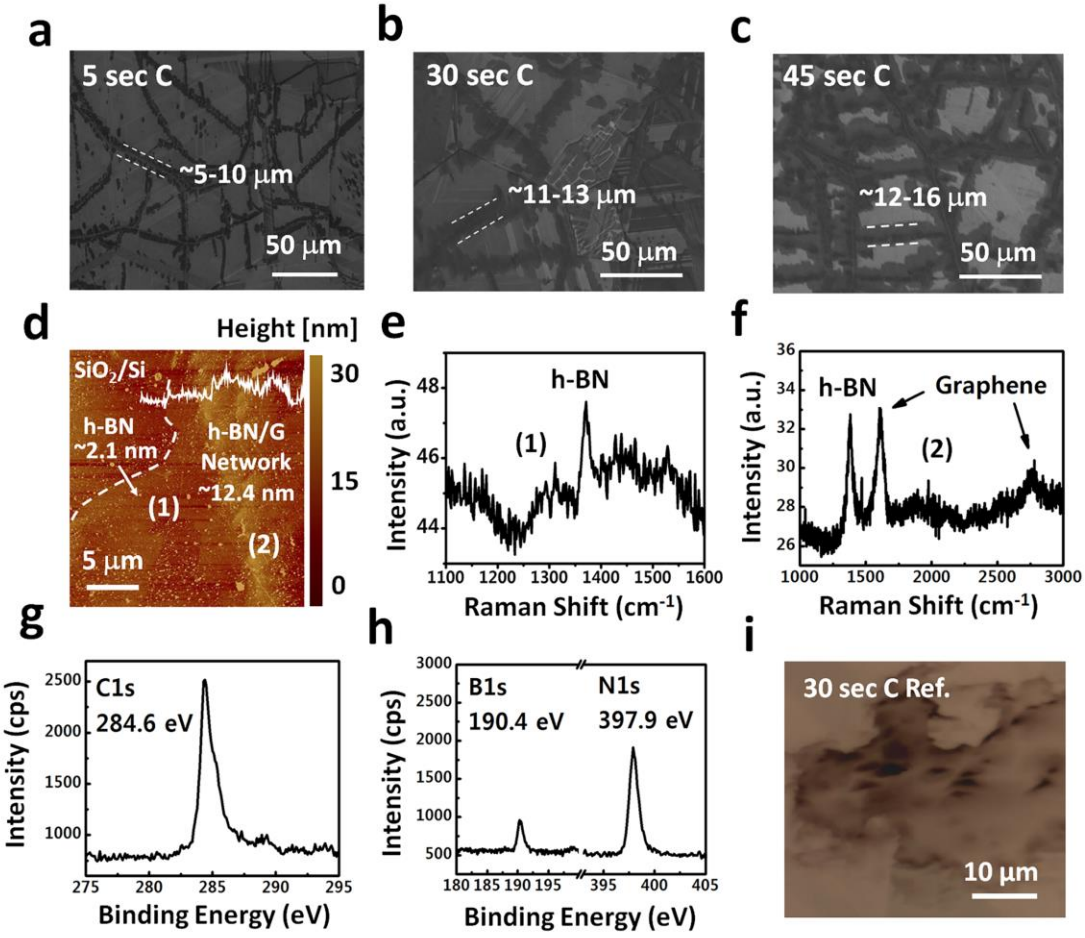

Figure 2.9. Characterizations of h-BN/G samples in region 1. SEM images of the h-BN/G samples with (a) 5-sec, (b) 30-sec, and (c) 45-sec C treatment time showing the G network morphology. (d) AFM image of h-BN/G sample with 30-sec C treatment time transferred onto SiO_2/Si substrate. (e) and (f) Raman spectra of the points (1) and (2) of (d), respectively. XPS signals of (g) C1s, and (h) B1s and N1s for as-grown h-BN/G sample with 30-sec C treatment time. (i) OM image of the G reference sample with 30-sec C time.

2.9(g) and (h) show C1s, and B1s and N1s XPS spectra of a 30-sec C treatment sample, respectively. C1s peak occurs at 284.6 eV indicating the existence of C sp^2 bonding of G layers [37,38]. B1s and N1s exhibit energy positions at 190.4 eV and 397.7 eV, respectively,

which is consistent with the reported values for XPS signals of h-BN [39,40]. By using sensitivity factors from the instrument manufacturer and calculating the atomic % of each atom, the B/N ratio is 1.03, suggesting an almost equal composition of B and N elements.

Figure 2.9(i) shows an OM image of a C-only reference sample. To grow this sample, the Co foil substrate was heated up to 900 ºC, treated with 30-sec C exposure and then cooled to room temperature. As it can be seen in Figure 2.9(i), the G morphology in the C reference sample is quite different with G morphology of h-BN/G sample with the same amount of C treatment time (Figure 2.4(b)). This difference in G morphology is believed to be caused by the top h-BN film rather than the Co substrate because the density of the Co substrate grain boundaries and imperfection sites in both h-BN/G and G reference samples should be about the same and uniformly distributed across the substrate's surface. The fact that the G in region 1 samples is only formed by precipitation during the cooling process, that is after h-BN film growth, makes the G morphology affected by the h-BN film. The G network morphology is the outcome of preferential C atom precipitation in the vicinity of h-BN grain boundaries, which have a random distribution within the h-BN film.

Figure 2.10 shows characterization results of the G reference sample in region 1 with 30-sec C treatment time. Graphene G peak intensity mapping of the reference sample (Figure 2.10(a)) shows a more uniform distribution of less intense G peak compared to that of h-BN/G sample with the same G growth conditions (Figure 2.4(e)). This suggests that when there is no h-BN on top, precipitated C atoms tend to form larger and thinner domains. Also, a D peak at ~1356 cm^{-1} with a FWHM of ~34 cm^{-1} was observed (Figure 2.10(b,c)), indicating a low quality G growth in this region. Overall, it appears that h-BN

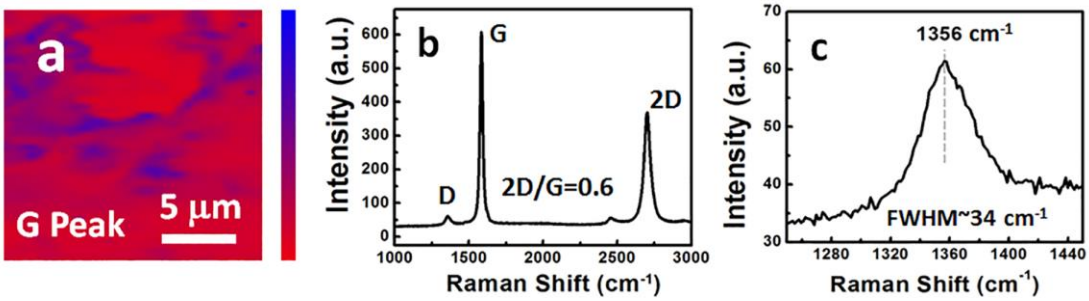

Figure 2.10. Raman results of G reference sample in region 1. To obtain this sample, the Co substrate was heated up to 900 °C and treated by 30-sec C (3 sccm), and then the substrate was cooled to room temperature. (a) graphene G peak Raman intensity mapping, (b) typical Raman spectrum of the G reference sample in region 3 with a 2D/G intensity ratio of ~0.6 and (c) a shorter-range Raman spectrum between 1250 and 1450 cm^{-1} showing a D peak at ~1356 cm^{-1} with a FWHM of ~34 cm^{-1}.

growth has the largest effect on the G growth (quality/morphology/thickness) in region 1 samples since the G is formed after h-BN growth. As the G growth mode gradually changes from precipitation during cooling process to isothermal growth at high temperatures (i.e., regions 2 and 3), the effect of top h-BN film on the growth and morphology of underneath G layers becomes less evident.

Figure 2.11 shows characterization results of h-BN/G samples with the same 30-sec C treatment time and different h-BN growth time. It can be seen in the SEM images of Figure 2.10(a-d) that the coverage and size of the triangular h-BN flakes increases as the increase of h-BN growth time and the whole Co substrate surface is almost covered with h-BN as the growth time reaches ~1 hr. Figure 2.11(e) shows h-BN lateral growth speed as a function of growth time. The area of h-BN coverage is obtained by ImageJ software (see Figure 2.12) and the growth speed is defined as the area of coverage divided by the growth

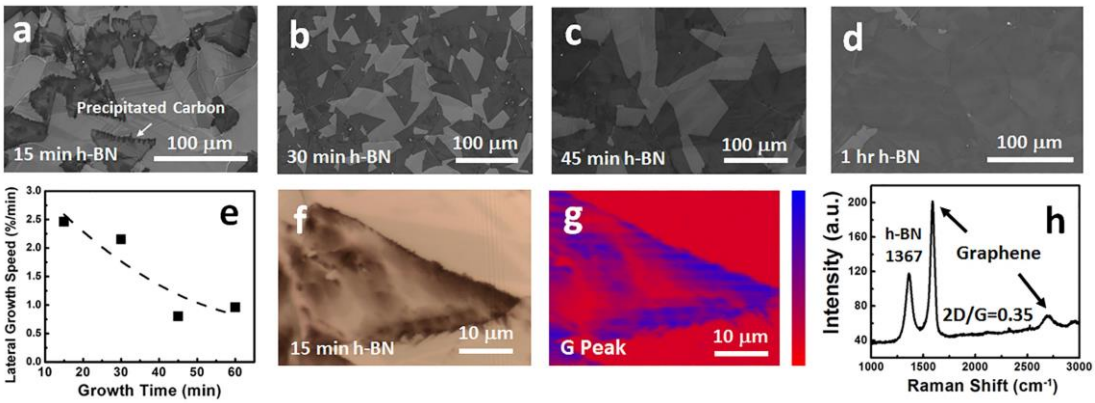

Figure 2.11. H-BN time-dependent growth of region 1 h-BN/G samples with 30-sec C treatment time. (a-d) SEM images of h-BN/G samples with 15-min, 30-min, 45-min and 1-hr h-BN growth duration. (e) h-BN lateral growth speed and triangle edge length for samples in (a-d). (f) OM image and corresponding (g) graphene G peak Raman intensity mapping and (h) Raman spectrum of (g) at its strongest signal point. H-BN E_{2g} Raman peak at ~1367 cm^{-1} has a FWHM of ~65 cm^{-1} and graphene 2D/G intensity ratio is ~0.35.

time. As seen from Figure 2.11(e), the h-BN lateral growth rate is relatively high in the short h-BN growth period (~ 2.5 %/min at 15 minutes), and then gradually decreases to lower values as the growth progresses (~ 1 %/min at 1 hr). This further justifies the continuous morphology of the h-BN films for all samples grown for 3 hours. It should be noted that the SEM image in Figure 2.11(a) and OM image in Figure 2.11(f) of the 15-min h-BN growth sample show the accumulation of C atoms (dark color) around triangular h-BN flakes. Figure 2.11(g) and (h) show graphene G peak Raman intensity mapping of Figure 2.11(f) and corresponding Raman spectra from the point of the strongest Raman signal in Figure 2.11(g), respectively. The Raman scattering results clearly support the findings from the microscopy studies in Figure 2.11(a) and (f). This behavior, i.e., C

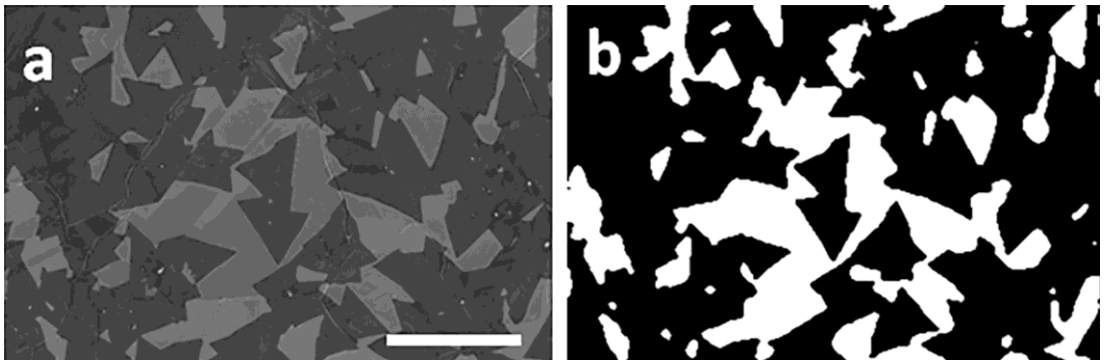

Figure 2.12. An example of h-BN/G coverage calculation for h-BN time-dependent growth samples using ImageJ software. First, an area of ~1 mm^2 from an SEM image was selected for each sample. (a) shows the SEM selected area for the h-BN/G sample grown with 30-sec C treatment time and 30-min h-BN growth time at 900 ºC. (b) By applying a black/white contrast threshold, h-BN flakes are identified with black color. Subsequently, the software measured the black area and divided it by the total area (~1 mm^2) to calculate the h-BN/G coverage for each sample. The scale bar in (a) is 100 μm.

preferential precipitation along h-BN triangle edges and/or grain boundaries during the cooling process, is also consistent with the formation mechanism for the G network underneath the h-BN film of h-BN/G samples in region 1 (Figures 2.4 and 2.11). The graphene 2D/G intensity ratio of the as-grown sample was calculated ~0.35 (Figure 2.11(h)) which is much lower than that of G reference sample in region 1, that is ~0.6 (Figure 2.10(b)). This further shows the effect of top h-BN film on the thickness of underneath G layers in region 1 samples. A wide FWHM of h-BN E_{2g} peak (~65 cm^{-1}) in Figure 2.11(h) can be due to the incorporation of intrinsic graphene D peak in the sample (Figure 2.9(c)).

Figure 2.13 shows Raman spectrum and C1s, B1s and N1s XPS signals of a

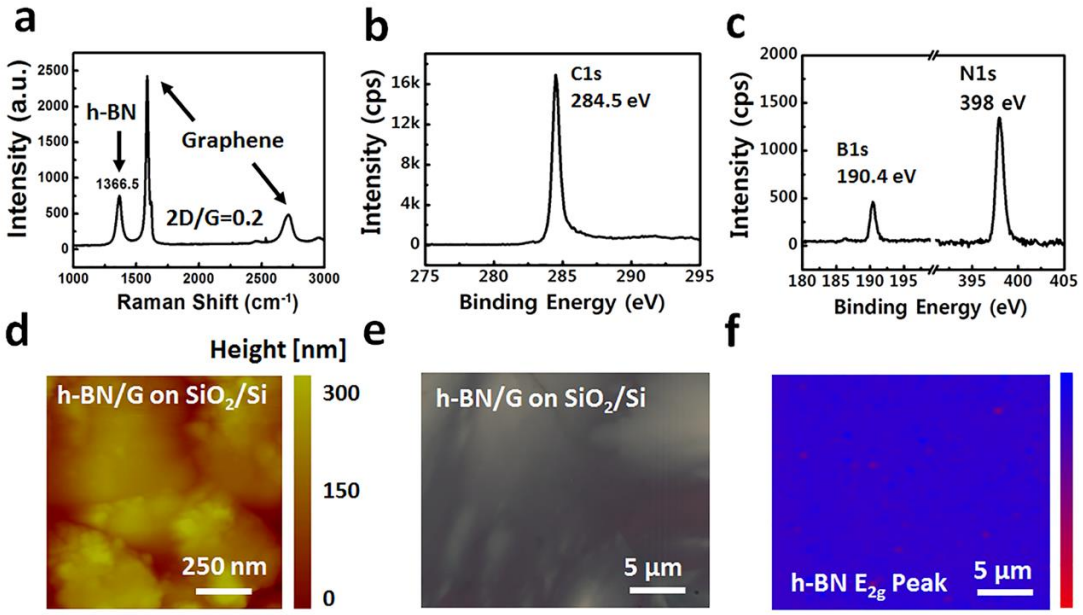

Figure 2.13. Characterization of h-BN/G sample in region 2. (a) Representative Raman spectrum of the as-grown sample. (b) C1s and (c) B1s and N1s XPS signals of the same sample. (d) AFM image of transferred h-BN/G sample with 1.5-min C treatment time onto SiO_2/Si substrate. (e) OM image of the transferred sample and (f) h-BN E_{2g} phonon peak intensity mapping of (e).

representative region 2 sample with a 1.5-min C treatment time, and AFM and OM images of the same sample after the h-BN/G structure was transferred onto a SiO_2/Si substrate and its corresponding h-BN E_{2g} phonon mode intensity mapping. Since the isothermal G growth in this region is limited only to the formation of a few G flakes/islands, the final G morphology in h-BN/G sample is a mixture of isothermal G growth and precipitation during the cooling process, resulting in a non-uniform G film. According to Figure 2.12(f), despite the non-uniform morphology of G growth in this region, the h-BN has been formed continuously and fully covered the sample's surface.

Figure 2.14 shows characterization results of typical h-BN/G samples in region 3. Figure 2.14(a) shows Raman spectra of an as-grown h-BN/G sample with 3-min C treatment time at 13 locations across the 1cm×1cm h-BN/G sample (indicated in a photo image in the inset of Figure 2.14(a)). The existence of both multilayer G (MG or thin graphite) and h-BN Raman peaks is evident. The 2D/G ratio of MG in this sample was calculated ~0.18. Figure 2.14(b) is the zoom-in spectra of Figure 2.14(a) between 1200 and 1500 cm^{-1}, showing excellent uniformity of h-BN E_{2g} phonon mode's position (~1366.57 cm^{-1}), intensity and full width at half maximum (FWHM~40 cm^{-1}) over these 13 points of measurement [41]. A portion of the sample was transferred onto SiO_2/Si substrate for the AFM measurement. The AFM image reveals that the h-BN/G film has a total thickness of ~133 nm (Figure 2.14(c)).

To reveal the individual thickness of h-BN and MG layers, we performed XPS sputtering depth profile measurement. Figure 2.14(d) and (e) show the evolution of C1s, and B1s and N1s XPS signals as a function of sputtering depth within 4 nm of the top surface of h-BN/G sample. As seen in Figure 2.14(d), C1s peak is strongest when the sample was not sputtered, which is due to the inclusion of signals from absorbed C species on the surface or adventitious C [42]. After removing the top 0.17 nm material, the intensity of C1s peak drops significantly compared with the signal before sputtering and then remains about the same with further sputtering while the width of the C1s peak increases as the sputtering depth increases (down to ~1-2 nm) due to Ar^+ beam induced damage. On the other hand, B1s and N1s XPS signals in Figure 2.14(e) decrease proportionally and gradually by removing the top layers and become negligible when the

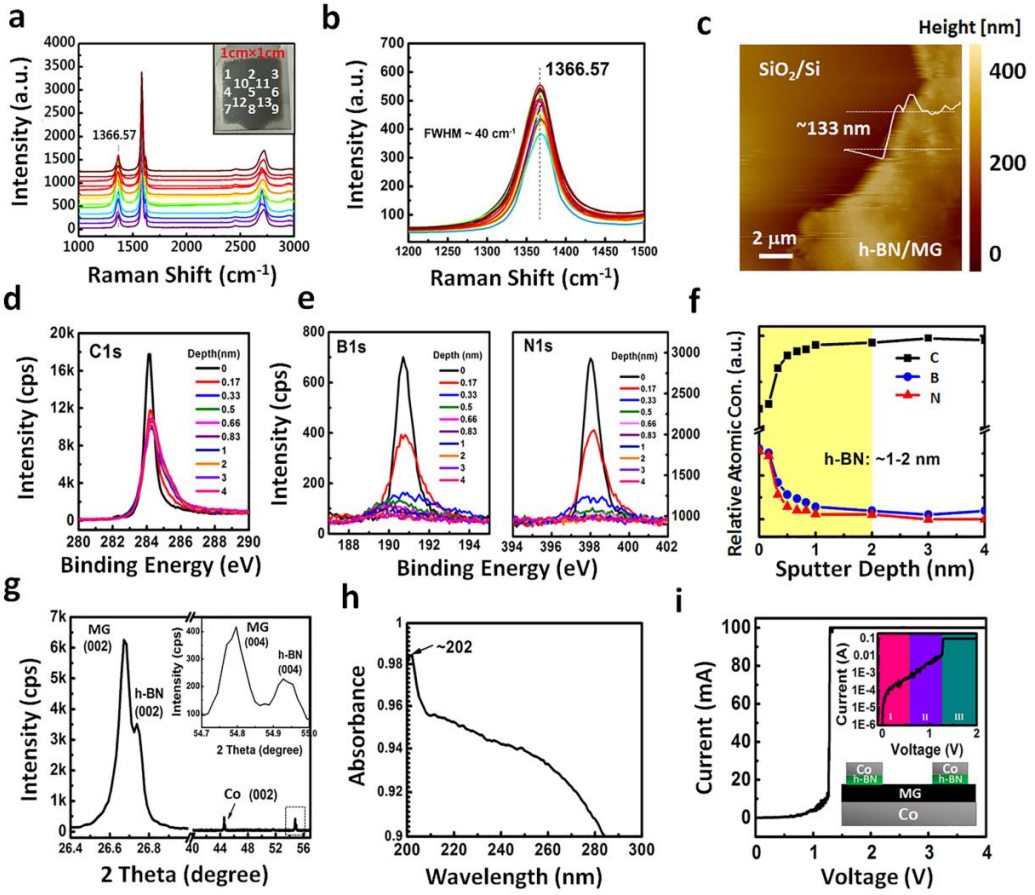

Figure 2.14. Characterization of h-BN/MG samples in region 3. (a) 13-points Raman spectra of the as-grown h-BN/MG sample with 3-min C treatment time and inset shows the sample photograph. The 2D/G ratio of G in this sample was calculated ~0.18. (b) Zoom-in Raman spectra of (a) showing the h-BN E_{2g} phonon mode at ~1366.5 cm^{-1} with a uniform FWHM of ~40 cm^{-1} across these 13 points of measurement. (c) AFM image of the same sample transferred onto SiO_2/Si substrate with the total thickness of ~133 nm. (d) C1s and (e) B1s and N1s as a function of sputtering depth in the depth-profile XPS characterization and (f) relative atomic concentration of C, B, and N versus sputtering depth. (g) XRD spectrum of the same sample. Inset is the magnified spectrum with 2theta from 54.7 to 55°. (h) UV absorption spectrum of the h-BN/MG sample transferred onto a sapphire substrate. (i) I-V characteristic of Co(contact)/h-BN/MG/Co(foil) two-terminal device structure with the contact size of 25μm×25μm. The inset displays the log-scale current versus voltage behavior of the device with 3 distinct regions.

relative atomic concentration for B, N, and C as a function of the sputtering depth. As the sputtering depth increases, both N and B concentrations decrease gradually and reach an insignificant percentage at a sputtering depth of 1~2 nm, while the C concentration gradually levels up and then becomes steady as the etching depth extends from 2 to 4 nm. Considering the AFM (Figure 2.14(c)) and XPS depth-profile (Figure 2.14(f)) measurement results, it can be concluded that the h-BN/MG structure has a top h-BN layer of 1~2 nm and a bottom MG layer of 131~132 nm. Such a large thickness of MG is believed to be caused mainly by precipitation of dissolved C atoms during cooling process. Much higher substrate cooling rates could significantly reduce the total G thickness, although thermal strain induced wrinkles could compromise the quality of the precipitated G in those cases [43]. Alternatively, other transition metals with much less C solubilities can be used to control the number of G layers down to a few layers [44,45]. Owing to the fact that these C atoms precipitate underneath the isothermally grown MG buffer, the morphological and structural uniformity of h-BN/G samples is well preserved, as inferred from Figure 2.14(c) and (g). Moreover, similar h-BN thickness in region 1 (~2.1 nm) and region 3 (1~2 nm) samples indicates that the h-BN vertical growth is not affected by the G growth mechanism, morphology or thickness (Figures 2.11 and 2.14). The seemly self-limited growth of h-BN on G with different morphology under the present growth condition is intriguing and needs further investigation. Similar self-limited growth of h-BN on metal substrates was also reported [46-50].

Figure 2.14(g) shows XRD pattern of the h-BN/G sample. The evident peaks at 26.64° and 54.79°, and 27.1° and 54.94° are assigned to (002) and (004) crystal plane

diffractions of MG and h-BN films according to JCPDS card numbers 41-1487 and 34-0421, respectively [51,52]. The small peak at 51.5° is from (002) crystal plane diffraction of hcp Co (JCPDS# 01-071-4239) [53,54]. Such intense XRD peaks indicate the high-quality of MG and h-BN films in the sample. It can be also realized that h-BN and MG have grown on the same crystal planes and along the same orientation. To further elucidate the epitaxial relation between h-BN and MG, we transferred a piece of the same sample and performed TEM measurement (Figure 2.15). Figure 2.15(a) shows the bright-field top-view image of the transferred film on the TEM grid and Figure 2.15(b) shows the SAED pattern obtained from the area in Figure 2.15(a). A single hexagonal pattern is observed (Figure 2.15(b)); however, the dots are slightly elongated, suggesting overlapping

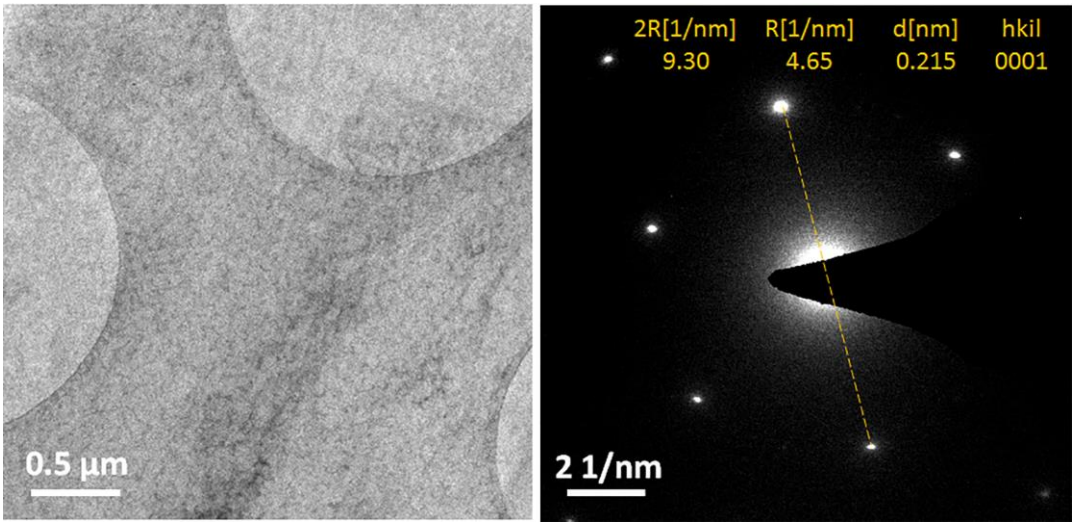

Figure 2.15. TEM results of the h-BN/G sample in region 3. (a) Bright-field top-view image of the transferred h-BN/G on the TEM grid and (b) corresponding SAED pattern of (a). A single hexagonal pattern can be observed in (b); however, the dots are slightly elongated, suggesting overlapping hexagonal patterns of h-BN and MG films with possibly a little miss-orientation. This proves the epitaxial relation of h-BN and MG stacked layers.

hexagonal patterns of h-BN and MG films with possibly a little miss-orientation. Figure 2.14(h) shows an absorption spectrum of the sample after a portion of the h-BN/MG film was transferred to a sapphire substrate. As can be seen in Figure 2.14(h), the clear absorption edge at ~202 nm originates from the band gap of h-BN film [55]. A big portion of UV light spectrum has been also absorbed by the thick MG film [56]. Figure 2.14(i) shows cross-plane I-V characteristic of a Co(contact)/h-BN/G/Co (substrate) two-terminal device. The bottom inset shows a schematic of the device, which was fabricated using a process described in the Experimental section. The top inset displays the log-scale current versus voltage behavior of the device, showing 3 distinct regions: I) current linearly increases as the increase of voltage, which represents direct-tunneling related conduction ($V<\sim0.6$) [56], II) current nonlinearly/exponentially increases with the voltage under moderate biases ($\sim0.6<V<\sim1.25$) due to Fowler-Nordheim tunneling [57], and III) current sharply increases due to the dielectric breakdown at a bias of 1.25 V [58]. The calculated breakdown electric field based on an h-BN thickness of 1~2 nm is 6.25-12.5 MV/cm, which is comparable with the observed values from other epitaxial h-BN films [58-60].

2.4. Conclusion

We performed a systematic study of the in-situ growth of h-BN/G films on Co substrate by sequentially introducing C source with a high C incorporation, and B and N sources in an MBE system. It is found that the continuous h-BN/G heterostructures can be formed at a substrate temperature of 850~900 ºC. By changing the C amount incorporation, the h-BN/G structure alters from region 1 where G network is formed only by precipitation during cooling process underneath the h-BN film; to region 2 where isothermal G growth

occurs to form G islands partially covering the substrate, followed by further precipitation G growth, leading to a non-uniform h-BN/G structure, and to region 3 where a uniform h-BN/G heterostructure with a thin continuous h-BN and a thick continuous MG are formed from both isothermal G growth and precipitation. It is found that the top h-BN film influences the morphology, thickness and quality of underneath G layers in h-BN/G samples of region 1. In addition, the h-BN growth is self-limited to a 1~2 nm thick film in all three regions, regardless of the underneath G thickness or morphology.

2.5. References

[1] Nag A., Raidongia K., Hembram K. P. S. S., Datta R., Waghmare U. V. and Rao C. N. R. Graphene analogues of BN: novel synthesis and properties. *ACS Nano* **4** 1539 (2010).

[2] Liu L., Feng Y. P. and Shen Z. X. 2002 Structural and electronic properties of h-BN. *Phys. Rev. B* **68** 104102 (2003).

[3] Watanabe K., Taniguchi T. and Kanda H. Direct-bandgap properties and evidence for ultraviolet lasing of hexagonal boron nitride single crystal. *Nat. Mat.* **3** 404 (2004).

[4] Hattori Y., Taniguchi T., Watanabe K. and Nagashio K. Layer-by-layer dielectric breakdown of hexagonal boron nitride. *ACS Nano* **9** 916 (2015).

[5] Kim S. M *et al* Synthesis of large-area multilayer hexagonal boron nitride for high material performance. *Nat. Commun.* **6** 8662 (2015).

[6] Novoselov K. S. A., Mishchenko A., Carvalho A. and Castro Neto A. H. 2D materials and van der Waals heterostructures *Science* **353** 9439 (2016).

[7] Xia W., Dai L., Yu P., Tong X., Song W., Zhang G. and Wang Z. Building three-dimensional graphene frameworks for energy storage and catalysis. *Nanoscale* **9** 4324 (2017).

[8] Schulman D.S., Arnold A.J., Razavieh A., Nasr J. and Das S. The prospect of two-dimensional heterostructures: A review of recent breakthroughs. *IEEE Nanotechnol. Mag*. **11** 6 (2017).

[9] Yankowitz M., Xue J., Cormode D., Sanchez-yamagishi J. D., Watanabe K., Taniguchi T., Jarillo-Herrero P., Jacquod P. and LeRoy B. J. Fast pick up technique for high quality heterostructures of bilayer graphene and hexagonal boron nitride. *Nat. Phys.* **8** 382 (2012).

[10] Aggoune W., Cocchi C., Nabok D., Rezouali K., Belkhir M. A. and Draxl C. Enhanced Light-Matter Interaction in Graphene/h-BN van der Waals Heterostructures. *J. Phys. Chem. Lett.* **8** 1464 (2017).

[11] Dean C. R. *et al* Hofstadter's butterfly and the fractal quantum Hall effect in moiré superlattices. *Nature* **497** 598 (2013).

[12] Cheng R. *et al* Multifunctional tunneling devices based on graphene/h-BN/MoSe2 van der Waals heterostructures. *Appl. Phys. Lett.* **110** 173507 (2017).

[13] C. R. Dean *et al* Boron nitride substrates for high-quality graphene electronics. *Nat.*

Nanotechnol. **5** 722 (2010).

[14] Amet F., Williams J. R., Garcia A. G. F., Yankowitz M., Watanabe K., Taniguchi T. and Goldhaber-Gordon D. Tunneling spectroscopy of graphene-boron-nitride heterostructures. *Phys. Rev. B* **85** 073405 (2012).

[15] Britnell L. *et al* Field-effect tunneling transistor based on vertical graphene heterostructures. *Science* **335** 947 (2012).

[16] Novoselov K. S., Jiang D., Schedin F., Booth T. J., Khotkevich V. V., Morozov S. V. and Geim A. K. Two-dimensional atomic crystals. *Proc. Natl. Acad. Sci. U.S.A.* **102** 10451 (2005).

[17] Pacile D., Meyer J. C., Girit C. O. and Zettl A. The two-dimensional phase of boron nitride: Few-atomic-layer sheets and suspended membranes. *Appl. Phys. Lett.* **92** 133107 (2008).

[18] Liu Z., Song L., Zhao S., Huang J., Ma L., Zhang J., Lou J. and Ajayan P. M. Direct growth of graphene/hexagonal boron nitride stacked layers. *Nano. Lett.* **11** 2032 (2011).

[19] Gao T., Song X., Du H., Nie Y., Chen Y., Ji Q., Sun J., Yang Y., Zhang Y. and Liu Z. Temperature-triggered chemical switching growth of in-plane and vertically stacked graphene-boron nitride heterostructures. *Nat. Commun.* **6** 6835 (2015).

[20] Wu Q., Jang S. K., Park S., Jung S. J., Suh H., Lee Y. H., Lee S. and Song Y. J. Layer-controlled CVD growth of large-area two-dimensional MoS_2 films. *Nanoscale* **7** 7574 (2015).

[21]Summerfield A. *et al* Strain-engineered graphene grown on hexagonal boron nitride by molecular beam epitaxy *Sci. Rep.* **6** 22440 (2016).

[22] Wofford J. M., Nakhaie S., Krause T., Liu X., Ramsteiner M., Hanke M., Riechert H. and Lopes J. M. A hybrid MBE-based growth method for large-area synthesis of stacked hexagonal boron nitride/graphene heterostructures. *Sci. Rep*. **7** 43644 (2017).

[23] Plaut A. S. *et al* An atomic carbon source for high temperature molecular beam epitaxy of graphene. *Carbon* **114** 579 (2017).

[24] Driver M. S., Beatty J. D., Olanipekun O., Reid K., Rath A., Voyles P. M. and Kelber J. A. Atomic layer epitaxy of h-BN(0001) multilayers on Co(0001) and molecular beam epitaxy growth of graphene on h-BN(0001)/Co(0001). *Langmuir* **32** 2601 (2016).

[25]Zheng R., Khanaki A., Tian H., He Y., Cui Y., Xu Z. and Liu J. Precipitation growth of graphene under exfoliated hexagonal boron nitride to form heterostructures on cobalt substrate by molecular beam epitaxy. *Appl. Phys. Lett.* **111** 011903 (2017).

[26]Xu Z., Zheng R., Khanaki A., Zuo Z. and Liu J. Precipitation growth of graphene under exfoliated hexagonal boron nitride to form heterostructures on cobalt substrate by molecular beam epitaxy. *Appl. Phys. Lett.* **107** 213103 (2015).

[27]Zuo Z., Xu Z., Zheng R., Khanaki A., Zheng J.-G and Liu J. In-situ epitaxial growth of graphene/h-BN van der Waals heterostructures by molecular beam epitaxy. *Sci. Rep.* **5** 14760 (2015).

[28]Xu Z., Khanaki A., Tian H., Zheng R., Suja M., Zheng J.-G. and Liu J. Direct growth of hexagonal boron nitride/graphene heterostructures on cobalt foil substrates by plasma-assisted molecular beam epitaxy. *Appl. Phys. Lett.* **109** 043110 (2016).

[29]Ishida K. and Nishizawa T. The C-Co(Carbon-Cobalt) system. *J. Phase Equilib.* **12** 417 (1991).

[30] Zheng M. *et al* Metal-catalyzed crystallization of amorphous carbon to graphene *Appl. Phys. Lett.* **96** 063110 (2010).

[31] Kassab L. R. P., Martinelli J. R., dos Santos A. D., Ribeiro S. J. L. and dos Santos M. V. Characterization of thin carbon films produced by the magnetron sputtering technique. *Mater. Res.* **19** 669 (2016).

[32] McCarty K. F., Feibelman P. J., Loginova E. and Bartelt N. C. Kinetics and thermodynamics of carbon segregation and graphene growth on Ru (0001) *Carbon* **47** 1806 (2009).

[33] Baraton L., He Z. B., Lee C. S., Cojocaru C. S., Châtelet M., Maurice J-L., Lee Y. H. and Pribat D. On the mechanisms of precipitation of graphene on nickel thin films. *Europhys. Lett.* **96** 46003 (2011).

[34] Hamilton J. C. and Blakely J. M. Carbon segregation to single crystal surfaces of Pt, Pd and Co. *Surf. Sci.* **91** 199 (1980).

[35] Hu X., Björkman T., Lipsanen H., Sun L. and Krasheninnikov A. V. Solubility of boron, carbon, and nitrogen in transition metals: getting insight into trends from first-principles calculations. *J. Phys. Chem. Lett*. **6** 3263 (2015).

[36] Luo J., Tian P., Pan C.-T., Robertson A. W., Warner J. H., Hill E. W. and Briggs G. A. D. Ultralow secondary electron emission of graphene. *ACS Nano* **5** 1047 (2011).

[37] Ci L. *et al* Atomic layers of hybridized boron nitride and graphene domains. *Nat. Mat.* **9** 430 (2010).

[38] Zheng R., Xu Z., Khanaki A., Tian H., Zuo Z., Zheng J.-G. and Liu J. Low-temperature growth of graphene on iron substrate by molecular beam epitaxy. *Thin Solid Films* **627** 39 (2017).

[39] Xu Z., Tian H., Khanaki A., Zheng R., Suja M. and Liu J. Large-area growth of multi-layer hexagonal boron nitride on polished cobalt foils by plasma-assisted molecular beam epitaxy. *Sci. Rep.* **7** 43100 (2017).

[40] Tonkikh A. A, Voloshina E. N., Werner P., Blumtritt H., Senkovskiy B., Güntherodt G., Parkin S. S. P. and Dedkov Y. S. Structural and electronic properties of epitaxial multilayer h-BN on Ni (111) for spintronics applications. *Sci. Rep*. **6** 23547 (2016).

[41] Gorbachev R. V. *et al* Hunting for monolayer boron nitride: optical and Raman signatures. *Small* **7** 465 (2011).

[42] Barr T. L. and Seal S. Nature of the use of adventitious carbon as a binding energy standard *J. Vac. Sci. Technol., A* **13.3** 1239 (1995).

[43] Choi D. S., Kim K. S., Kim H., Kim Y., Kim T. Y., Rhy S.-H., Yang C.-M., Yoon D. H. and Yang W. S. Effect of cooling condition on chemical vapor deposition synthesis of graphene on copper catalyst. *ACS Appl. Mater. Interfaces* **6** 9574 (2014).

[44] Zhao P., Kumamoto A., Kim S., Chen X., Hou B., Chiashi S., Einarsson E., Ikuhara Y. and Maruyama S. Self-limiting chemical vapor deposition growth of monolayer graphene from ethanol. *J. Phys. Chem. C* **117** 10755 (2013).

[45] Takesaki Y., Kawahara K., Hibino H., Okada S., Tsuji M. and Ago H. Highly uniform bilayer graphene on epitaxial Cu–Ni (111) alloy *Chem. Mat.* **28** 4583 (2016).

[46] Orofeo C. M., Suzuki S., Kageshima H. and Hibino H. Growth and low-energy electron microscopy characterization of monolayer hexagonal boron nitride on epitaxial cobalt. *Nano Res.* **6** 335 (2013).

[47] Shi Y. *et al* Synthesis of few-layer hexagonal boron nitride thin film by chemical vapor deposition *Nano Lett.* **10** 4134 (2010).

[48] Jang S. K., Youn J., Song Y.J. and Lee S. Synthesis and characterization of hexagonal boron nitride as a gate dielectric. *Sci. Rep*. **6** 30449 (2016).

[49] Preobrajenski A. B., Vinogradov A. S. and Mårtensson N. Monolayer of h-BN chemisorbed on Cu(111) and Ni(111): The role of the transition metal 3d states. *Surf. Sci.* **582** 21. (2005).

[50] Morscher M., Corso M., Greber T. and Osterwalder J. Formation of single layer h-BN on Pd(111). *Surf. Sci.* **600** 3280 (2006).

[51] Stobinski L., Lesiak B., Malolepszy A., Mazurkiewicz M., Mierzwa B., Zemek J., Jiricek P. and Bieloshapka I. Graphene oxide and reduced graphene oxide studied by the XRD, TEM and electron spectroscopy methods. *J. Electron. Spectrosc. Relat. Phenom*. **195** 145 (2014).

[52] Bhimanapati G. R., Kozuch D. and Robinson J. A. Large-scale synthesis and functionalization of hexagonal boron nitride nanosheets. *Nanoscale* **6** 11671 (2014).

[53] Chioncel F. M. and Haycock W. P. Structural characterization of cobalt thin films grown by metal-organic CVD. *Chem. Vap. Deposition* **11** 235 (2005).

[54] Khanaki A., Xu Z., Tian H., Zheng R., Zuo Z., Zheng J.-G. and Liu J. Self-assembled cubic boron nitride nanodots. *Sci. Rep*. **7** 4087 (2017).

[55] Zhang C., Zhao S., Jin C., Koh A. L., Zhou Y., Xu W., Li Q., Xiong Q., Peng H. and Liu Z. Direct growth of large-area graphene and boron nitride heterostructures by a co-segregation method. *Nat. Commun*. **6** 6519(2015).

[56] Meng J. H., Zhang X. W., Wang H. L., Ren X. B., Jin C. H., Yin Z. G., Liu X. and Liu H. Synthesis of in-plane and stacked graphene/hexagonal boron nitride heterostructures by combining with ion beam sputtering deposition and chemical vapor deposition. *Nanoscale* **7** 16046 (2015).

[57] Ji Y. *et al* Boron nitride as two-dimensional dielectric: reliability and dielectric breakdown. *Appl. Phys. Lett*. **108** 012905 (2016).

[58] Britnell L. *et al* Electron tunneling through ultrathin boron nitride crystalline barriers. *Nano Lett.* **12** 1707 (2012).

[59] Hui F., Pan C., Shi Y., Ji Y., Grustan-Gutierrez E. and Lanza M. On the use of two-dimensional hexagonal boron nitride as dielectric. *Microelectron. Eng.* **163** 119 (2016).

[60] Hattori Y., Taniguchi T., Watanabe K. and Nagashio K. Comparison of device structures for the dielectric breakdown measurement of hexagonal boron nitride. *Appl. Phys. Lett.* **109** 253111 (2016).

Chapter 3: The role of carbon interstitials in Co on controllable synthesis of high-quality large-area two-dimensional hexagonal boron nitride layers

3.1. Introduction

Hexagonal boron nitride (h-BN), a two-dimensional (2D) isostructure of graphene (G), has gained significant attention for its remarkable properties [1-4], as well as potentials as a 2D dielectric [5-10] and ultraviolet optics material [4,11-13]. To realize the technological potential of h-BN, the key is reliable and controllable synthesis of large-area h-BN. Toward this direction, tremendous effort has been made on chemical vapor deposition (CVD) of h-BN on various catalytic transition metal substrates, including Cu [3,14-16], Ni [17-19], Fe [20-22], Ru [23] and Pt [24,25]. Experiments have proved that transition metals could provide favorable chemical environment for the synthesis of high-quality graphene and h-BN. In addition, rational engineering of catalytic effect of the transition metal substrates by alloying or incorporating additional species has been utilized in the growth of both h-BN and G to enhance the control over layers' number, nucleation density and domain size [20,21,24,26,27]. Recently, CVD growth of G and h-BN assisted by carbon in the form of α-C or hydrocarbon gas has been reported by pre-depositing PMMA [28] or simultaneously introducing methane [29], respectively. Nevertheless, the growth of h-BN on transition metal substrates incorporated with any alien impurities such as carbon has not been studied. Transition metals with high carbon solubility are commonly thought to be detrimental for G growth, due to the precipitation of low-quality graphitic structure during substrate cooling, resulting in poor layers' number controllability [30]. However, from a completely

different perspective, the high carbon solubility of metals ensures the presence of a substantial amount of dissolved carbon atoms as interstitials. As a result, the tuning of carbon concentration in a wide range within the carbon solubility's limit can bring a whole new dimension of control for the growth of h-BN in addition to other regular growth parameters such as substrate temperature, growth pressure, surface roughness, and so on. Thus, to elucidate the effect of interstitial carbon on the growth of h-BN, it is critical to control the carbon concentration precisely in a trace level that does not end up with precipitating onto the metal surface. From this standpoint, molecular beam epitaxy (MBE), an alternative to CVD, has the ability to control precisely over the growth parameters. Moreover, it has been proved to be a reliable method to grow 2D h-BN and h-BN/graphene heterostructures [31-34]. For example, in our group, we have demonstrated the growth of 5-6 nm h-BN film on polished Co foil substrates by MBE (Figure 3.1) [32].

In this work, we carefully prepared Co substrate with different carburization time using acetylene gas prior to the growth of h-BN in a plasma-assisted MBE system. The dissolution of carbon atoms in Co enabled and enhanced the growth of h-BN on Co surface. Intensive scanning electron microscopy (SEM) study of h-BN grown on Co with different carburization conditions shows that the morphology as well as the lateral growth speed of h-BN domains can be readily controlled by carbon concentration. The morphology vastly varies from 2D layer-plus-3D islands to homogeneous 2D layers. Comprehensive characterizations including transmission electron microscopy (TEM), Raman spectroscopy, atomic force microscope (AFM), UV-Vis absorption spectroscopy and X-ray photoelectron spectroscopy (XPS) were carried out to study the structural and

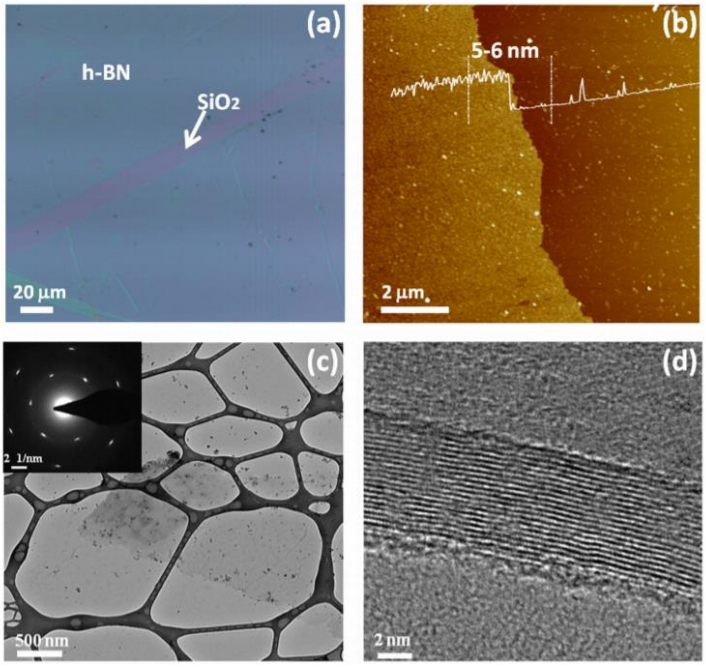

Figure 3.1. Growth of multilayer h-BN on Co foil substrate by MBE. (a) Optical micrograph and (b) AFM image of the transferred h-BN film on SiO_2 showing a h-BN thickness of 5-6 nm. (c) Plan-view TEM image of the transferred h-BN film on a TEM grid. Inset is an electron diffraction pattern, showing the six-fold symmetry of h-BN film. (d) High-resolution TEM image showing multi-layer nature of the h-BN film near its folded edge [32].

compositional properties of the samples. H-BN dielectric properties were characterized based on Co(foil)/h-BN/Co(contact) two-terminal devices. Density function theory (DFT) studies revealed the enhanced adsorption of both B and N atoms on the Co metal surface because of embedded carbon interstitials, leading to the homogeneous large-area 2D h-BN.

3.2. Experimental details

Substrate preparation: Co foils with a thickness of 0.1 mm and a purity of 99.995% from Alfa Aesar were polished on a SBT 920 Lapping and Polishing workstation and cut into 1

cm × 1 cm pieces as substrates. These pieces were degreased and deoxidized with acetone, IPA and diluted hydrochloric acid (10%), rinsed in deionized (DI) water, blown dry and finally loaded into an MBE chamber. Negligible amount of carbon impurity existed in as-received Co foils (0-6 ppm according to Alfa Aesar' glow discharge mass spectrometry report). Co substrates without carburization process are referred as carbon-free Co.

Hydrogen annealing and carburization: A re-designed Perkin-Elmer MBE system with a background pressure of ~10^{-9} Torr was used for the sample growth. The substrate was heated to 900 ºC and annealed at this temperature under a 10-sccm flow of hydrogen gas for 10 minutes. Then, 0.5-sccm C_2H_2 gas was introduced into chamber with a pressure of 5×10^{-5} Torr for 15 to 240 s to enrich Co with carbon prior to h-BN growth. H-BN growth step started immediately after the carburization process.

H-BN growth: A Knudsen effusion cell filled with B_2O_3 powder (Alfa Aesar, 99.999% purity) was used as boron (B) source Nitrogen plasma (Airgas, 99.9999% purity) generated by an electron cyclotron resonance (ECR) system and high-purity ammonia (American Gas Group, 99.9995% purity) were used as nitrogen (N) sources. The h-BN growth was conducted by simultaneous introduction of B and N sources onto the Co substrate at 900 ºC. B cell temperature was maintained at 1150 ºC. N source consisting of 10-sccm N_2 gas through an ECR plasma source and NH_3 gas at a flow rate of 5 sccm through a shut-off valve were introduced to the chamber. The ECR current was set at 60 mA with a power of 228 W. The growth pressure was on the order of 6×10^{-4} Torr. After the growth, the samples were cooled to room temperature at a rate of 10 ºC/min. Detailed growth conditions are

summarized in Table 3.1. Figure 3.2 shows a schematic of the typical 2D h-BN growth process via Co carburization approach by MBE.

Transferring of h-BN samples: The transferring process of the epitaxial h-BN films from the substrates was carried out by the typical wet transferring method [35]. The Co substrate was etched by $FeCl_3$/HCl solution after spin-coating PMMA (495 A4) on as-grown samples. The PMMA/h-BN stack was then transferred into 10% HCl, 5% HCl and DI water successively to rinse out the residual etchant. Then, the floating h-BN film was taken out

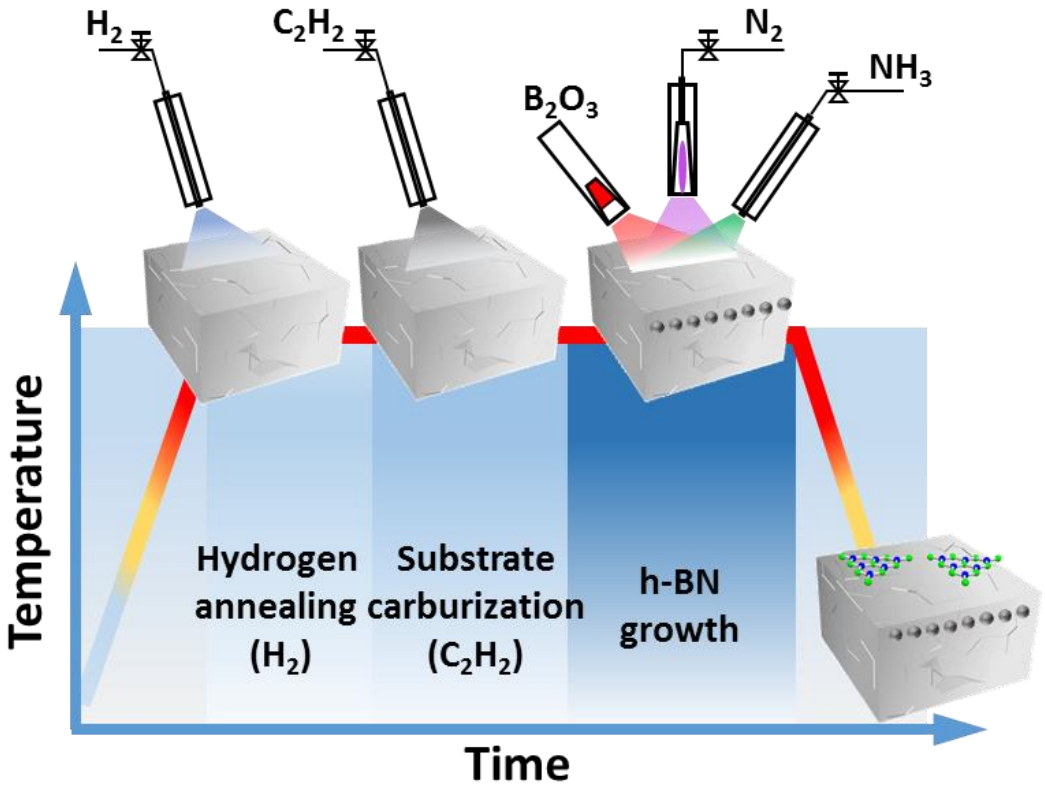

Figure 3.2. Schematic of MBE growth steps. Five colored regions indicate five growth steps including ramping-up, hydrogen annealing, substrate carburization, h-BN growth and cooling.

by desired substrates and left to dry for at least 12 hours. Thereafter, a few drops of PMMA were deposited again on the transferred film and soaked for another two hours. These additional drops of PMMA soften the previous PMMA layer and enhance the attachment of h-BN on the substrate. PMMA was removed by dipping the sample into acetone bath. Finally, the sample was annealed at 400 °C inside a CVD furnace for 3 hours in Ar/O_2 flow of 300 sccm to remove any remaining organic residue.

Characterizations: SEM images were acquired using an FEI NNS450 system in secondary electron (SE) imaging mode with a beam voltage of 10 kV. Raman characterizations were performed using a HORIBA LabRam system equipped with a 60-mW, 532-nm green laser. XPS characterization was conducted using a Kratos AXIS ULTRA XPS system equipped with an Al Kα monochromatic X-ray source and a 165-mm mean radius electron energy hemispherical analyzer. AFM images were obtained using a Veeco D5000 AFM system. TEM images and selected area electron diffraction (SAED) patterns were acquired using a FEI Tecnai12 system. TEM sample was prepared by picking a transferred h-BN film using a lacey carbon coated Cu TEM grid.

Device fabrication and electrical measurement: Co(foil)/h-BN/Co(contact) two-terminal devices were fabricated by a standard photolithography and lift-off process. A Co layer of 100 nm was patterned as top square contacts with an edge length of 200 μm on the surface of as-grown h-BN film. Reactive ion etching (RIE) was performed with a 50-sccm SF_6 plasma, under a power of 50 W, and for 15 seconds to etch the h-BN film between devices, which ensured isolation of different devices on the same substrate. Current-voltage

(I-V) characteristics were obtained by an Agilent 4155C semiconductor parameter analyzer equipped with probing tips having a diameter of about 5 μm (Signatone, SE-TL).

DFT calculations: Theoretical calculations were based on first-principles density functional theory (DFT) using projector augmented wave method and the Perdew-Burke-Ernzerhof (PBE) type generalized gradient approximation [36,37] as implemented in the software package VASP [38]. Spin polarization was included self-consistently in all calculations. For the unit cell calculations, a Monkhorst-Pack scheme was adopted to integrate over the Brillouin zone with a k-mesh of 9×9×1. A plane-wave basis cutoff of 550 eV was used. All structures were optimized until the largest force on the atoms was less than 0.01 eV/Å. To model the adsorption energies of B and N atoms on Co (111) surface, single B or N atom was assumed to be on the specific sites on the surface of a supercell consisting of four atomic layers of 4×4 Co atoms in the (111) plane. These specific sites include the top of the Co atoms, hexagonal closely packed (HCP), and face centered cubic (FCC) sites of the Co (111) surface, on which the settlement of B and N atoms would enable epitaxial relationship between h-BN and Co (111) substrate. A gap of 15 Å was introduced to avoid interactions between the periodically repeated surfaces.

3.3. Results and discussion

Table 3.1 summarizes the growth conditions of all h-BN samples grown on carbon-free Co and carburized Co substrates. Sample A is carbon-free Co and our reference sample. Samples B1-B5 are h-BN samples grown with different growth time on the same 60-s carburized Co substrates. C1-C4 are carbon concentration dependent samples with 1-

Table 3.1. Summary of growth conditions for different h-BN samples.

Step	Parameters	Sample A	Sample B1-B5	Sample C1-C4	Sample D1-D7
Hydrogen Annealing	Temperature (°C)	900	900	900	900
	Hydrogen gas flow (sccm)	10	10	10	10
	Duration (mins)	10	10	10	10
Carburization	Temperature (°C)	--	900	900	900
	Acetylene gas flow (sccm)	--	0.5	0.5	0.5
	Duration (s)	--	60	***60, 120, 180, 240***	***15, 30, 45, 60, 120, 180, 240***
H-BN Growth	Substrate temperature (°C)	900	900°	900	900
	Boron cell temperature (°C)	1150	1150	1150	1150
	Ammonia gas flow (sccm)	5	5	5	5
	Nitrogen gas flow (sccm)	10	10	10	10
	Nitrogen ECR current (mA)	60	60	60	60
	Duration (mins)	180	***15, 30, 60, 90, 180***	60	180

hr growth of h-BN. D1-D7 are carbon concentration-dependent samples with 3-hrs growth of h-BN. All the samples are grown on polished Co foils. Note that Sample B3 is just sample C1 and Sample B5 is just Sample D4. Direct growth of h-BN on carbon-free Co substrate was reported previously, however, those h-BN films were grown at a relatively low temperature of 850 °C, thus the quality of the films was good but not excellent, which is inferred from a breakdown electric field of only 3 MV/cm [32]. In this series of experiments, all samples were grown at a higher substrate temperature of 900 °C in order to enhance the quality of the films. Surprisingly, with all other growth conditions same as or similar to that of Reference 32, the attempt towards the growth of h-BN onto carbon-free Co substrate at 900 °C was not successful (i.e., Sample A), as verified by characterizations such as SEM, OM, Raman and XPS (Figure 3.3). The main reason is associated with low absorption of B species on metal surface, which is later confirmed by the theoretical calculation of absorption energy. On the other hand, h-BN has been reliably

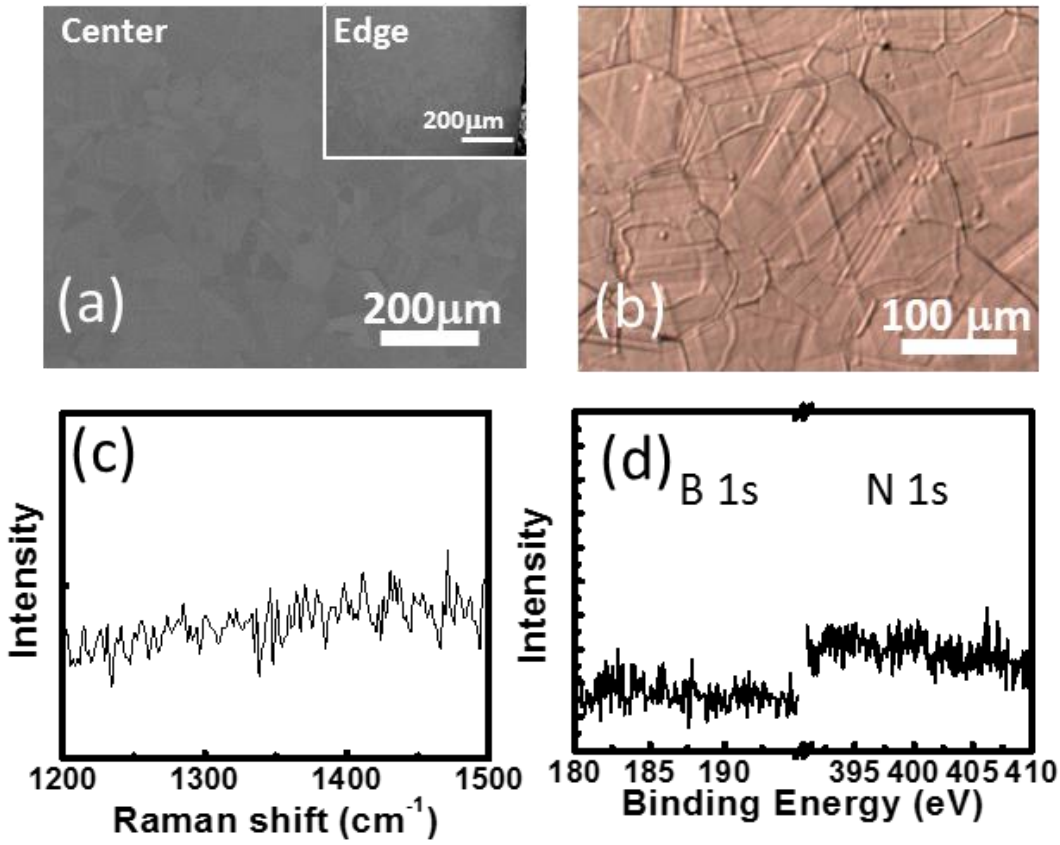

Figure 3.3. Characterization of reference sample: h-BN growth on carbon-free Co foil (Sample A). (a) SEM image in the center and edge (inset). No contrast can be observed, indicating no h-BN growth. (b) Optical microscope image of sample surface. (c) Raman spectrum. (d) XPS spectrum at B 1s and N 1s. No h-BN related signature peaks are observed.

grown onto all carburized Co substrates at 900 ºC (Samples B1-B5, C1-C4, D1-D7). Vacuum carburization has been widely used for synthesis of carbon steel by exposing iron in a hydrocarbon environment [39]. Here, carburization of Co substrates was performed by introducing 0.5 sccm C_2H_2 gas for different amount of time at the growth temperature to attain different C concentration in the Co substrates.

Figure 3.4(a) shows an SEM image of a typical sample (Sample B5) taken at its center region. Sample B5 was grown with the introduction of B and N sources for 3 hrs on a 60-sec carburized Co substrate at 900 ºC. The brighter regions correspond to prism-shape multilayer h-BN islands ("prisms" in short) due to the charging effect, and conversely darker regions indicate h-BN few-layer film. Thus, the h-BN film consists of high-density prisms atop of continuous few-layer thin film. The edge length of a typical prism is around 10 μm (Figure 3.4(a) inset). To show the contrast between thin h-BN film and Co substrate,

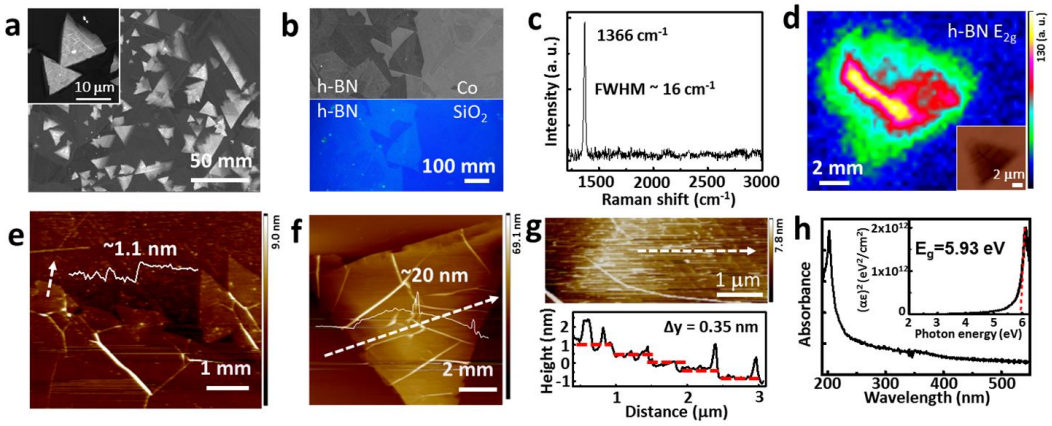

Figure 3.4. Characterization of the 3-hrs h-BN sample grown on 60-sec carburized Co substrate. (a) SEM image of the sample, showing 2D layer-plus-3D islands morphology. The inset is an image with higher magnification, indicating the size of a typical prism-shaped h-BN island. (b) SEM and optical microscope images of as-grown (top) and transferred (bottom) sample on the sample edge. (c) Raman spectrum measured at the center of a prism-shaped island. (d) Raman mapping on an as-grown prism-shaped island with corresponding optical micropscopy image shown in inset at the right bottom corner. (e) AFM image and its scan profile on the few-layer region of a transferred h-BN sample on SiO_2/Si. (f) AFM image and its scan profile across a prism-shaped island. (g) AFM image and scan profile on the side wall of a prism-shaped island. The height profile was obtainedalong the white arrow direction illustrated in the image. (h) UV-Vis absorption spectrum of a transferred h-BN sample on sapphire. Inset is $(A\varepsilon)^2$ versus ε curve.

SEM image was also taken at the edge of the sample where the density of the "prisms" is much lower (Figure 3.4(b)). The part covered by h-BN shows darker color due to the attenuation of secondary electrons emitted from Co substrate by h-BN [40]. The film is further transferred onto a Si substrate covered with a 300-nm SiO_2. Compared with the SEM image of the area on as-grown sample, the transferred film looks continuous and intact. Figure 3.4(c) shows a typical Raman spectrum of a prism on the as-grown sample, showing a characteristic E_{2g} phonon mode at 1366 cm^{-1} with a full width at half maximum (FWHM) of 16 cm^{-1}, which is comparable to the reported values of mechanically exfoliated h-BN [41]. No graphite related Raman peaks are observed within 1250 to 3000 cm^{-1}, indicating no carbon-related growth/deposition on the sample's surface. A simple selective etching experiment is designed to visualize the trace of carbon in Co substrate (Figure 3.5). From Raman spectra, the interface between Co and h-BN is confirmed to be free of C-related structure, while α-C network structure is embedded in Co grain boundaries (Figure 3.5(c)), which can be explained by insufficient carbon concentration, high carbon solubility and low carbon diffusion coefficient in Co [42].

Figure 3.4(d) shows an h-BN E_{2g} peak Raman mapping image around a prism-shaped island area (the inset is an OM image of the feature). The Raman signal is strongest in the center and becomes weaker as the mapping is away from the center, which is due to the prism shape morphology. The h-BN signal is essentially zero at the region off the prism where 2D few-layer h-BN is located. Two reasons account for this phenomenon. First, unlike other 2D materials such as graphene and transition metal dichalcogenides (TMDs), Raman signal in h-BN is relatively weak due to the non-resonant character of Raman

scattering in h-BN [43]. Second, a laser beam normal incident to a flat metal surface would form a standing wave with a node near the metal surface according to the boundary condition at metal surface (E_t=0), while the epitaxial few-layer h-BN film lays on the proximity of metal surface resulting in a much weaker Raman scattering [44]. Graphene G peak mapping in the same area (Figure 3.6) displays negligible signal, which verifies that carbon atoms have not precipitated at the h-BN/Co interface to form any graphitic structure. According to the AFM measurement, the thickness of h-BN thin film is ~1.1 nm

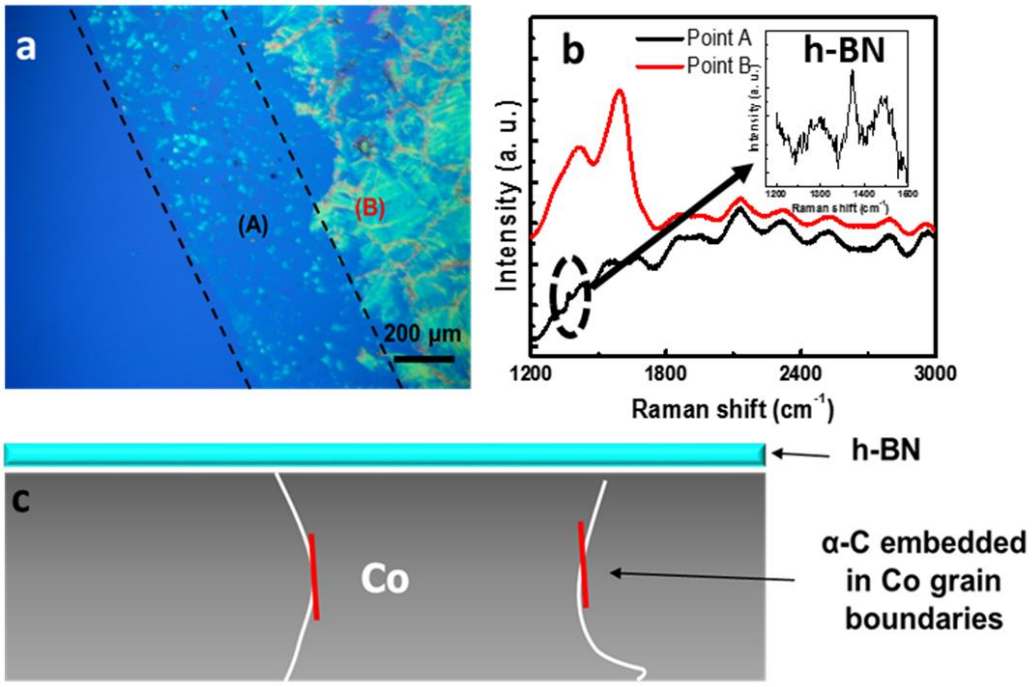

Figure 3.5. Sample with 60 sec C_2H_2 introduction prior to 3 hrs h-BN growth and transferred onto SiO_2/Si substrate under selective etching process. (a) OM image of the sample showing two distinct parts: (A) the part that the Co substrate is totally etched away and (B) the part that is still under the etching process (incomplete etching). (b) Raman spectra from point (A) (the black spectrum) and point B (the red spectrum) of (a). Inset shows a zoom-in Raman spectrum of point (A). (c) Schematic of h-BN/Co sample from a cross-sectional view.

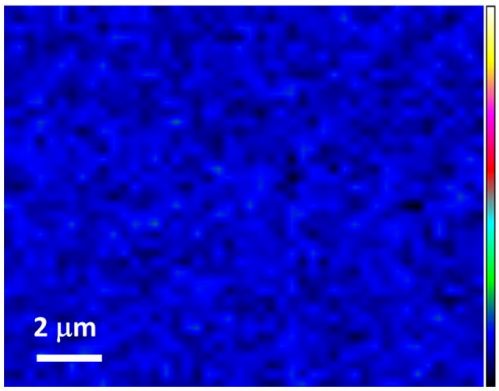

Figure 3.6. Raman mapping at graphene G peak of Sample B5 on the same area as in Figure 3.4(d).

and the height of h-BN prism is ~20 nm, as shown in Figure 3.1(e) and 3.1(f), respectively. Layered structure is clearly observed from the AFM scan profile over the side wall of the h-BN prism. The interlayer distance is measured as 0.35 nm (Figure 3.1(g)), which agrees with the theoretical interlayer distance of h-BN [45]. A strong peak at ~203 nm with a sharp absorption edge can be observed in the absorption spectrum (Figure 3.1(h)), corresponding to a band gap of ~5.93 eV for h-BN extracted from Tauc equation [31].

Figure 3.7(a-h) show SEM images of h-BN samples grown for 1-hr (Samples C1-C4) and 3-hrs (Samples D4-D7) on carburized Co substrates for 60 to 240 sec, respectively. As it can be seen from Figure 3.7(a) and (b), high-density h-BN prisms are formed on 60-sec carburized samples. By fixing the Co carburization time at 60 sec, additional samples with other h-BN growth time were grown and Figure 3.8(a-e) show SEM images of these samples. Only sparse h-BN nuclei emerge on the surface of a 15-min h-BN growth sample (Figure 3.8(a)), which suggests the time to form stable nuclei (incubation time) is around 15 minutes. Nucleation density increases rapidly in the next 15-minute growth following

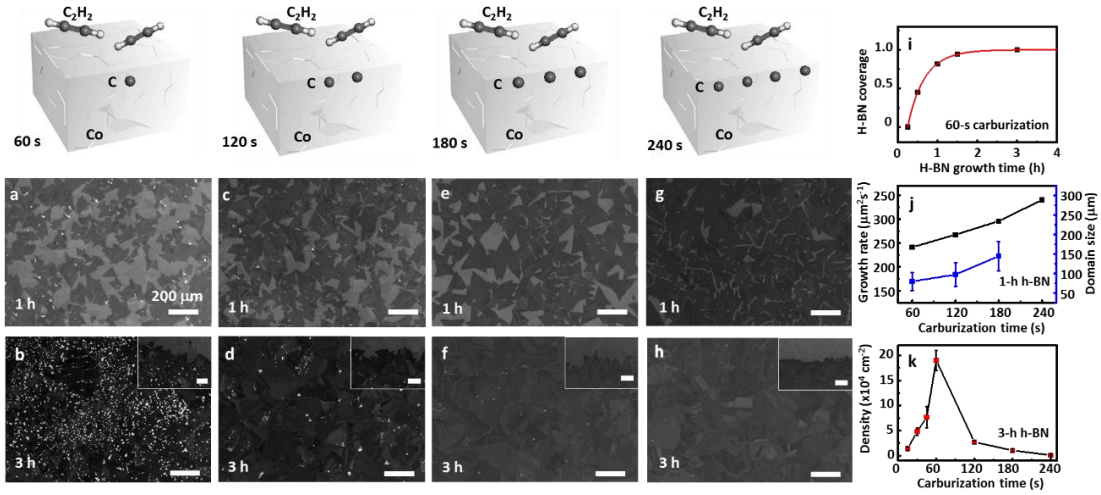

Figure 3.7. Morphology evolution of h-BN as a function of Co carburization time. Schematic shows that carbon concentration is controlled by carburization process duration. (a-h) Large-area SEM images of (a, c, e, g) 1-hr h-BN samples (C1, 2, 3, 4) and (b, d, f, h) 3-hrs h-BN samples (D4, 5, 6, 7) on carburized Co substrate for 60, 120, 180, and 240 sec, respectively. Insets in (b, d, f, h) show the edge area for contrast. All scale bars in the images represent 200 μm. (i) Plot of h-BN fractional coverage as a function of h-BN growth time with carburization time fixed at 60 s, fitted with the JMAK model in red. (j) Plot of lateral growth rate and domain size of 1-hr h-BN samples as a function of carburization time from 60 to 240 sec. The lateral growth rate is calculated from the h-BN covered area per unit time on 1386 × 990 μm^2 of each sample. The domain size measurement is not available for 240-sec carburized sample due to coalescence of domains. (k) Density of prism-shaped island in the 3-hrs h-BN samples as a function of carburization time.

the incubation period (Figure 3.8(b)). After certain surface coverage, the size of most h-BN domains increases as incoming ad-atoms are more likely to be captured by existing h-BN flake edges (Figure 3.8(c, d)). Co surface is almost fully covered after 90 minutes of growth. B and N ad-atoms start to nucleate and grow on top of existing layers, favorably on the defects and atomic steps. Finally, continuous 2D layers-plus-3D islands are formed for the sample grown for 3 hours (Figure 3.8(e)). The lateral growth is further studied under

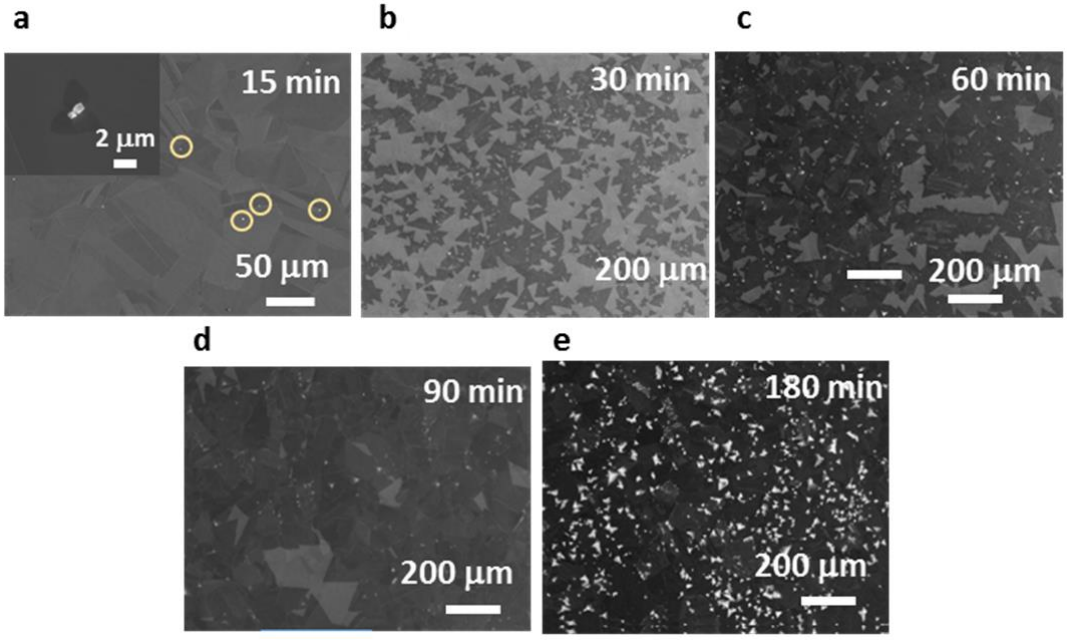

Figure 3.8. H-BN time-dependent growth with 60-sec carburization of Co substrate (Samples B1-B5). (a-e) SEM images of h-BN samples grown for 15, 30, 60, 90, and 180 min, respectively. Yellow circle in (a) indicates small nuclei of h-BN. The inset shows an enlarged image of an individual h-BN nucleus.

the framework of Johnson-Mehl-Avrami-Kolmogorov (JMAK) model. Figure 3.7(i) plots the h-BN coverage versus its growth time. H-BN coverage on Co was obtained by using ImageJ software, as detailed in Figure 3.9, can be fitted by an exponential curve according to the JMAK model [46,47]:

$$A_{BN} = 1 - \exp(k(t - t_0)^n) \qquad (1),$$

where A_{BN} is the h-BN fractional coverage. K is the rate constant, which depends on both the nucleation rata and domain growth rate. The index n is the Avrami exponent, which is related to the dimensionality of the system and time-dependent nucleation and growth rate. It can be expressed as n = qd+B, where q equals 1 for linear growth (reaction controlled) or 1/2 for parabolic growth (diffusion controlled), and d stands for the dimensionality of

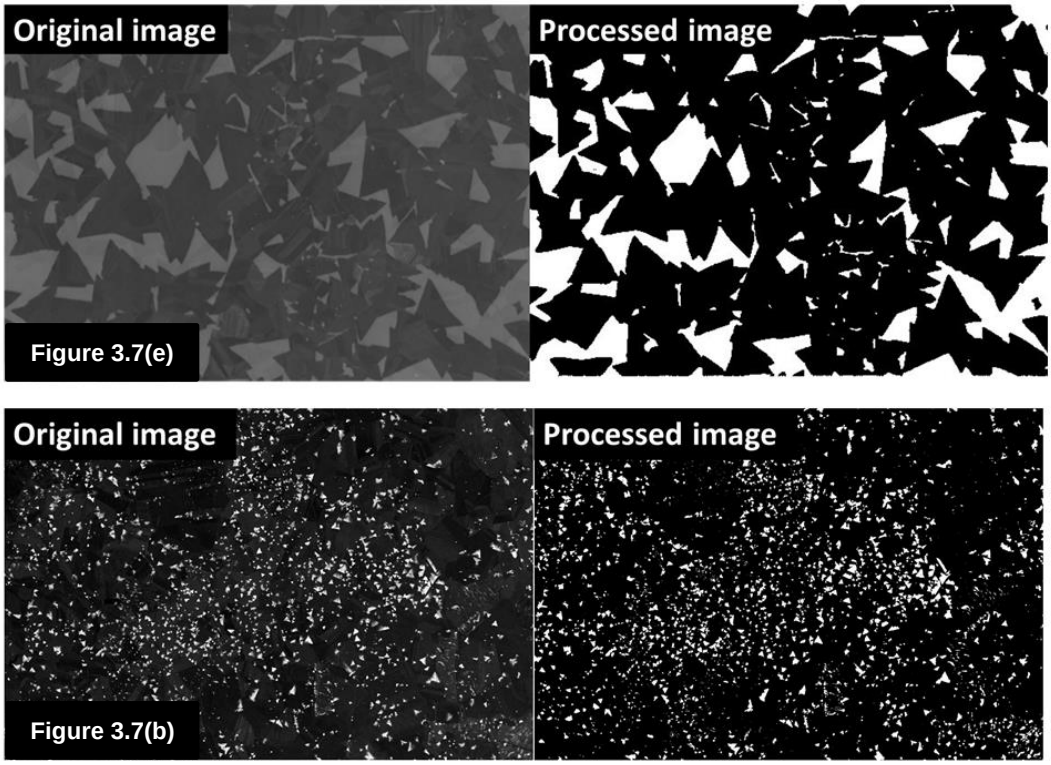

Figure 3.9. Comparison between Figure 3.7(e) and Figure 3.7(b) with corresponding ImageJ software processed images.

the growth; B is 0 for site-saturated nucleation and 1 for continuous nucleation with constant rate. An $n = 0.96 \pm 0.05$ is extracted from fitting of experimental data, suggesting a 2D diffusion controlled growth with site-saturated nucleation [48].

With the change of carburization time from 60 to 240 sec, the morphology of h-BN films grown for the same growth time of 1 hr is evidently different as shown in Figure 3.7 (a), (c), (e), and (g). H-BN flakes appear as dark features and increase in size and coverage as the carburization time increases. Figure 3.7(j) shows the average h-BN domain size and lateral growth rate as a function of carburization time for these 1-hr h-BN samples. The

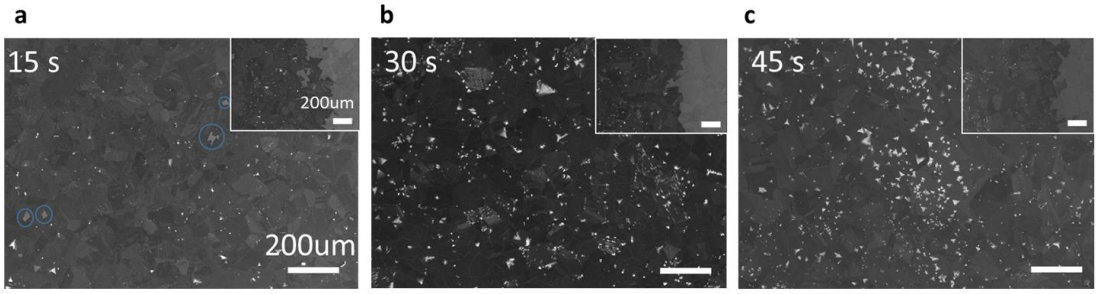

Figure 3.10. Additional SEM images of 180-mins h-BN samples. (a-c) SEM image of samples with (a) 15-, (b) 40- and (c) 45-s carburization time. H-BN pinholes are circled in blue in (a). Insets show the edge area for contrast. The scale bars in all images are 200 μm.

domain size increases from ~80 to ~144 μm as the carburization time increases from 60 to 180 sec. For the sample with a 240-sec carburization time (Figure 3.7(g)), h-BN domains coalesce and almost fully cover the Co surface. The lateral growth rate increases as the carburization time increases.

As the h-BN growth time is extended to 3 hrs, the entire Co surface of all samples with different carburization time is covered by continuous 2D h-BN films, as seen from the SEM images in Figure 3.7(b), (d), (f), (h) and Figure 3.10. Additional 3D h-BN prism-shaped islands are also formed on top of the 2D layers in some of these samples, which are clearly related to the carburization time. Figure 3.7(k) shows the density of h-BN prisms as a function of carburization time. The density of h-BN prisms decreases from 1.9×10^5 cm^{-2} to roughly zero as the Co carburization time increases from 60 to 240 sec. In contrast, the density of prisms increases gradually for shorter carburization time from 15 to 60 sec. As it is discussed later, the incorporation of interstitial carbon in Co essentially enables the nucleation and growth of h-BN. As interstitial carbon content is low in these samples with

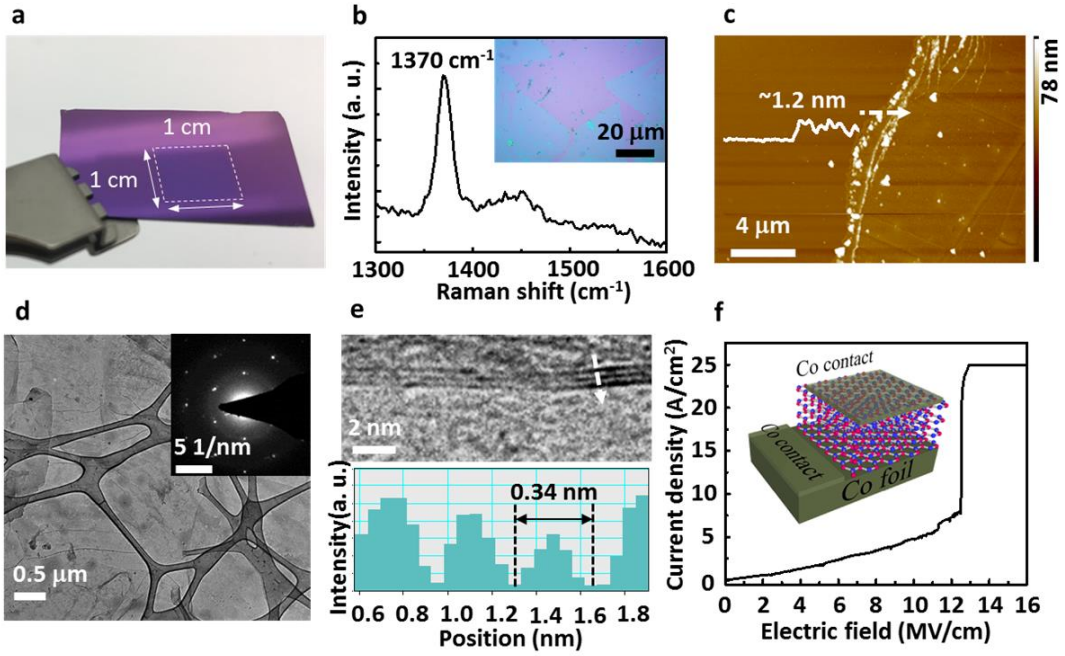

Figure 3.11. Characterization of an h-BN few-layer sample (Sample D7). (a) photograph of h-BN sample transferred onto SiO_2/Si substrate showing the film size of 1 cm × 1 cm. (b) Raman spectrum measured on the transferred h-BN few-layers on SiO_2/Si. The inset displays OM image of the corresponding sample. (c) AFM image and profile across the edge of transferred thin h-BN film. **d**, plane-view TEM image of h-BN sample transferred onto a lacey carbon coated copper grid, with SAED pattern shown in the top right corner inset. **e**, TEM image at the edge of the h-BN sample with intensity scan across the white line shown below. **f**, current density versus electric field of a Co(foil)/h-BN/Co(contact) two-terminal device. The inset displays a schematic of the device structure.

the carburization time less than 60 sec, the absorption of both B and N atoms is weak, the nucleation mainly relies on defects and imperfection sites on the surface, which facilitates vertical growth of prisms. As interstitial carbon content increases in the samples with carburization time larger than 60 sec, the abundance of B and N atoms on the surface because of the enhanced adsorption facilitates the nucleation of h-BN domains. Combined

with a larger lateral growth rate, prism-like island formation is further suppressed, leading to the dominant growth of 2D layers.

Figure 3.11(a) shows a photograph of a homogeneous few-layer h-BN sample (Sample D7). Figure 3.11(b) shows Raman spectrum of the transferred sample with a sharp E_{2g} phonon mode at 1370 cm^{-1} and FWHM of ~16 cm^{-1}. The inset shows an OM image of the transferred film onto a SiO_2/Si substrate. Excellent contrast is observed, indicating the large-area uniform film. Figure 3.11(c) shows an AFM image of the transferred film with a scan profile across a flake edge in the inset. The thickness of the h-BN film is measured as ~1.2 nm. Figure 3.11(d) shows a plan-view TEM image of the h-BN film transferred onto a lacey carbon grid and the inset is its corresponding 6-spot SAED pattern, indicating high crystallinity. Further TEM analysis of the film edge shows that the film consists of three layers (Figure 3.11(e)). The interlayer distance is measured ~0.33 nm as shown in the intensity scan along the white arrow, which is corresponding to the h-BN (0001) crystal planes. This result is in a good agreement with the AFM result shown in Figure 3.11(c).

Figure 3.11(f) shows current density versus electric field of a Co(metal contact)/h-BN/Co(foil) two-terminal device with a metal contact size of 200×200 μm^2 based on a 240-sec carburized h-BN sample (Sample D7). The thickness of the 2D h-BN is considered as ~1 nm according to the observation of a 3-layer film by TEM imaging (AFM result gives a slightly larger thickness of ~1.2 nm due to tip effect). The current-voltage characteristic clearly exhibits a quasi-linear relationship at the low and moderate voltage regions due to direct tunneling [49] and a dielectric breakdown. As shown in Figure 3.11(f), the breakdown electric field is about 12.5 MV/cm. This number is more than four times larger

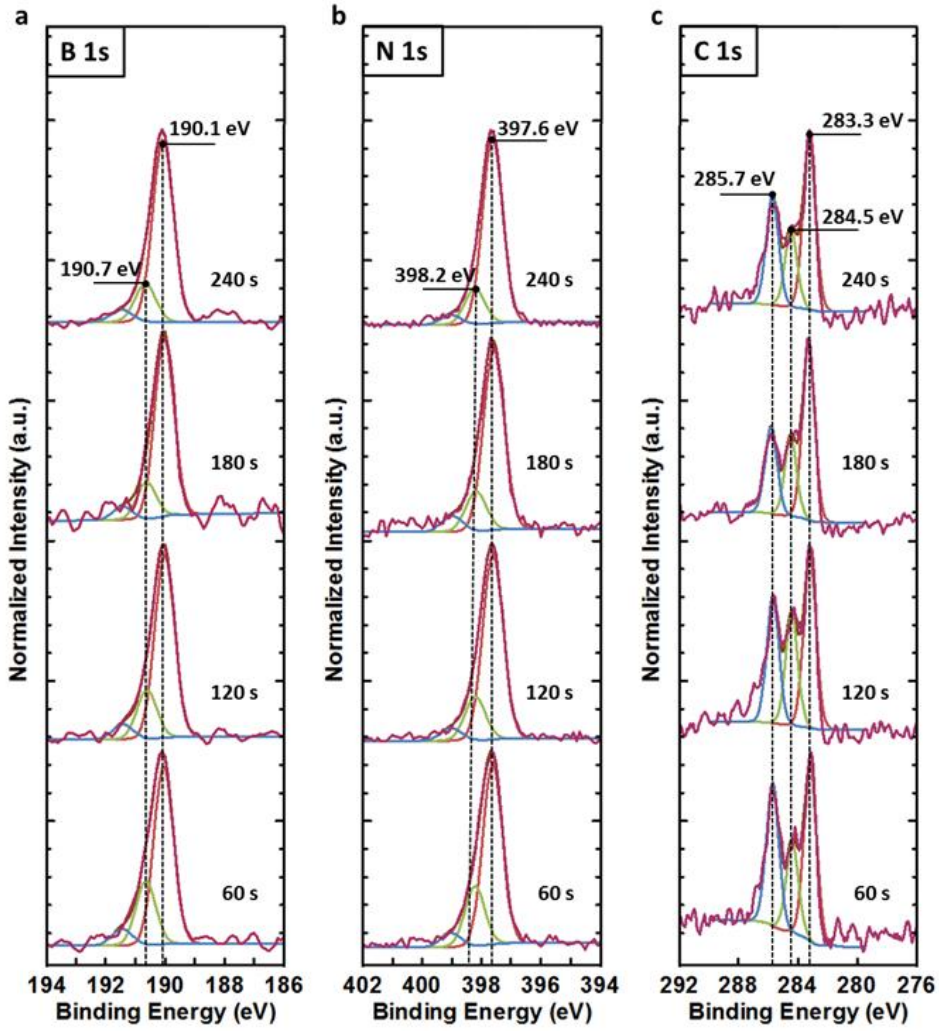

Figure 3.12. XPS of 1-hr h-BN samples with different carburization time. (a-c) XPS spectra of surface resolved (a) B1s, (b) N1s, and (c) subsurface C1s after removal of h-BN layer and surface contamination by 60-sec Ar ion sputtering of the h-BN samples with 60-, 120-, 180- and 240-sec carburization time from bottom to top.

than that of our earlier devices based on h-BN films without carburization [32], suggesting significantly improved quality of the h-BN here.

Figure 3.12(a) and (b) show B1s, and N1s XPS spectra of h-BN samples C1, C2, C3, and C4 which were grown for 1 hr with carburization time from 60 to 240 sec, respectively.

The B1s (N1s) peak can be fitted into two peaks at slightly different binding energy (BE), with a dominant peak at a lower BE of 190.1(397.6) eV as well as a small peak at a higher BE of 190.7(398.2) eV. The dominant lower-BE peak can be assigned to sp^2 B-N bond for hexagonal phase BN [50]. The higher-BE peak can be assigned to local cubic-like sp^3 bonds [51-53]. The difference in BE between the two peaks is ~0.6 eV, which is also close to the reported values of 0.82 eV for B and 0.89 eV for N [53]. As seen from Figure 3.12(a) and 3.12(b), the relative intensity of the 190.7(398.2) eV pair is the largest in 60-sec carburized sample. As the carburization time increases, the relative intensity of the high-BE peak decreases and almost vanishes in 180- and 240-sec carburized samples. This result suggests the decrease of sp^3 bonds as the increase of the carburization time. Complementarily, the relative intensity of the lower BE pair (sp^2 bond phase) is inversely correlated to the prism density of each sample. This implies that the sp^3 bonds possibly exist in the prisms, seeding the vertical growth of multilayer islands, in particular in the low-carburized samples. The increase of interstitial carbon suppresses the formation of sp^3 type of bonds and promotes the lateral growth of h-BN layers in higher-carburized samples. The stoichiometry of these as-grown films were calculated to have a B:N ratio between 1.05:1 and 1:1.06, which are essentially ~1:1 within the experimental error of the XPS sensitivity factors and peak fitting.

Figure 3.12(c) shows XPS C1s spectra of samples C1, C2, C3, and C4 after 60-sec Ar ion sputtering. As seen from Figure 3.12(c), a major peak at 283.3 eV is close to the assignment for interstitial carbon or carbide [54-56], which indicates the presence of interstitial carbon atoms in the Co substrates. The intensity does not change much among

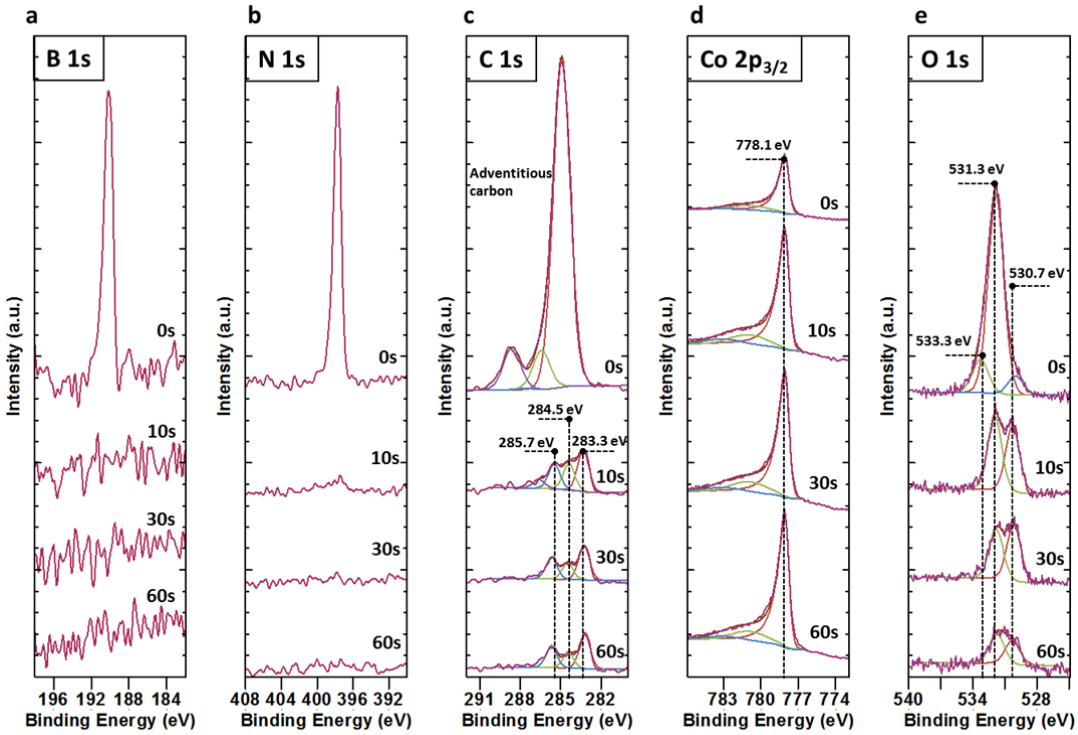

Figure 3.13. XPS depth profiling of h-BN sample with 240-sec carburization of Co substrate. (a-e) B1s (a), N1s (b), C1s (c), Co $2p_{3/2}$ (d), O1s (e) peaks with 0- 10- 30- 60-s sputtering under 3-keV Ar ion from top to bottom, respectively.

the samples due to the fact that the characterization was performed at room temperature, and the excessive carbon over the solubility level has precipitated as α-C in between Co grains. As a matter of fact, the carbon solubility in Co at our growth temperature of 900 ºC is ~1.5 at.% [57]. Thus, with different C_2H_2 flux rate and treatment time, the interstitial carbon concentration could vary between 0 and 1.5 at% in different samples at the growth temperature, leading to different morphology of the synthesized films. The peak at 284.5 eV can be assigned to C-C bond [58], which is possibly originated from α-C structure embedded in Co grain boundaries. The peak at 285.7 eV appears due to adsorbed CO molecule on Co surface [59].

The depth-resolved XPS of the 240-s carburized sample was also carried out (Figure 3.13). This sputtering was used to completely remove h-BN layers and surface carbon contamination. To evaluate the near-surface carbon information using XPS experiment, the key is to remove the adventitious carbon as well as h-BN layers on the surface. From Figures 3.13(a) and (b) it is evident that after 10-sec sputtering, majority of both B 1s and N 1s peaks are removed, while only a small peak of N 1s remains due to the high relative sensitivity factor of N 1s. After 60-sec sputtering, no h-BN related signals can be detected on the surface. The surface C 1s spectrum shows typical peaks of adventitious carbon with the main peak at 284.9 eV (Figure 3.13(c)). All major peaks are removed after 10-sec sputtering. A new peak emerges at 283.3 eV as the main peak, which can be assigned to interstitial carbon or carbide. The peak at 284.5 eV, and 285.7 eV are assigned to C-C bond as in α-C, and CO absorbed on surface, respectively. Co 2p3/2 signals show a dominate peak at 778.1 eV, which is used for binding energy calibration (Figure 3.13(d)). The surface O 1s intensity reduces significantly after 10-sec sputtering due to the fact that surface organic compound and water are removed. Then the near surface O 1s can be fitted by two peaks at 531.3 eV as the C-O peak in CO and 530.7 eV as CoO peak.

To understand the effect of Co and carburized Co on the growth of h-BN at the molecular level, ab-initio DFT simulation has been carried out. The simulation methodology is summarized in the Experimental details section (Chapter 3.2). The surface energy of the substrate σ is defined as [36-38]

$$\sigma = \frac{[E_{slab} - \sum N_i \mu_i]}{2A} \qquad (2),$$

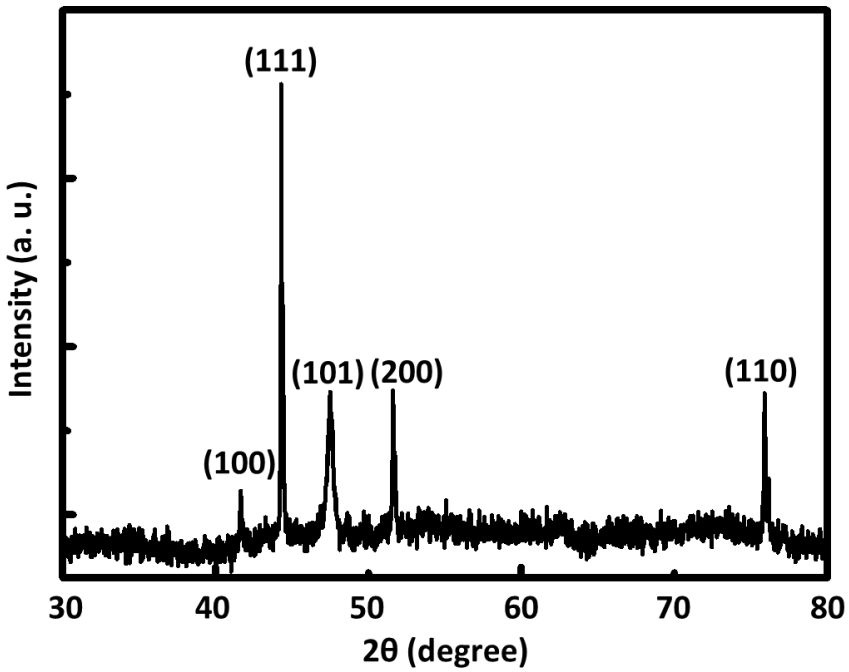

Figure 3.14. XRD pattern of 3-hrs h-BN sample with 180-sec carburization (Sample D6).

where E_{slab} is the total energy of the substrate calculated from first principles, μ_i is the chemical potential of species *i* in the slab structure, N_i is the number of particles of the *i*-th element in the slab, and A is the area of the slab. Here, Co substrates are polycrystalline with a dominant orientation of (111) plane, as can also be seen from the XRD spectrum of the 240-sec carburized sample in Figure 3.14. The DFT calculations show that Co (111) surface has a surface energy of 2037.87 mJ/m^2, compared to that of Cu (111), which is 1231.08 mJ/m^2. Cu (111) is used as a reference since h-BN can be grown on it [3,14-16]. Higher surface energy of Co (111) suggests better wettability of Co (111) as substrate.

The adsorption energy of B and N atoms on Co substrate is calculated using the following expression,

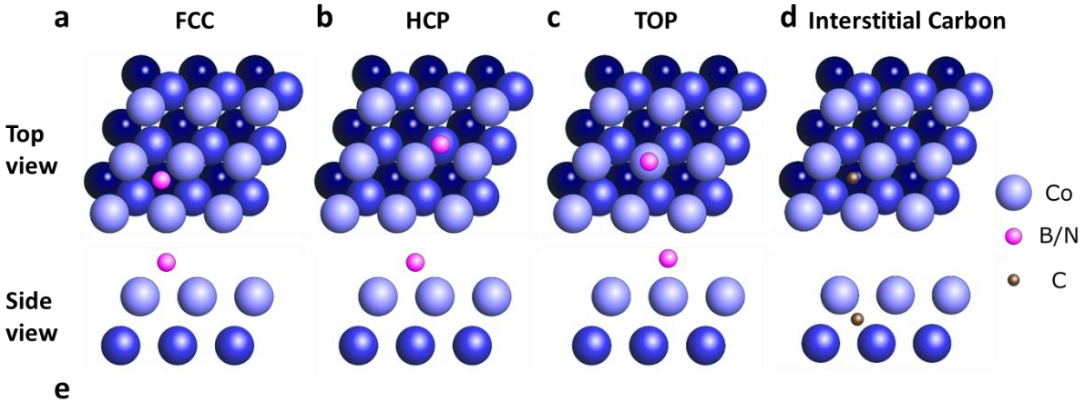

e

Adsorption Energy eV/atom	Boron			Nitrogen		
	FCC	HCP	On top	FCC	HCP	On top
Cu(111)	1.74	1.71	3.26	1.11	1.19	3.22
Co(111)	0.80	0.69	2.23	-0.26	-0.50	1.80
Co(111) With interstitial carbon	0.522	0.081	Not stable	-0.298	-1.062	Not stable

Figure 3.15. DFT calculation results of adsorption energies of B and N on Co (111) with and without interstitial carbon. (a-d) Top-view and side-view schematic of (a) B/N atoms on FCC sites, (b) B/N atoms on HCP sites, (c) B/N atoms on top of substrate atoms, and (d) interstitial carbon on an octahedral site of the substrate. (e) A summary of adsorption energies of B and N on a reference Cu (111) substrate and on Co (111) substrates with and without embedded interstitial carbon.

$$E_b = E_{B/N\,on\,surface} - E_{B/N} - E_{surface} \qquad (3)$$

where $E_{B/N\,on\,surface}$ is the total energy of a B or N atom on the surface of a supercell consisting of four layers of 4×4 Co atoms aligned in the (111) plane, $E_{B/N}$ is the chemical potential of the adsorbed B or N atom and $E_{surface}$ is the total energy of the isolated four layer 4×4 Co(111) supercell. The amplitude of the adsorption energy reflects how easy the atoms can be adsorbed/desorbed from a surface. Generally, smaller adsorption energy means higher adsorption of an atom onto a surface and a negative adsorption energy

corresponds to a stable adsorption. Figure 3.15 summarizes the DFT calculation results of adsorption energies of B and N atoms on Co (111) with and without embedded interstitial carbon on Cu (111) substrates. As seen from the top-view and side-view cartoons in Figure 3.15(a-d), in addition to the positions directly on the top of hexagonally aligned Co (or Cu) atoms, six voids within the Co (or Cu) hexagon, three of them designated as Face Centered Cubic (FCC) sites and the other three designated as Hexagonal Closely Packed (HCP) sites, are also possible positions to host either B or N atoms. On Cu (111) surface the adsorption energy of B and N are positive for all the top, HCP and FCC sites although B and N have relatively lower adsorption energies if they would stay on HCP and FCC sites, respectively. Large positive adsorption energies for B and N on Cu (111) surface suggest that h-BN should not be formed on Cu (111) unless the growth is triggered through other mechanism. The experimental demonstration of the growth of h-BN on Cu (111) was explained by the presence of preferential nucleation sites, for examples, alien atoms, atomic steps and defects, including extended defects such as grain boundaries and point defects [36-38]. On Co (111) surface, as seen from Figure 3.15(e), the adsorption energies of B and N on the three sites are significantly lower compared to Cu (111) surface. In addition, the adsorption energies of N on both HCP and FCC sites of Co surface become negative, suggesting enhanced adsorption of N atoms onto these sites of the substrate. The above comparison between Co and Cu substrates indicates that h-BN would be more likely to grow on Co under certain conditions such as at a relatively low growth temperature assuming both substrates are free of surface irregularities as preferential nucleation sites.

As the growth temperature is raised to a certain point such as 900 ºC in this case, the desorption rates of both B and N atoms on Co (111) surface become higher, leading to zero growth as shown earlier. The central theme of this work is to enable the growth of h-BN at these conditions by elevating the adsorption rates of B and N atoms on Co (111) as well using controllable carbon incorporation to modify the substrate. In XPS studies in Figure 3.12, we have shown the existence of interstitial carbon in Co. It was also reported that the octahedral sites in Co (111) are the most stable sites for interstitial carbon [60]. Thus, with the assumption of an interstitial carbon at the octahedral site in a supercell of Co (111), which is 0.6 Å below the surface, adsorption energies of different sites for B and N were calculated using the same DFT calculation method summarized in the Experimental Details section. As seen from Figure 3.15(e), except for the top site where both B and N are pushed away and hence can be considered unstable, the adsorption energies of B and N are further reduced for HCP and FCC sites compared to no interstitial carbon. In particular, B and N have the lowest adsorption energy of 0.08, and -1.06 eV/atom at the HCP sites, respectively.

From above experiment and simulation results, we can realize the growth control from the perspective of adsorption energy. On carbon-free Co samples, high and positive adsorption energy of B atoms results in a low atomic efficiency on the Co surface and, therefore, a low h-BN growth reliability. The low efficiency of atomic B is a result of both high, positive adsorption energy and high de-absorption coefficient at high growth temperature. The existence of interstitial carbon atoms in Co assists the adsorption of B and N atoms onto the Co surface and enhance the nucleation of h-BN. When interstitial

carbon concentration in Co is zero or low, the h-BN nucleation relies mostly on alien impurities and imperfections such as defects, grain boundaries, and local valleys/protrusions on the surface. This condition results in the formation of both 2D h-BN and 3D prism-shaped islands, as discussed in the XPS analysis. The competition between 2D and 3D growth modes was clearly demonstrated with the effect of carburization time on the density of prism-shaped islands. On the other hand, when interstitial carbon concentration is high, h-BN nucleation happens uniformly across the surface as a result of abundant B and N atoms on the surface. In addition, significantly increased h-BN lateral growth rate suppresses the vertical growth of 3D islands and promotes the 2D growth of uniform few-layers h-BN film.

3.4. Conclusion

A new dimension of control in the growth of h-BN by modifying Co substrate via carburization process has been achieved. Systematic SEM study of MBE grown h-BN samples on carburized Co foils is presented to reveal the h-BN nucleation and domain growth, and evolution of morphology as a function of carbon concentration. The interstitial carbon atoms in Co triggers and enhances the growth of h-BN at the given condition. Further increase of carbon concentration promotes lateral growth of h-BN few-layers and eliminates the prism-shape island formation. The lateral h-BN growth is fitted with JMAK model. Characterizations were carried out on a few-layer h-BN sample grown on a 240-s C_2H_2 treated Co substrate, revealing that tri-layer h-BN films with excellent uniformity in structural and electrical properties are formed. The growth mechanism is further studied

by DFT calculation. The adsorption energies of both B and N atoms are improved by the existence of interstitial carbon atoms, resulting a more reliable and controllable 2D crystal process compared to the growth on carbon-free Co samples. The interstitial carbon-assisted growth of h-BN film can be expanded to other synthesis tools as well as the synthesis of other 2D crystal materials.

3.5. References

[1] Liu L., Feng Y. and Shen Z. Structural and electronic properties of h-BN. *Phys. Rev. B* **68** 104102 (2003).

[2] Nag A. *et al.* Graphene analogues of BN: novel synthesis and properties. *ACS Nano* **4** 1539 (2010).

[3] Song L. *et al.* Large scale growth and characterization of atomic hexagonal boron nitride layers. *Nano Lett.* **10** 3209 (2010).

[4] Watanabe K., Taniguchi T. and Kanda H. Direct-bandgap properties and evidence for ultraviolet lasing of hexagonal boron nitride single crystal. *Nat. Mater.* **3** 404 (2004).

[5] Dean C. R. *et al.* Boron nitride substrates for high-quality graphene electronics. *Nat. Nanotech.* **5** 722 (2010).

[6] Britnell L. *et al.* Field-effect tunneling transistor based on vertical graphene heterostructures. *Science* **335** 947 (2012).

[7] Dean C. *et al.* Hofstadter's butterfly and the fractal quantum Hall effect in moire superlattices. *Nature* **497** 598 (2013).

[8] Kim K. K. *et al.* Synthesis and characterization of hexagonal boron nitride film as a dielectric layer for graphene devices. *ACS Nano* **6** 8583 (2012).

[9] Lee K. H. *et al.* Large-scale synthesis of high-quality hexagonal boron nitride nanosheets for large-area graphene electronics. *Nano Lett.* **12** 714 (2012).

[10] Levendorf M. P. *et al.* Graphene and boron nitride lateral heterostructures for atomically thin circuitry. *Nature* **488** 627 (2012).

[11] Cassabois G., Valvin P. and Gil B. Hexagonal boron nitride is an indirect bandgap semiconductor. *Nat. Photonics* **10** 262 (2016).

[12] Kubota Y., Watanabe K., Tsuda O. and Taniguchi T. Deep ultraviolet light-emitting hexagonal boron nitride synthesized at atmospheric pressure. *Science* **317** 932 (2007).

[13] Watanabe K., Taniguchi T., Niiyama T., Miya K. and Taniguchi M. Far-ultraviolet plane-emission handheld device based on hexagonal boron nitride. *Nat. Photonics* **3** 591 (2009).

[14] Kim K. K. *et al.* Synthesis of monolayer hexagonal boron nitride on Cu foil using chemical vapor deposition. *Nano Lett.* **12** 161 (2011).

[15] Tay R. Y. *et al.* Growth of large single-crystalline two-dimensional boron nitride hexagons on electropolished copper. *Nano Lett.* **14** 839 (2014).

[16] Tay R. Y. *et al.* Synthesis of aligned symmetrical multifaceted monolayer hexagonal boron nitride single crystals on resolidified copper. *Nanoscale* **8** 2434 (2016).

[17] Kidambi P. R. *et al.* In situ observations during chemical vapor deposition of hexagonal boron nitride on polycrystalline copper. *Chem. Mater.* **26** 6380 (2014).

[18] Ismach A. *et al.* Toward the controlled synthesis of hexagonal boron nitride films. *ACS Nano* **6** 6378 (2012).

[19] Shi Y. *et al.* Synthesis of few-layer hexagonal boron nitride thin film by chemical vapor deposition. *Nano Lett.* **10** 4134 (2010).

[20] Caneva S. *et al.* Controlling catalyst bulk reservoir effects for monolayer hexagonal boron nitride CVD. *Nano Lett.* **16** 1250 (2016).

[21] Caneva S. *et al.* Nucleation control for large, single crystalline domains of monolayer hexagonal boron nitride via Si-doped Fe catalysts. *Nano Lett.* **15** 1867 (2015).

[22] Kim S. M. *et al.* Synthesis of large-area multilayer hexagonal boron nitride for high material performance. *Nat. Commun.* **6** 8662 (2015).

[23] Sutter P., Lahiri J., Zahl P., Wang B. and Sutter E. Scalable synthesis of uniform few-layer hexagonal boron nitride dielectric films. *Nano Lett.* **13** 276 (2012).

[24] Gao Y. *et al.* Repeated and controlled growth of monolayer, bilayer and few-layer hexagonal boron nitride on Pt foils. *ACS Nano* **7** 5199 (2013).

[25] Kim G. *et al.* Growth of high-crystalline, single-layer hexagonal boron nitride on recyclable platinum foil. *Nano Lett.* **13** 1834 (2013).

[26] Hao Y. *et al.* The role of surface oxygen in the growth of large single-crystal graphene on copper. *Science* **342** 720 (2013).

[27] Weatherup R. S. *et al.* In situ characterization of alloy catalysts for low-temperature graphene growth. *Nano Lett.* **11** 4154 (2011).

[28] Song X. *et al.* Seed-assisted growth of single-crystalline patterned graphene domains on hexagonal boron nitride by chemical vapor deposition. *Nano Lett.* **16** 6109 (2016).

[29] Ismach A. *et al.* Carbon-assisted chemical vapor deposition of hexagonal boron nitride. *2D Mater.* **4** 025117 (2017).

[30] Zheng R. *et al.* Low-temperature growth of graphene on iron substrate by molecular

beam epitaxy. *Thin Solid Films* **627** 39 (2017).

[31] Xu Z. *et al.* Direct growth of hexagonal boron nitride/graphene heterostructures on cobalt foil substrates by plasma-assisted molecular beam epitaxy. *Appl. Phys. Lett.* **109** 043110 (2016).

[32] Xu Z. *et al.* Large-area growth of multi-layer hexagonal boron nitride on polished cobalt foils by plasma-assisted molecular beam epitaxy. *Sci. Rep.* **7** 43100 (2017).

[33] Xu Z., Zheng R., Khanaki A., Zuo Z. and Liu J. Direct growth of graphene on in situ epitaxial hexagonal boron nitride flakes by plasma-assisted molecular beam epitaxy. *Appl. Phys. Lett.* **107** 213103 (2015).

[34] Zuo Z. *et al.* In-situ epitaxial growth of graphene/h-BN van der Waals heterostructures by molecular beam epitaxy. *Sci. Rep.* **5** 14760 (2015).

[35] Li X. *et al.* Transfer of large-area graphene films for high-performance transparent conductive electrodes. *Nano Lett.* **9** 4359 (2009).

[36] Jensen F., Besenbacher F., Lægsgaard E. and Stensgaard I. Surface reconstruction of Cu (110) induced by oxygen chemisorption. *Phys. Rev. B* **41** 10233 (1990).

[37] Li X. *et al.* Large-area synthesis of high-quality and uniform graphene films on copper foils. *Science* **324** 1312 (2009).

[38] Hasegawa Y. and Avouris P. Direct observation of standing wave formation at surface steps using scanning tunneling spectroscopy. *Phys. Rev. Lett.* **71** 1071 (1993).

[39] Kula P., Pietrasik R. and Dybowski K. Vacuum carburizing—process optimization. *J. Mater. Process. Technol.* **164** 876 (2005).

[40] Xie J. and Spallas J. P. Different contrast mechanisms in SEM imaging of graphene. *A. Technologies, ed* (2012).

[41] Gorbachev R. V. *et al.* Hunting for monolayer boron nitride: optical and Raman signatures. *Small* **7** 465 (2011).

[42] Koh A. T., Foong Y. M. and Chua D. H. Comparison of the mechanism of low defect few-layer graphene fabricated on different metals by pulsed laser deposition. *Diamond Relat. Mater.* **25** 98 (2012).

[43] Stenger I. *et al.* Low frequency Raman spectroscopy of few-atomic-layer thick h-BN crystals. *2D Mater.* **4** 031003 (2017).

[44] Greenler R. G. and Slager T. Method for obtaining the Raman spectrum of a thin film on a metal surface. *Spectrochim. Acta, Part A* **29** 193 (1973).

[45] Pease R. S. An X-ray study of boron nitride. *Acta Crystallogr.* **5** 356 (1952).

[46] Johnson W. A. Reaction kinetics in process of nucleation and growth. *Trans. AIME* **135** 416 (1939).

[47] Kim H. *et al.* Activation energy paths for graphene nucleation and growth on Cu. *ACS Nano* **6** 3614 (2012).

[48] Ye F. and Lu K. Crystallization kinetics of Al–La–Ni amorphous alloy. *J. Non-Cryst. Solids* **262** 228 (2000).

[49] Lee G.-H. *et al.* Electron tunneling through atomically flat and ultrathin hexagonal boron nitride. *Appl. Phys. Lett.* **99** 243114 (2011).

[50] Moudler J. F., StickleW. F., Sobol P. E. and Bomben K. D. Handbook of X-ray photoelectron spectroscopy. *Perkin-Elmer, Eden Prairie, MN* **52** (1992).

[51] Khanaki A. *et al.* Self-assembled cubic boron nitride nanodots. *Sci. Rep.* **7** 4087 (2017).

[52] Trehan R., Lifshitz Y. and Rabalais J. Auger and x-ray electron spectroscopy studies of h-BN, c-BN, and N^{+2} ion irradiation of boron and boron nitride. *J. Vac. Sci. Technol. A* **8** 4026 (1990).

[53] Widmayer P., Boyen H.-G., Ziemann P., Reinke P. and Oelhafen P. Electron spectroscopy on boron nitride thin films: comparison of near-surface to bulk electronic properties. *Phys. Rev. B* **59** 5233 (1999).

[54] Bonzel H. and Krebs H. On the chemical nature of the carbonaceous deposits on iron after CO hydrogenation. *Surf. Sci.* **91** 499 (1980).

[55] Panzner G. and Diekmann W. The bonding state of carbon segregated to α-iron surfaces and on iron carbide surfaces studied by electron spectroscopy. *Surf. Sci.* **160** 253 (1985).

[56] Zhang C. *et al.* Direct growth of large-area graphene and boron nitride heterostructures by a co-segregation method. *Nat. Commun.* **6** 6519 (2015).

[57] Ishida K. and Nishizawa T. The C-Co (carbon-cobalt) system. *J. Phase Equilib.* **12** 417 (1991).

[58] Zheng M. *et al.* Metal-catalyzed crystallization of amorphous carbon to graphene. *Appl. Phys. Lett.* **96** 063110 (2010).

[59] Wesner D., Linden G. and Bonzel, H. Alkali promotion on cobalt: surface analysis of the effects of potassium on carbon monoxide adsorption and Fischer-Tropsch reaction.

Appl. Surf. Sci. **26** 335 (1986).

[60] Liu S., van Duin A. C., van Duin D. M., Liu B. and Edgar J. H. Atomistic insights into nucleation and formation of hexagonal boron nitride on nickel from first-principles-based reactive molecular dynamics simulations. *ACS Nano* **11** 3585 (2017).

Chapter 4: Self-assembled growth of cubic boron nitride nanodots

4.1. Introduction

Boron nitride (BN) is a III-V compound and isoelectronic to the similarly structured carbon lattice, i.e., can possess sp^2- and sp^3-bonded phases. This feature leads to a variety of crystalline BN forms including hexagonal (h-BN), rhombohedral (r-BN), turbostratic (t-BN), cubic (c-BN) and wurtzite (w-BN). Among all these crystalline forms, bulk c-BN is most thermodynamically stable, which has excellent physical and chemical properties such as super high hardness (>70 GPa), wide direct band-gap energy (Eg ≈ 6.4 eV), doping ability for both p- and n-type conductivity, very high isotropic thermal conductivity (13 $Wcm^{-1}K^{-1}$) along with very low linear thermal expansion (1.2×10^{-6} $°C^{-1}$), low dielectric constant (7.1), high breakdown field (~0.7 Vnm^{-1}), high-oxidation resistant (>1300 °C), and high structural and chemical stability. These intriguing properties have attracted many researchers to work on synthesis, characterization, and implementation of c-BN bulk and thin film materials for a broad range of mechanical, thermal and optoelectronic applications [1-10].

Low-dimensional c-BN nanodots (NDs) have their unique applications in addition to those enabled from their bulk counterparts. More specifically, the nanometric size c-BN nanodots with a large surface area can enhance performance of many devices and systems. For example, c-BN NDs can be integrated with lithium metal oxide/phosphide ($LiMO_2$/$LiMPO_4$) cathode materials used in Li-ion batteries and act as a fast heat dissipater

with low thermal expansion to improve their safety features, or as an agent to increase their thermal and chemical stabilities [11]. Also, c-BN NDs can be used as a catalyst support for all applications in which the process requires relatively high temperatures [12]. Furthermore, they are considered as a well-suited candidate for variety of biological applications such as high-contrast bioimaging probe, cell tracking, and gene technology owing to their fast and uniform agglomeration around the targeting material, strong fluorescence properties, and excellent biocompatibility [13]. Nanometric c-BN dots can be also used as a very fine polishing agent because of their size and high hardness [14]. Surface-plasmon-mediated deep ultraviolet ND light emitting diodes, sensors, and electrically insulating/thermally conductive filters in high-power/high-frequency electronics operating in harsh environments are among other examples that may also benefit from c-BN NDs.

Industrial C-BN materials are produced in large quantities as powders with sizes ranging from submicron to millimeters by a high-pressure high-temperature (HPHT) method. However, because of very high growth temperature, in turn, fast growth rate, the size of c-BN particles could not easily reach below submicron [15]. So far, there are very few experimental works for preparation of nanometric c-BN particles or NDs. Among these efforts, phase transformation, laser ablation, and solvothermal reaction have been mostly attempted. Phase transformation of graphite-like (hexagonal) or amorphous BN precursors usually requires extremely high pressure of several tens GPa and high temperature of 1300~1700 °C [16,17]. Laser ablation technique also uses hexagonal BN precursors, which requires a high-power laser to provide locally high pressure/temperature for c-BN NDs

growth [18]. Chemical routes can also generate a large amount of c-BN materials, however, controlling the size, morphology, phase and purity of as-grown NDs is difficult thanks to low reaction temperature [19,20]. Aside from having to use extreme growth conditions, such synthesis approaches often lead to the final products with either a mixture of different BN phases, e.g. h-BN/c-BN, or containing process-related impurities/contaminants [16-20].

In contrast, self-assembled growth of NDs has been identified as an important nanofabrication process in which the building blocks spontaneously organize into random and/or ordered distributions by thermodynamic and other constraints [21] However, in order to successfully exploit NDs self-assembly in technological applications and to ensure effective scale-up, a high level of control using ultra high vacuum chemical vapor deposition (CVD) or molecular beam epitaxy (MBE) is desirable. As a versatile tool, MBE has natural advantages in high-quality materials growth including thin films and self-assembled NDs because of its ultra-high vacuum environment and instant introduction and control of multiple sources [22-28]. Therefore, the direct growth of c-BN NDs by MBE offers reduced complexity of fabrication procedure as well as a great degree of quality, purity, and reproducibility. Here we report MBE growth and characterization of self-assembled c-BN NDs on cobalt (Co) and nickel (Ni) metal substrates. A simplified numerical model is also introduced to simulate the formation energy behaviour of c-BN NDs on metal substrates.

4.2. Experimental details

Substrate preparation. Commercial cobalt (Co) foil (Alfa Aesar, 0.1 mm thick, 99.95% purity) and nickel (Ni) foil (Alfa Aesar, 0.025 mm thick, 99.5% purity) were used as substrates. The measured roughness for as-received Co and Ni foils are 187 and 140 nm, respectively (Figure 4.1). The foils were cut into 1 cm×1 cm pieces and etched by diluted HCl solution (5%) for 1 minute to remove the native oxides. Acetone, isopropyl alcohol (IPA), and deionized water (DI) were used to clean the substrates. After blown dry using a nitrogen gun, these substrates were immediately loaded onto substrate holders and transferred to the growth chamber. A Knudsen effusion cell filled with B_2O_3 powder (Alfa Aesar, 99.999%) was used as the boron source. An electron cyclotron resonance (ECR) system was used to form nitrogen gas plasma (Airgas, 99.9999%) as the nitrogen source. The nitrogen source was tuned by either nitrogen gas flow meter or ECR magnetron current.

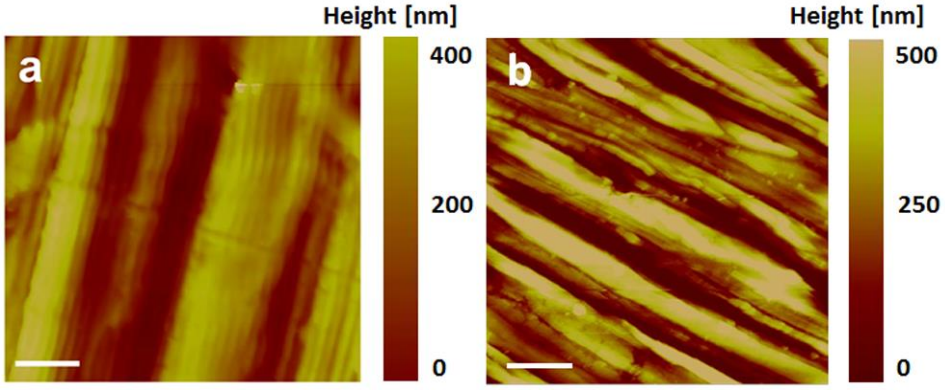

Figure 4.1. AFM images of the substrates. (a) nickel foil and (b) cobalt foil. The root mean square roughness is 140 and 187 nm for Ni and Co foil substrates, respectively. The scale bars are 10 μm.

C-BN NDs growth. For a typical growth, the substrate was firstly annealed at 900 ºC under a hydrogen flow of 10 sccm for a duration of 15 minutes. At the end of substrate surface treatment, the hydrogen gas flow rate was reduced to 6 sccm and c-BN NDs growth was started. Boron cell temperature was ramped to 1100 ºC right before the growth. Nitrogen flow rate was 10 sccm and the ECR current was set at 60 mA. The growth time varied between 10 seconds and 45 minutes and the growth temperature was 900 ºC for all samples. At the end of growth, the substrate temperature was cooled towards ambient temperature. The substrate heating/cooling rate was ~10 ºC/min.

C-BN NDs characterization. Raman characterizations were performed using a HORIBA LabRam system equipped with a 60-mW 532-nm green laser. Scanning electron microscopy (SEM) images were acquired using a XL30-FEG system. Atomic force microscopy (AFM) images were obtained using a Veeco AFM D3100 system. Size distribution and density of c-BN NDs samples grown on Co foil were obtained using ImageJ software. X-ray photoelectron spectroscopy (XPS) was carried out using a Kratos AXIS ULTRA XPS system equipped with an Al Kα monochromatic X-ray source and a 165-mm mean radius electron energy hemispherical analyzer. X-ray diffraction (XRD) (Philips, PW1730) was performed at θ-2θ configuration and using Cu Kα radiation (λ=1.5405 Å, 40 kV, 40 mA). Transmission electron microscopy (TEM) images were acquired using a FEI/Philips CM-30 TEM. Cross-sectional TEM samples were prepared using the focused ion beam technique. C-BN NDs sample was originally covered by a carbon layer of 26 nm, followed by an Ir layer of about 6 nm, and further protected by electron-beam and ion-beam deposited Pt layers of 41 nm and 1.5 μm, respectively.

4.3. Results and discussion

4.3.1. Self-assembled growth of c-BN NDs on Co substrate. Figure 4.2(a) shows an SEM image of a c-BN NDs sample, which was grown on Co foil substrate at 900 °C for a duration of 10 minutes, showing a relatively uniform distribution of NDs over a large area of the sample.

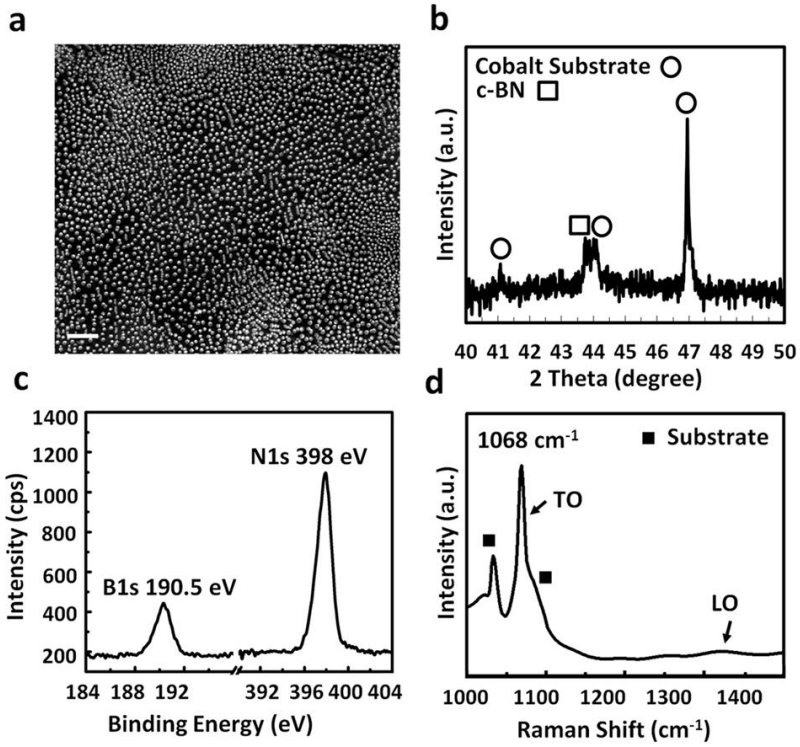

Figure 4.2. Characterization of self-assembled c-BN NDs grown on Co foil substrate by plasma-assisted MBE. The sample was grown at 900 °C for 10 minutes. (a) SEM image of the sample showing a relatively uniform distribution of NDs over a large area. The average NDs lateral size and density are estimated to be ~87 nm and ~4.08×10^{9} cm^{-2}, respectively. The scale bar is 1 μm. (b) Short-range X-ray diffraction pattern of c-BN NDs on Co foil substrate showing a dominant peak at 43.89° corresponding to (111) crystal plane diffraction of c-BN NDs with the fcc structure. (c) B1s and N1s XPS signals of NDs. (d) Raman spectrum of c-BN NDs showing an evident TO phonon peak located at 1068 cm^{-1}.

Using ImageJ software, the density of NDs was estimated to be ~4.08×10^{9} cm^{-2} (Figure 4.3). The lateral size of NDs was also estimated to be 80~90 nm.

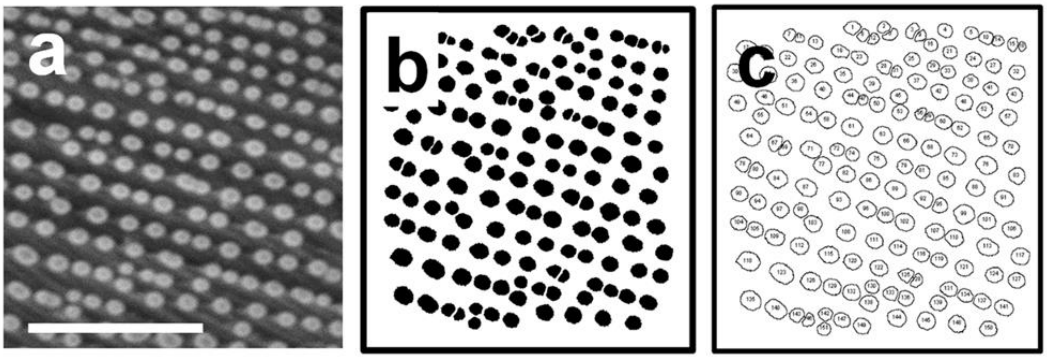

Figure 4.3. An example of size distribution estimation using ImageJ software. First, an area of 4 μm^2 from an SEM image was selected for each sample. (a) shows the selected area for the sample grown on Co foil at a growth temperature of 900 ºC for 5 minutes. (b) By applying a black/white contrast threshold, NDs were defined as circular features, which are outlined with black circles and accordingly numbered, as shown in (c). Subsequently, the software calculated the area for each ND and the total number of NDs. Finally, their diameter (lateral size) as well as their density were estimated. The scale bar in (a) is 1 μm.

Figure 4.2(b) shows X-ray diffraction pattern of the c-BN NDs sample. The dominant peak at 43.89° was assigned to (111) crystal plane diffraction of c-BN NDs with the fcc structure according to JCPDS#025-1033. Short-range (2θ: 40~50°) survey was chosen for Figure 4.2(b) to resolve the peak deconvolution for c-BN (111) and Co (002) occurred near 44° diffraction angle. Full-range XRD pattern (2θ: 20~90°) of the sample is also shown in Figure 4.4. According to the full-range scan, no other diffraction of BN related materials can be observed, suggesting that NDs are dominantly cubic in structure [29]. Due to the much lower peak intensity compared to those from the substrate, the second and third order diffraction peaks of c-BN NDs are not detected in the spectrum. The calculated unit cell

parameter from the XRD result of c-BN NDs is 3.57 Å. A slight change from its bulk number of 3.61 Å suggests that some strain still exists after the formation of the dots [30]. It is worth mentioning that the lattice of c-BN NDs may be distorted unevenly in the in-plane and cross-plane directions since the θ/2θ peak only gives information about (111) plane distance. Furthermore, as the self-assembly formation of dots represents a process of strain relaxation due to lattice mismatch between the dots and substrate, the degree of strain relaxation may also vary from dots with different sizes and shapes, and from near the substrate-NDs interface to the upper part within the same dot, as shown in TEM imaging later.

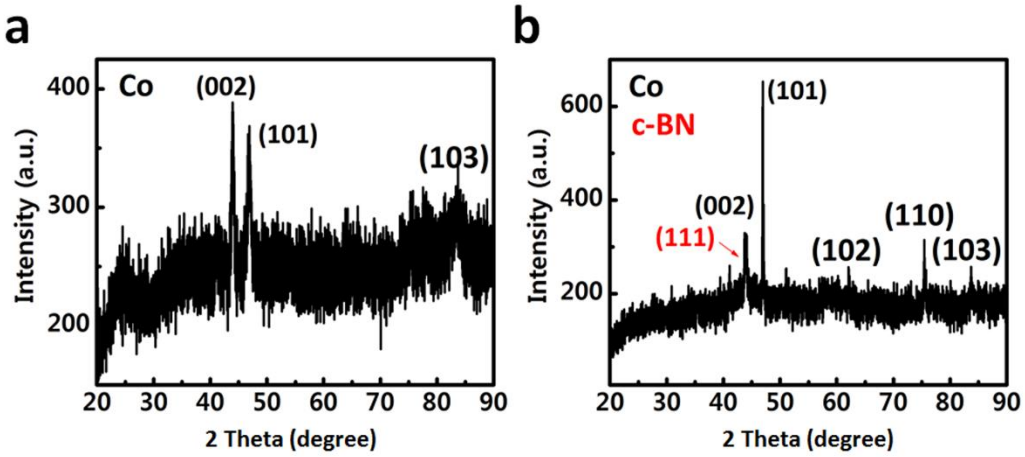

Figure 4.4. Full range XRD patterns. XRD spectra of (a) as-received Co substrate, and (b) the c-BN NDs grown on Co substrate at 900 °C for a duration of 10 minutes**.** Except a peak at about 44° (see Figure 4.2(b) for a better visualization), no other diffraction of BN related materials can be observed in the entire pattern (2θ: 20-90°), suggesting that NDs possess dominantly cubic structure. All other peaks were assigned to diffractions from polycrystalline Co substrate with the hexagonal structure according to JCPDS# 01-071-4239.

Figure 4.2(c) shows XPS spectrum of B1s and N1s signals. B1s and N1s exhibit an energy position at 190.5 eV and 398.0 eV, respectively, which are typical characteristics of c-BN material [31]. By using sensitivity factors from the instrument manufacturer and calculating atomic % of each atom, the B/N ratio is 1.01, suggesting an almost equal composition of boron and nitrogen elements. Figure 4.2(d) shows a Raman spectrum of the c-BN NDs sample. A peak at 1068 cm^{-1} is evident, which shows a large shift of 12 cm^{-1} towards a higher wavenumber compared to the characteristic transverse optical (TO) phonon mode of c-BN bulk material (1056 cm^{-1}) [32]. This could be due to the strain effect induced by lattice mismatch between the Co substrate and c-BN NDs and/or internal NDs crystal defects [32]. The intensity of the longitudinal optical (LO) phonon mode at about 1306 cm^{-1} is much weaker than that of the TO phonon mode, which could be due to the size effects from c-BN NDs or internal lattice defects [33]. Also, according to the Raman selection rule, the observation of TO and LO phonon modes indicates that the c-BN NDs growth has dominantly occurred along <111> direction, which is consistent with our XRD results (Figure 4. 2(b)). No h-BN phonon modes (e.g., E_{2g} at about 1366 cm^{-1}) are observed as well. The full width at half maximum (FWHM) of the TO phonon peak is 10 cm^{-1}, which is twice as large as that of a single crystal c-BN material having a high quality and a size of 1~2 mm obtained by a high-pressure method [35]. The difference could be explained by the small and non-uniform size effects on the FWHM of the phonons in the NDs [36]. A peak at 1034 cm^{-1} and its shoulder at around 1086 cm^{-1} in the Raman spectrum are mainly caused by the post-growth Co surface oxidation and subsequent formation of CoO, $Co(OH)_3$, CoO(OH), and Co_3O_4 (Figure 4.5) [37-39]. Other materials such as boron oxide

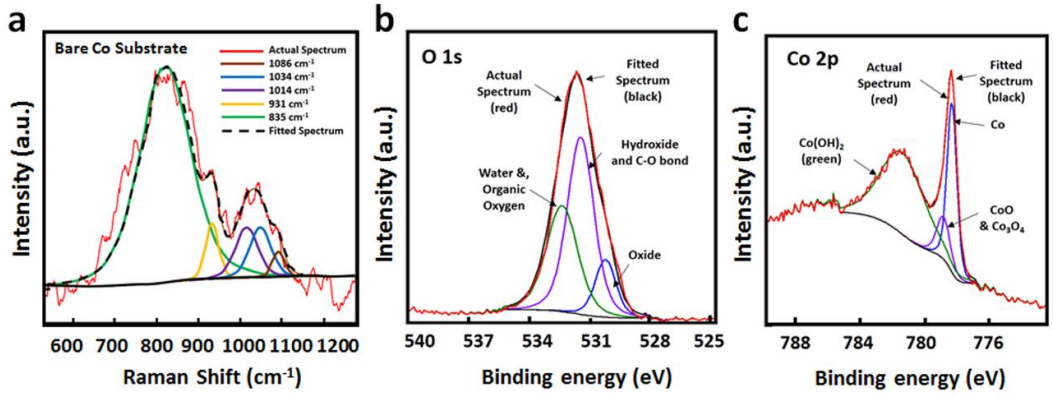

Figure 4.5. Raman and XPS analyses. (a) Raman spectrum of the bare Co substrate fitted into multiple peaks. XPS signals of (b) O1s and (c) Co2p for c-BN NDs sample grown on Co substrate at 900 °C for 10 minutes.

(B_2O_3) [40], boric acid (H_3BO_3) [41], boron carbide (B_4C) [42], carbon nitride (CN) [43], and cobalt boride (CoB) [44] do not exist in our c-BN NDs based on their Raman, XRD, and XPS characteristics, suggesting the formation of pure c-BN phase in this synthesis method.

Figure 4.6(a-d) show SEM images of c-BN NDs samples grown at different growth time of 10 seconds, 30 seconds, 5 minutes, and 45 minutes, respectively. All the samples were grown at 900 °C. Therefore, together with the 10-minute sample discussed earlier, we have total five samples to study the growth time dependence. According to Figure 4.2(a) and (b), even at a short growth time of 10 or 30 seconds, high-density NDs have been formed on the Co foil surface, suggesting that the growth rate should have been fast. The fast growth rate of NDs within a short period of time can be due to the catalytic effect of Co substrate, which reduces the NDs growth formation energy [45-47]. In addition, the rough surface of the Co substrate (Rq ~ 187 nm) provides a great number of preferential

nucleation sites for NDs growth [48]. As a result, NDs notably increase in size as the growth time increases within this short growth time (Figure 4.6(a) and (b)). However, as the growth time further increases (up to 45 minutes), the NDs growth rate reduces and the NDs become more uniform in size and shape (Figure 4.6(c) and (d)). This is reasonable since it is less thermodynamically favorable for incoming boron and nitrogen atoms to grow upon previously grown c-BN NDs compared to that of fresh Co foil surface thanks to different formation energy on these surfaces [49,50]. In addition, it has been theoretically shown that the surface free energy barrier is the largest at the edges of the NDs due to NDs surface strain, and decays as the adatoms move away from them, further suggesting that the adatoms tend to form new NDs instead of accumulating with previously grown ones [50]. As the growth time lapses, the substrate surface is eventually covered with dense NDs and simultaneously run out of preferential nucleation sites. Further introduction of sources onto the substrate would lead to the accumulation of adatoms on existing NDs. During this period, two competing processes may co-exist for those relatively small NDs: higher-strained, smaller NDs grow faster than less-strained larger ones in order to reduce their larger surface strain and total free energy [50,51]. On the other hand, boron and nitrogen atoms may leave very small or irregular-shaped NDs to settle into larger NDs [52,53]. The competing processes eventually bring about more uniformity in size with time. It should be also noted that apparent chain-like alignment of NDs is observed in the SEM images. This is related to the substrate roughness effect, which is discussed later [54].

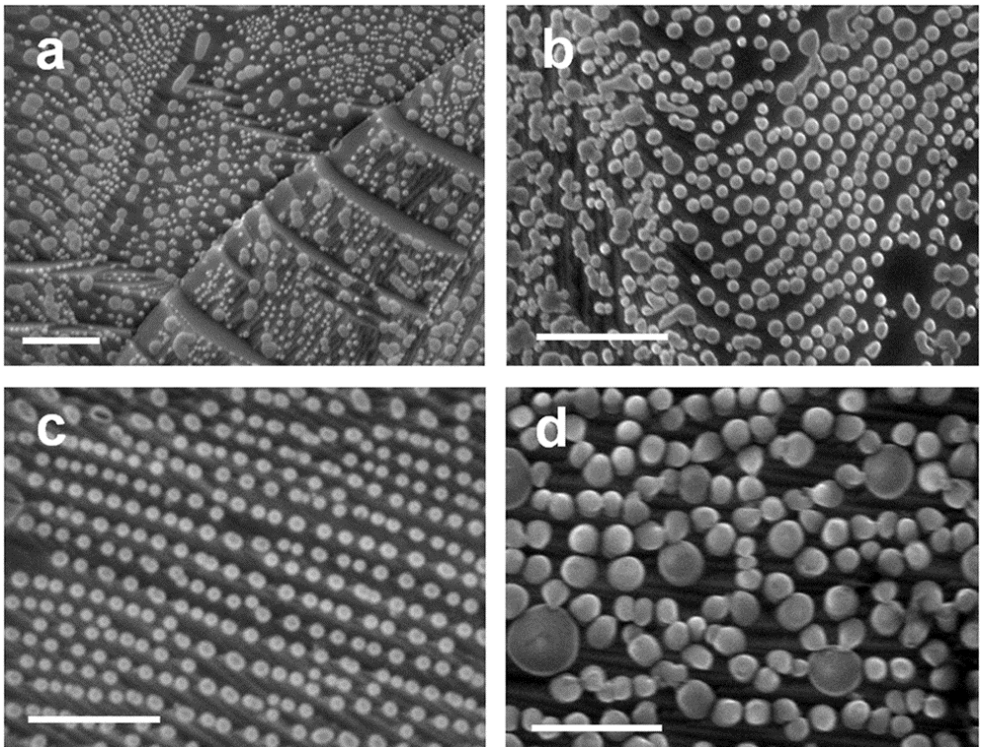

Figure 4.6. Morphology evolution of the c-BN NDs as a function of growth time. SEM images of samples grown at (a) 10 seconds, (b) 30 seconds, (c) 5 minutes, and (d) 45 minutes. All the samples were grown at the same growth temperature of 900 °C and all the scale bars are 1 μm.

Figure 4.7(a) shows histogram plot of NDs lateral size distributions as a function of growth time using ImageJ software (Figure 4.2). The number of NDs and their lateral size were approximated for an area of 4 μm^2. It is worth mentioning that the effort to extract vertical height information of these dots by AFM was halted as a result of quite rough Co foil substrate surface. According to Figure 4.7(a), the distribution of ND sizes narrows from 30~175 nm (mean: 77.6 nm, standard deviation: 38.3 nm) to 30~155 nm (mean: 93 nm, standard deviation: 23.8 nm), 50~142 nm (mean: 102.5 nm, standard deviation: 16 nm), 62~190 nm (mean: 112.7 nm, standard deviation: 19.2 nm), and finally

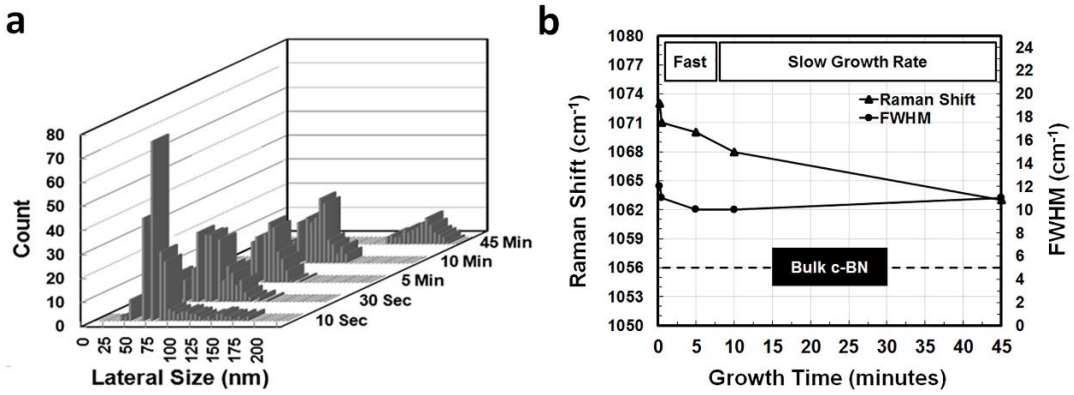

Figure 4.7. Growth time-dependent features analysis. (a) Graphical representation of c-BN NDs on Co lateral size distributions by histogram; (b) Raman shift and FWHM of TO phonon peak of c-BN NDs versus growth time. Raman shift evolves from 1073 to 1063 cm^{-1}. The size dependence of FWHM of the TO phonon peak is weak in a range of 10~12 cm^{-1}. The dashed line in (b) shows the position for characteristic TO phonon peak and FWHM of bulk c-BN

140~210 nm (mean: 174.4 nm, standard deviation: 18.6 nm) as the growth time increases from 10 seconds to 30 seconds, 5 minutes, 10 minutes and finally to 45 minutes. Moreover, since the area of survey for each sample is constant (4 μm^2), the number of NDs becomes less as the growth time progresses, suggesting that NDs become larger and their density reduces.

Figure 4.8 shows Raman spectra for all five samples and Figure 4.7(b) shows Raman shift and FWHM of TO phonon peak of ND sample as a function of growth time. Raman characteristic peak blue-shifts from 1073 to 1063 cm^{-1} as the NDs enlarge with the growth time. Interestingly, the rate change in Raman peak wavenumber is also in accordance with the observed trend for changes in the growth rate of NDs in the SEM images (Figure 4.2(a) and Figure 4.6). However, the FWHM of the TO phonon peak in a

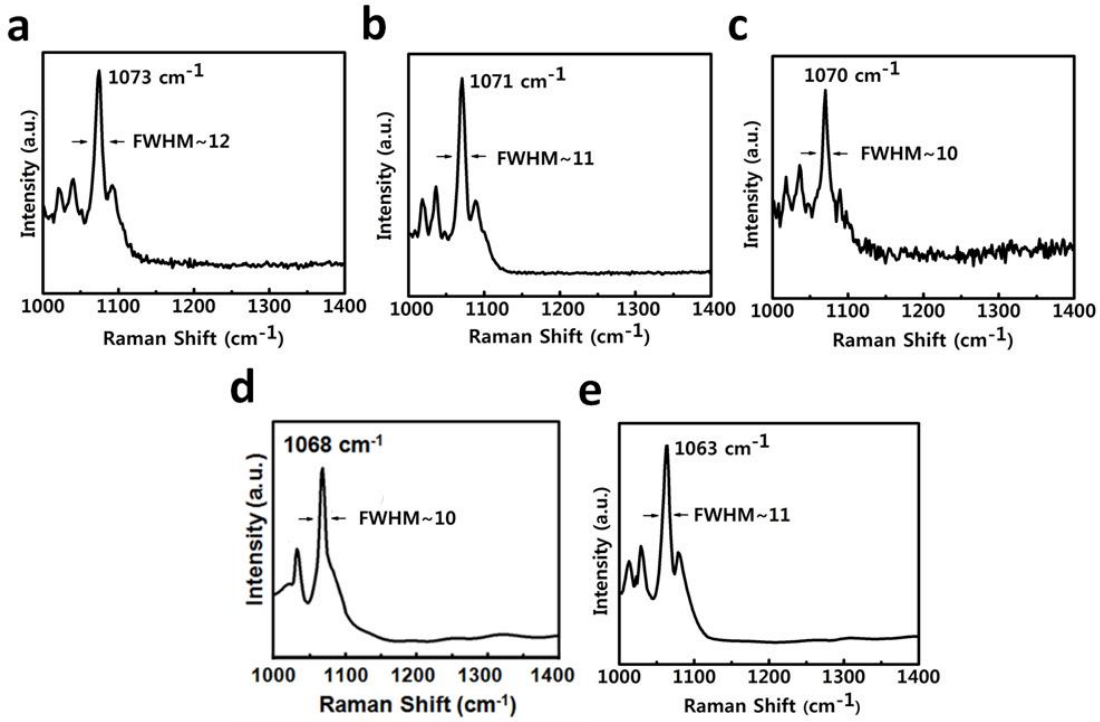

Figure 4.8. Raman spectra of c-BN NDs on Co substrate. Samples grown at 900 °C for (a) 10 seconds, (b) 30 seconds, (c) 5 minutes, (d) 10 minutes, and (e) 45 minutes

range of 10~12 cm^{-1} does not have a clear dependence of the size of the dots. It should be noted that the intensity of LO phonon modes decreases as the decrease of the growth time, which may be due to relaxation of Raman selection rules for smaller c-BN NDs [33,34].

4.3.2. Self-assembled growth of c-BN NDs on Ni substrate. In order to study different substrate effect on the formation of c-BN NDs, Ni foil was also used. Because of its similarity with Co in terms of catalytic effect [55] and lattice mismatch with c-BN, it is expected that c-BN NDs can also be formed on Ni substrate. Figure 4.9(a) shows an SEM image of a c-BN NDs sample grown at 900 ºC for 10 minutes. X-ray diffraction, XPS, and

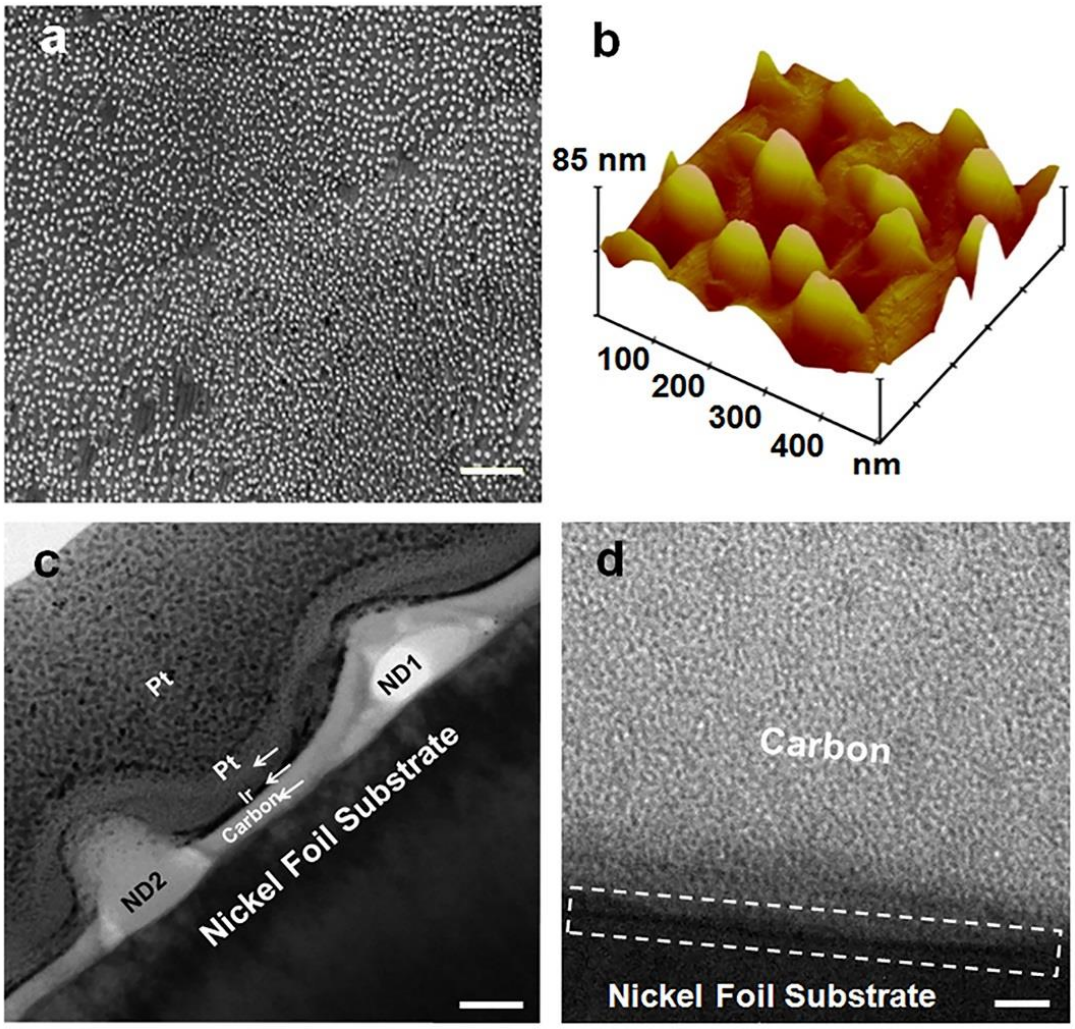

Figure 4.9. Characterization of c-BN NDs on Ni foil substrate. The sample was grown at 900 °C for 10 minutes. (a) SEM image of the sample. The NDs are uniformly distributed over a large area. The density of NDs is estimated to be ~2.3×10^{9} cm^{-2}. The scale bar is 1 μm. (b) AFM image of the sample, c-BN NDs have average lateral and vertical sizes of ~ 95 and ~ 45 nm, respectively. (c) Cross-sectional bright field TEM image of the sample. Two c-BN NDs are resolved in the image. (d) Higher resolution bright field TEM image of the sample. The dashed-line rectangle shows the interface between the carbon coating layer and Ni foil substrate between the two NDs. No c-BN wetting layer underneath or near the NDs area can be observed, indicating VW growth mode.

Raman spectroscopy characterization of the sample indicates that these NDs are c-BN (Figure 4.10).

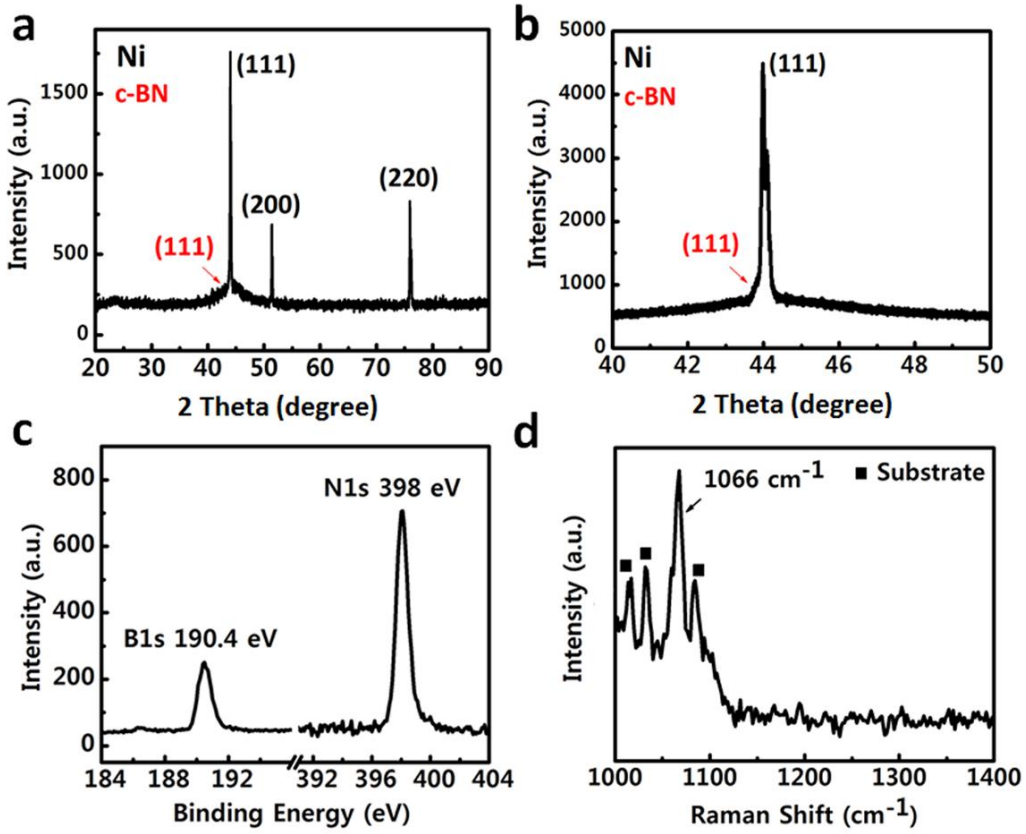

Figure 4.10. Characterizations of self-assembled c-BN NDs on Ni foil substrate by plasma-assisted MBE. The sample was grown at 900 °C for 10 minutes. (a) Long range and (b) short range X-ray diffraction pattern of c-BN NDs on Ni substrate showing a shoulder at 43.8° near the (111) crystal plane diffraction of Ni substrate. Other diffractions were assigned to the polycrystalline Ni substrate with a fcc structure according to JCPDS# 00-004-0850. (c) B1s and N1s XPS signals of NDs with the B/N ratio of ~1.02. (d) Raman spectrum of c-BN NDs showing an evident peak located at 1066 cm^{-1} with a full width half maximum (FWHM) of ~11 cm^{-1}.

As seen from the SEM image, a relatively uniform distribution of c-BN NDs is achieved over a large area of the Ni substrate. The density of NDs is estimated to be around ~2.3×10^{9} cm^{-2}, which is lower than that on Co foil sample under the same growth condition (Figure 4.2(a)). This might be due to the smoother surface of Ni foil, in turn, less preferential nucleation sites (Figure 4.1). Using AFM characterizations (Figure 4.9(b)), the

average lateral and vertical sizes of c-BN NDs were estimated to be ~95 and ~40 nm, respectively. Figure 4.9(c) shows a bright field cross-sectional TEM image of the sample. Two c-BN NDs are evident within the imaging area. Figure 4.9(d) shows a higher resolution bright field TEM image of the sample area between the two NDs. A dashed-line rectangle in Figure 4.9(d) is used to guide the eyes on the interface between the carbon coating layer and Ni foil substrate. No c-BN epilayer/wetting layer underneath or between the NDs can be observed, indicating that the c-BN ND growth undergoes Volmer-Weber (VW) growth mode [50].

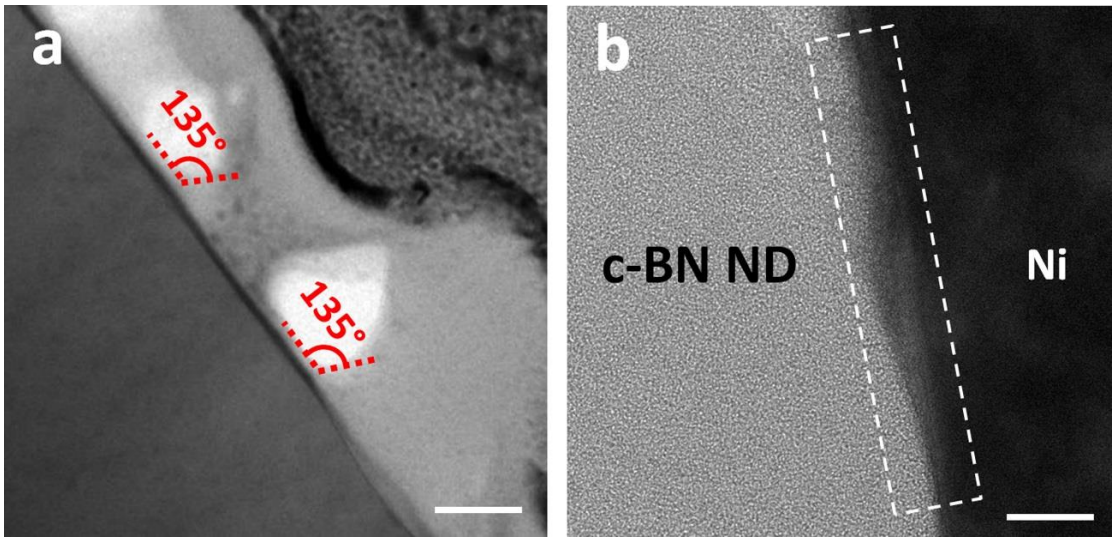

Figure 4.11. High resolution TEM studies of C-BN ND on Ni substrate. (a) Contact angle measurement of c-BN ND on Ni. According to the cross-sectional bright field TEM image in (a) the contact angle of ~135° was measured for another two NDs with approximately a similar lateral size. (b) The interface structure between the c-BN ND and Ni substrate shows a darker contrast compared to the surrounding area of ND. Both the measured contact angle of above 90° in (a) and different contrasts at the interface region and surroundings in (b) could be indications of strain at the interface between c-BN ND and Ni substrate and subsequent VW growth mode. The scale bars in (a) and (b) are 50 and 5 nm, respectively.

This is reasonable because the lattice mismatch between c-BN and Co or Ni substrates prevents the formation of strained two-dimensional BN wetting layer at the early stage of the growth. Instead, small amount of deposited material is accumulated so as to form NDs directly on the substrate. In addition, insolubility of BN in Ni, Co and related alloys at high temperatures causes the boron and nitrogen atoms to more strongly bond to one another than to the underlying substrate, which encourages VW growth mode, as in the case of the growth of many metals on insulator substrates or vice versa [56-58]. The measured contact angle of 135° (i.e., >90°) for c-BN NDs on Ni substrate can be another indication for the presence of strain at the NDs/substrate interface and subsequent VW growth mechanism (Figure 4.11(a)) [59,60]. Moreover, according to Figure 4.11(b), higher resolution bright field TEM images at the interface proximity between the c-BN ND and Ni substrate (dashed-line rectangle) show a darker contrast compared to the surrounding area of ND, implying different atomic structures, lattice spacing, or orientations at such locations which could be another sign of strain [61,62].

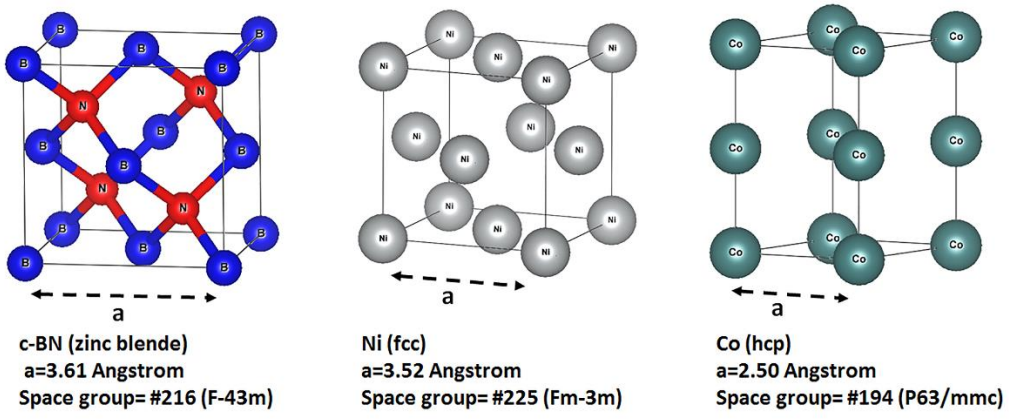

Figure 4.12. Crystal Structure, lattice constant and space group number of c-BN, Ni and Co.

It is worth noting that the amount of lattice mismatch between c-BN structure (zinc blende) and underneath metal substrate (hcp Co or fcc Ni) can vary significantly depending on the ND and substrate surface crystal orientations. Our Co and Ni foil substrates are polycrystalline in nature (Figure 4.4 and Figure 4.10), and even within a single grain, their rough surfaces can expose different facets with different orientations for the growth of c-BN NDs. For example, the lattice mismatch between the c-BN (111) and Co (001) would be ~2% ($\alpha_{c\text{-}BN(111)}$=2.55 Å, $\alpha_{Co(001)}$=2.50 Å), while for other possible crystal orientations such as c-BN (001) on Co (001), it can be as large as ~44.4% ($\alpha_{c\text{-}BN(001)}$=3.61 Å) (Figure 4.12).

4.3.3. C-BN NDs formation energy modeling. To further understand the formation of c-BN ND nucleation on metal substrates, we have carried out numerical modeling of the formation energy. The formation energy can be written as:

$$E_F = E_{surf-ND} + E_{int} - E_{surf-sub} + E_{mismatch} \qquad (1),$$

where E_F is the total formation energy of ND with a unit of (Jm^{-1}), $E_{surf\text{-}ND}$ is the surface energy of ND, E_{int} is the interface energy of the interface between two materials, $E_{surf\text{-}sub}$ is the surface energy of the substrate covered by ND, and $E_{mismatch}$ is the elastic strain energy stored in ND with a unit of (Jm^{-1}). The first three terms are dominating factors in the determination of strainless NDs on a substrate, for example, Si dots on SiO_2 substrate [54]. The last term is included to accommodate the elastic energy strain as a result of lattice mismatch between NDs and underneath metal substrate [63,64]. It should be noted that the

formulation of formation energy in equation (1) does not include contribution from catalytic effect because it would be different for different metal substrates, differs significantly with growth conditions such as growth temperature. Equation (1) can be expressed as the following equation:

$$E_F = L\gamma_{ND}(\sec\theta + \frac{\gamma_{int} - \gamma_{sub}}{\gamma_{ND}}) + \frac{1}{2}SE\varepsilon \qquad (2),$$

Where γ_{ND}, γ_{int}, and γ_{sub} are the surface energy density of ND, interface, and substrate, respectively. L, θ, and S are ND lateral size, contact angle, and the area in two-dimensional (2D) model, respectively. $\gamma = (\frac{\gamma_{int} - \gamma_{sub}}{\gamma_{ND}})$ is defined as a non-dimensional system parameter, which varies between -1 and 1 based on the contact angle (θ) and according to the Young equation [64]. Contact angle also relates to ND size and the nature of the two materials [66-67]. E is Young module of ND, and $\varepsilon = (\frac{\alpha_{ND} - \alpha_{sub}}{\alpha_{sub}})$ is strain caused by lattice mismatch between the ND and metal substrate. α_{ND} and α_{sub} are the lattice constant of ND and unit cell parameter of substrate, respectively. Since it is possible that a nanodot adopts a contact angle upon its nucleation (e.g. $\theta \leq 90°$) and increases it during the growth (e.g. $\theta \geq 90°$), different equations must be used to simulate the formation energy of NDs based on their contact angles and shapes [59,60].

For a contact angle of below 90°, NDs can be simulated as triangles (Figure 4.13), and the total formation energy can be written as:

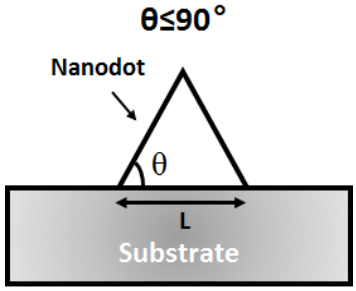

Figure 4.13. Schematic of a ND with a triangular shape and contact angle of below 90°.

$$E_F = \gamma_{ND}(\sec\theta + \frac{\gamma_{\text{int}} - \gamma_{sub}}{\gamma_{ND}})S^{\frac{1}{2}}(\tan\theta)^{-\frac{1}{2}} + \frac{1}{2}SE\varepsilon^2 \qquad (3),$$

$$\theta < 90^o$$

While for a contact angle of above 90°, NDs can be simulated as regular polygons with different number of sides (same length), where the number of the sides are determined by a type of polygon which has the closest inner angle to that of ND contact angle (Figure 4.14 and Table 4.1).

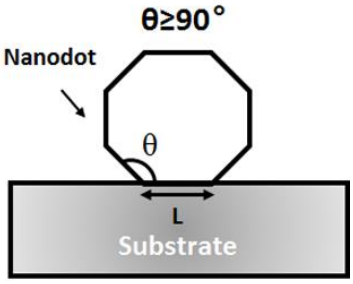

Figure 4.14. Schematic of a ND with a polygon shape and contact angle of above 90°.

Table 4.1. Number of the polygon sides (n) associated with the contact angle of a ND

Number of the Polygon Sides (n)	Inner Angle = Contact Angle (degree)
4	**90**
5	**108**
6	**120**
7	**128.5**
8	**135**
9	**140**
.	**.**

For any regular polygon with *n* sides (same length for all the sides) we can write:

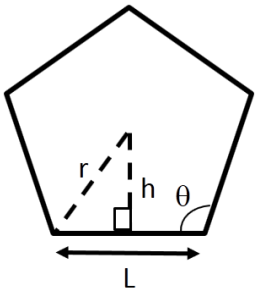

$$r = \frac{L}{2\sin(\frac{180}{n})} \qquad r = \frac{h}{\cos(\frac{180}{n})} \qquad \rightarrow \qquad h = \frac{L\cot(\frac{180}{n})}{2} \qquad n = \frac{360}{180-\theta} \qquad \theta = \frac{(n-2)180}{n}$$

Where *r*, *L*, θ (degree), and *h* are polygon radius, side length, inner angle, and apothem. Therefore, the total area of the polygon can be calculated as the sum of *n* triangles with the same area:

$$S = nS_{triangular} = n\frac{L.h}{2} = \frac{nL^2\cot(\frac{180}{n})}{4} = \frac{nL^2\cot(\frac{\theta}{n-2})}{4}$$

$$n \geq 4$$

$$\theta \geq 90^o$$

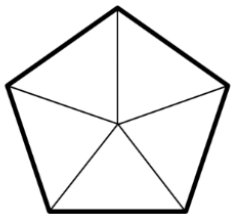

And L can be written as:

$$L = 2(S\tan(\frac{\theta}{n-2}))^{\frac{1}{2}} n^{-\frac{1}{2}}$$
$$n \geq 4$$
$$\theta \geq 90^{o}$$

Therefore, by substituting the new L in Equation (2), the total formation energy (E_f) for a ND with a contact angle of above 90°can be written as:

$$\mathrm{E_F} = 2\gamma_{\mathrm{ND}}(\sec\theta + \frac{\gamma_{\mathrm{int}} - \gamma_{\mathrm{sub}}}{\gamma_{\mathrm{ND}}})\mathrm{S}^{\frac{1}{2}} \tan(\frac{\theta}{\mathrm{n}-2})^{\frac{1}{2}} \mathrm{n}^{-\frac{1}{2}} + \frac{1}{2}\mathrm{SE}\varepsilon^{2}$$
$$\mathrm{n} \geq 4 \qquad (4),$$
$$\theta \geq 90^{\mathrm{o}}$$

where n is the number of the sides for the polygon.

According to Table 4.1, the best polygon that can represent our NDs on Ni with contact angle of 135° is an octagon with n=8 and inner angle of 135°. To run the simulation, we assumed a c-BN ND ($\alpha_{ND(001)}$=3.57 Å) was formed on top of an idealized flat surface of a metal substrate with (111) crystal orientation and a fixed contact angle of θ=135° (Figure 4.11(a)). The best polygon that can represent a ND with θ=135° would be an octagon (n=8) with inner angle of 135°, and hence, Equation (4) can be used to calculate the ND formation energy. Here the values are chosen as a representative case just to show the overall trend

on ND nucleation behavior. The surface energy density and Young module for c-BN NDs are ~40 mJm^{-2} and ~500 GPa, respectively [68,69]. Figure 4.15(a) shows the schematic of NDs formation with different contact angles and Figure 4.15(b) shows the formation energy of c-BN NDs on Ni substrate ($\alpha_{Ni(111)}$=2.48 Å) as a function of γ. The larger the γ is, the higher the formation energy is, and hence, the harder it is to form c-BN ND. It should be also noted that the formation energy is linearly proportional to γ, however, the alterations are not significant. In contrast, when γ is fixed (e.g., γ=-0.7), the formation energy changes dramatically and nonlinearly as the substrate unit cell parameter (α_{sub}) changes within a range of 2~3 Å, as can be seen in Figure 4.15(c).

Similar behavior is observed for various γ and lattice parameters (Figure 4.16). These results suggest that the elastic strain energy ($E_{mismatch}$) plays a major role in determining the total formation energy of strained c-BN NDs on metal substrate via VW

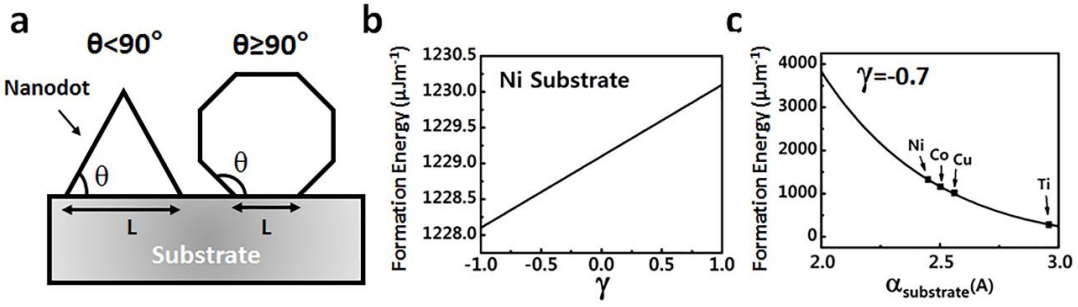

Figure 4.15. Formation energy of c-BN ND on metal substrates. (a) 2D model of a strained self-assembled c-BN ND growth on a flat metal substrate via VW growth mode and different contact angles. (b) Total formation energy of a c-BN ND with the contact angle of 135° grown on flat Ni (111) substrate as a function of γ. (c) Total formation energy of a c-BN ND with the contact angle of 135° and γ fixed at -0.7 as function of substrate unit cell parameter ($\alpha_{substrate}$). Unit cell parameters (along (111) crystal plane) of different transition metal substrates have been tagged in panel c.

growth mode. According to our calculation, this behavior is mainly due to the lattice mismatch between the c-BN NDs and underneath metal substrate, and the large value of Young module for c-BN material (~500 GPa). Although the growth of c-BN NDs has been demonstrated on Co and Ni substrates here, based on our calculations (Figure 4.15(c)), we hypothesize that it should be possible to grow c-BN NDs on other similar transition metal substrates including titanium (Ti), copper (Cu), etc.

Finally, we discuss the mechanism for seemingly chain-like alignment of NDs on the surfaces as seen from the SEM images in Figure 4.2. The Co foil substrates were not ideally flat with ridges and valleys across their surfaces (Figure 4.1). If we take the substrate rough surface morphology effect into account, for example, at concave surfaces where the atomic inter-distances of underneath metal substrate are relatively smaller

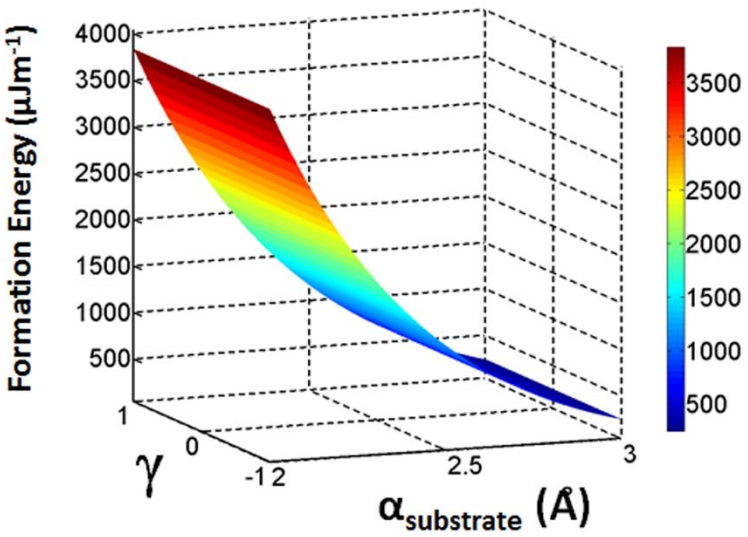

Figure 4.16. Three-dimensional (3D) plot of the total formation energy of a c-BN ND as a function of system parameter (γ) and substrate unit cell parameter ($\alpha_{substrate}$), assuming the ND is grown on top of a flat metal substrate with a contact angle of 135°.

compared to that of flat substrate surfaces, the lattice mismatch between the substrate and c-BN ND would be less, and hence, the formation energy would be much lower. Therefore, the concave substrate surfaces can act as preferential places for nucleation of c-BN NDs, leading to the chain-like alignment of NDs along the valleys. Using a similar analysis, we can reach an opposite situation for the formation of c-BN NDs on convex substrate surfaces.

4.4. Conclusion

We report self-assembled growth of c-BN NDs on Co and Ni metal substrates by plasma-assisted MBE. The cubic structure was confirmed by detecting the c-BN characteristic TO phonon mode in Raman spectra, (111) crystal plane diffraction peak in XRD pattern, and B1s and N1s signals in XPS results. The time evolution growth of c-BN NDs was observed using SEM and AFM characterizations, and the changes in their size distribution, alignment, density, and internal strain were carefully studied. It was concluded that the substrate (i.e., catalysis effect, lattice-mismatch-induced strain, and roughness), together with the growth conditions (i.e., the growth time and growth temperature) play a key role in the nucleation, formation, and morphological changes of c-BN NDs. The c-BN NDs with a density of $\sim 10^9$ cm^{-2} scale from 175 nm to 77 nm with the growth time. In addition, VW growth mode is responsible for the formation of c-BN NDs and the elastic strain energy is the dominant factor in determining the total formation energy of c-BN NDs on metal substrates. Self-assembly can lead to high-quality, pure, and ultrasmall c-BN NDs in the nanometer range that conventional high-temperature high-pressure methods were not

able to achieve, therefore this research paves a way to develop this new form of c-BN materials for a variety of novel applications such as catalysis, battery, biology, deep ultraviolet sensor, and optoelectronic technologies.

4.5. References:

[1] Samantaray C. B. and Singh R. N. Review of synthesis and properties of cubic boron nitride (c-BN) thin films. *Int. Mater. Rev.* **50** 313 (2005).

[2] Vel L., Demazeau G. and Etourneau J. Cubic boron nitride: synthesis, physicochemical properties and applications. *Mater. Sci. Eng. B* **10** 149 (1991).

[3] Tian Y. *et al.* Ultrahard nanotwinned cubic boron nitride. *Nature* **493** 385 (2013).

[4] Monteiro S. N., Skury A. L. D., de Azevedo M. G. and Bobrovnitchii G. S. Cubic boron nitride competing with diamond as a superhard engineering material–an overview. *J. Mater. Res. Technol.* **2** 68 (2013).

[5] Xu L., Li S., Zhang Y. and Zhai Y. Synthesis, properties and applications of nanoscale nitrides, borides and carbides. *Nanoscale* **4** 4900 (2012).

[6] Mohammad S. N. Electrical characteristics of thin film cubic boron nitride. *Solid-State Electron.* **46** 203 (2002).

[7] Mishima O., Tanaka J., Yamaoka S. and Fuknaga O. High-temperature cubic boron nitride pn junction diode made at high pressure. *Science* **238** 181 (1987).

[8] Kumar R. and Parashar A. Atomistic modeling of BN nanofillers for mechanical and thermal properties: a review. *Nanoscale* **8** 22 (2016).

[9] Ronning C., Feldermann H. and Hofsäss H. Growth, doping and applications of cubic boron nitride thin films. *Diamond Relat. Mater.* **9** 1767 (2000).

[10] Bello I. *et al.* Deposition of thick cubic boron nitride films: The route to practical applications. *Diamond Relat. Mater.* **14** 1154 (2005).

[11] Srivastava M. *et al.* Recent advances in graphene and its metal-oxide hybrid nanostructures for lithium-ion batteries. *Nanoscale* **7** 4820 (2015).

[12] Meyer N., Bekaert K., Pirson D., Devillers M. and Hermans S. Boron nitride as an alternative support of Pd catalysts for the selective oxidation of lactose. *Catal. Commun.* **29** 170 (2012).

[13] Lin L. *et al.* Fabrication and luminescence of monolayered boron nitride quantum dots. *Small* **10** 60 (2014).

[14] Liu G. et al. Submicron cubic boron nitride as hard as diamond. *Appl. Phys. Lett.* **106** 121901 (2016).

[15] Watanabe K., Taniguchi T. and Kanda H. Ultraviolet luminescence spectra of boron nitride single crystals grown under high pressure and high temperature. *Phys. Status Solidi A* **201** 2561 (2004).

[16] Huang J. Y. and Zhu Y. T. Atomic-scale structural investigations on the nucleation of cubic boron nitride from amorphous boron nitride under high pressures and temperatures. *Chem. Mater.* **14** 1873 (2002).

[17] Solozhenko V. L., Kurakevych O. O. and Le Godec Y. Creation of nanostuctures by extreme conditions: High-pressure synthesis of ultrahard nanocrystalline cubic boron nitride. *Adv. Mater.* **24** 1540 (2012).

[18] Wang J. B., Yang G. W., Zhang C. Y., Zhong X. L. and Ren Z. A. Cubic-BN nanocrystals synthesis by pulsed laser induced liquid–solid interfacial reaction. *Chem. Phys. Lett.* **367** 10 (2003).

[19] Liu H. *et al.* Photochemical synthesis of ultrafine cubic boron nitride nanoparticles under ambient conditions. *Angew. Chem.* **127** 7157 (2015).

[20] Hao X. P. *et al.* Synthesis of cubic boron nitride at low-temperature and low-pressure conditions. *Chem. Mater.* **13** 2457 (2001).

[21] Grzelczak M., Vermant J., Furst E. M. and Liz-Marzán L. M. Directed self-assembly of nanoparticles. *ACS Nano* **4** 3591 (2010).

[22] Zuo Z. *et al.* In-situ epitaxial growth of graphene/h-BN van der Waals heterostructures by molecular beam epitaxy. *Sci. Rep.* **5** 14760 (2015).

[23] Xu Z., Zheng R., Khanaki A., Zuo Z. and Liu J. Direct growth of graphene on in situ epitaxial hexagonal boron nitride flakes by plasma-assisted molecular beam epitaxy. *Appl. Phys. Lett.* **107** 213103 (2015).

[24] Xu Z. *et al.* Direct growth of hexagonal boron nitride/graphene heterostructures on cobalt foil substrates by plasma-assisted molecular beam epitaxy. *Appl. Phys. Lett.* **109** 043110 (2016).

[25] Xu Z. *et al.* Large-area growth of multi-layer hexagonal boron nitride on polished cobalt foils by plasma-assisted molecular beam epitaxy. *Sci. Rep.* **7** 43100 (2017).

[26] Zheng R. *et al.* Low-temperature growth of graphene on iron substrate by molecular beam epitaxy. *Thin Solid Films* **627** 39 (2017).

[27] Wang K. L., Cha D., Liu J. and Chen C. Ge/Si self-assembled quantum dots and their optoelectronic device applications. *Proc. IEEE* **95** 1866 (2007).

[28] Adelmann C. *et al.* Self-assembled InGaN quantum dots grown by molecular-beam epitaxy. *Appl. Phys. Lett.* **76** 1570 (2000).

[29] Huang, J. Y. and Zhu Y. T. Atomic-scale structural investigations on the nucleation of cubic boron nitride from amorphous boron nitride under high pressures and temperatures. *Chem. Mater.* **14** 1873 (2002).

[30] Mirkarimi P. B., McCarty K. F. and Medlin D. L. Review of advances in cubic boron nitride film synthesis. *Mater. Sci. Eng. R* **21.2** 47 (1997).

[31] Zhou Z. F. *et al.* Formation of cubic boron nitride films on nickel substrates. *Thin Solid Films* **368** 292 (2000).

[32] Reich S. *et al.* Resonant Raman scattering in cubic and hexagonal boron nitride. *Phys. Rev. B* **71** 205201 (2005).

[33] Werninghaus T., Hahn J., Richter F. and Zahn D. R. T. Raman spectroscopy investigation of size effects in cubic boron nitride. *Appl. Phys. Lett.* **70** 958 (1997).

[34] Zardo I. S. *et al.* Raman spectroscopy of wurtzite and zinc-blende GaAs nanowires: polarization dependence, selection rules, and strain effects. *Physical Review B* **80** 245324 (2009).

[35] Datchi F. and Canny, B. Raman spectrum of cubic boron nitride at high pressure and temperature. *Phys. Rev. B* **69** 144106 (2004).

[36] Viera G., Huet S. and Boufendi L. Crystal size and temperature measurements in nanostructured silicon using Raman spectroscopy. *J. Appl. Phys.* **90** 4175 (2001).

[37] Nakhaie S. *et al.* Synthesis of atomically thin hexagonal boron nitride films on nickel foils by molecular beam epitaxy. *Appl. Phys. Lett.* **106** 213108 (2015).

[38] Biesinger M. C. *et al.* Resolving surface chemical states in XPS analysis of first row transition metals, oxides and hydroxides: Cr, Mn, Fe, Co and Ni. *Appl. Surf. Sci.* **257** 2717 (2011).

[39] Alrehaily L. M., Joseph J. M., Biesinger M. C., Guzonas D. A. and Wren, J. C. Gamma-radiolysis-assisted cobalt oxide nanoparticle formation. *Phys. Chem. Chem. Phys.* **15** 1014 (2013).

[40] Huang L., Nicholas J., Kieffer J. and Bass J. Polyamorphic transitions in vitreous B_2O_3 under pressure. *J. Phys.: Condens. Matter* **20** 075107(2008).

[41] Arenal R. *et al.* Raman spectroscopy of single-wall boron nitride nanotubes. *Nano Lett.* **6** 1812 (2006).

[42] Tallant D. R., Aselage T. L., Campbell A. N. and Emin D. Boron carbide structure by Raman spectroscopy. *Phys Rev B.* **40** 5649 (1989).

[43] N. Xu *et al.* Raman spectra of nanocrystalline carbon nitride synthesized on cobalt-covered substrate by nitrogen-atom-beam-assisted pulsed laser ablation. *J. Appl. Phys.* **92** 496 (2002).

[44] Masa J. *et al.* Amorphous cobalt boride (Co_2B) as a highly efficient nonprecious catalyst for electrochemical water splitting: oxygen and hydrogen evolution. *Adv. Energy Mater.* **6** 1502313 (2016).

[45] Orofeo C. M., Suzuki S., Kageshima H. and Hibino H. Growth and low-energy electron microscopy characterization of monolayer hexagonal boron nitride on epitaxial cobalt. *Nano Res.* **6** 335 (2013).

[46] Nahm K. S., Kim T. Y. and Lee S. H. Catalytic effect of metal elements on the growth of GaN and Mg-doped GaN micro-crystals. *Korean J. Chem. Eng.* **20** 653 (2003).

[47] Miller D. M., Buettner G. R. and Aust, S. D. Transition metals as catalysts of "autoxidation" reactions. *Free Radical Biol. Med.* **8** 95 (1990).

[48] Tay, R. Y. *et al.* Growth of large single-crystalline two-dimensional boron nitride hexagons on electropolished copper. *Nano Lett.* **14** 839 (2014).

[49] Cimalla V., Zekentes K. and Vouroutzis N. Control of morphological transitions during heteroepitaxial island growth by reflection high-energy electron diffraction. *Mater. Sci. Eng. B* **88** 186 (2002).

[50] Barabási A. L. Thermodynamic and kinetic mechanisms in self-assembled quantum dot formation. *Mater. Sci. Eng. B* **67** 23 (1999).

[51] Jin G. *et al.* Controlled arrangement of self-organized Ge islands on patterned Si (001) substrates. *Appl. Phys. Lett.* **75** 2752 (1999).

[52] Zhang J., Brehm M., Grydlik M. and Schmidt O. G. Evolution of epitaxial semiconductor nanodots and nanowires from supersaturated wetting layers. *Chem. Soc. Rev.* **44** 26 (2015).

[53] Jin G., Liu J. L. and Wang K. L. Temperature effect on the formation of uniform self-assembled Ge dots. *Appl. Phys. Lett.* **83** 2847 (2003).

[54] Ren J., Hu H., Liu F., Chu S. and Liu J. Strain-less directed self-assembly of Si nanocrystals on patterned SiO_2 substrate. J. *Appl. Phys.* **112** 054311 (2012).

[55] Auwärter W., Suter H. U., Sachdev H. and Greber T. Synthesis of one monolayer of hexagonal boron nitride on Ni (111) from B-trichloroborazine $(ClBNH)_3$ *Chem. Mater.* **16** 343 (2004).

[56] Diebold U., Pan J. M. and Madey T. E. Growth mode of ultrathin copper overlayers on TiO_2 (110). *Phys. Rev. B* **47** 3868 (1993).

[57] Wu Y., Garfunkel E. and Madey T. E. Initial stages of Cu growth on ordered Al_2O_3 ultrathin films. *J. Vac. Sci. Technol. A* **14** 1662 (1996).

[58] Pang C. L., Raza H., Haycock S. A. and Thornton G. Growth of copper and palladium on α-Al_2O_3 (0001). *Surf. Sci.* **460** L510 (2000).

[59] Seel S. C. and Thompson C. V. Tensile stress generation during island coalescence for variable island-substrate contact angle. *J. Appl. Phys.* **93** 9038 (2003).

[60] Eaglesham D. J., Unterwald F. C. and Jacobson D. C. Growth morphology and the equilibrium shape: The role of ‘‘surfactants’’ in Ge/Si island formation. *Phys. Rev. Lett.* **70** 966 (1993).

[61] Zang K. *et al.* Revealing ultralarge and localized elastic lattice strains in Nb nanowires embedded in NiTi matrix. *Sci. Rep.* **5** 17530 (2015).

[62] Hiramatsu K. *et al.* The composition pulling effect in MOVPE grown InGaN on GaN and AlGaN and its TEM characterization. *MRS Internet J. Nitride Semicond. Res.* **2** 6 (1997).

[63] Lee D. N. Elastic properties of thin films of cubic system. *Thin Solid Films* **434** 183 (2003).

[64] Li Y. L., Hu S. Y., Liu Z. K. and Chen L. Q. Effect of substrate constraint on the stability and evolution of ferroelectric domain structures in thin films. *Acta Mater.* **50** 395 (2002).

[65] De Gennes, P. G. Wetting: statics and dynamics. *Rev. Mod. Phys.* **57** 827 (1985).

[66] Nicotra G. *et al*. Nucleation kinetics of Si quantum dots on SiO_2. *J. Appl. Phys*. **95** 2049 (2004).

[67] Liu, F. Self-assembly of three-dimensional metal islands: Nonstrained versus strained islands. *Phys. Rev. Lett.* **89** 246105 (2002).

[68] Spiesser A. Surface free energy of cubic boron nitride films deposited on nanodiamond. *J. Phys. Chem. C* **111** 12768 (2007).

[69] Jiang X., Philip J., Zhang W. J., Hess P. and Matsumoto S. Hardness and Young's modulus of high-quality cubic boron nitride films grown by chemical vapor deposition. *J. Appl. Phys.* **93** 1515 (2003).

Chapter 5: Summary

In summary, we discussed the molecular beam epitaxy growth and characterization of three types of low-dimensional materials, that is h-BN/G vertical heterostructure, 2D h-BN and c-BN NDs. Firstly, in Chapter 2, we performed a systematic study of the in-situ growth of vertical h-BN/G heterostructure on Co substrate via MBE method. We showed a continuous h-BN/G heterostructures can be formed at a substrate temperature of 850~900 ºC. We identified three different h-BN/G growth regions based on the amount of C in Co substrate and G growth mode/morphology: (1) where G network is formed only by precipitation during cooling process underneath the h-BN film; (2) where isothermal G growth occurs to form G islands partially covering the substrate, followed by further precipitation G growth, leading to a non-uniform h-BN/G structure; and (3) where a uniform h-BN/G heterostructure with a thin continuous h-BN and a thick continuous MG are formed from both isothermal G growth and precipitation. We found that the top h-BN film influences the morphology, thickness and quality of underneath G layers in h-BN/G samples of region 1. In addition, the h-BN growth is self-limited to a 1~2 nm thick film in all three regions, regardless of the underneath G thickness or morphology.

In Chapter 3, we showed that incorporation of interstitial C into heated Co substrate can also facilitate the growth of 2D h-BN and control its morphology in a MBE system. Indeed, by carburizing the Co substrate, we introduced a new growth parameter which can highly improve the growth reliability of 2D h-BN film. We achieved a high breakdown electric field of 12.5 MV/cm for a tri-layer continuous h-BN film. Using DFT calculations, we found out that the adsorption energies of B and N atoms are improved by the existence

of interstitial C atoms, resulting in a more reliable and controllable 2D crystal growth compared to the that on carbon-free Co samples.

Finally, in Chapter 4, we showed self-assembled growth of c-BN NDs on Co and Ni metal substrates by MBE. We confirmed the cubic structure of BN NDs by detecting the c-BN characteristic TO phonon mode in Raman spectra, (111) crystal plane diffraction peak in XRD pattern, and B1s and N1s signals in XPS spectra. We found out that the substrate conditions (i.e., catalysis effect, lattice-mismatch-induced strain, and roughness), as well as the growth conditions (i.e., the growth time and growth temperature) play a key role in the nucleation, formation, and morphological changes of c-BN NDs. The c-BN NDs with a density of $\sim 10^9$ cm^{-2} scale from 175 nm to 77 nm with the growth time. In addition, VW growth mode is responsible for the formation of c-BN NDs and the elastic strain energy is the dominant factor in determining the total formation energy of c-BN NDs on metal substrates.

Appendix

Publications:

[1] Zuo Z. Xu Z., Zheng R., **Khanaki A.**, Zheng J.-G. and Liu J. In-situ epitaxial growth of graphene/h-BN van der Waals heterostructures by molecular beam epitaxy. *Sci. Rep.* **5** 14760 (2015).

[2] Xu Z., Zheng R., **Khanaki**, **A.**, Zuo Z. and Liu J. Direct growth of graphene on in situ epitaxial hexagonal boron nitride flakes by plasma-assisted molecular beam epitaxy. *Appl. Phys. Lett.* **107** 213103 (2015).

[3] Xu Z., **Khanaki A.**, Tian H., Zheng R., Zheng J.-G. and Liu J. Direct growth of hexagonal boron nitride/graphene heterostructures on cobalt foil substrates by plasma-assisted molecular beam epitaxy. *Appl. Phys. Lett.* **109** 043110 (2016).

[4] Xu Z., Tian H., **Khanaki A.**, Zheng R., Suja M. and Liu J. Large-area growth of multi-layer hexagonal boron nitride on polished cobalt foils by plasma-assisted molecular beam epitaxy. *Sci. Rep.* **5** 43100 (2017).

[5] Zheng R., Xu Z., **Khanaki A.**, Tian H., Zuo Z. and Liu J. Low-temperature growth of graphene on iron substrate by molecular beam epitaxy. *Thin Solid Films* **627** 39 (2017).

[6] Zheng R., **Khanaki A.**, Cui. Y., Tian H., Xu Z. and Liu J. Precipitation growth of graphene under exfoliated hexagonal boron nitride to form heterostructures on cobalt substrate by molecular beam epitaxy. *Appl. Phys. Lett.* **111** 011903 (2017).

[7] **Khanaki A.**, Xu Z., Tian H., Zheng R., Zuo Z., Zheng J.-G. and Liu J. Self-assembled cubic boron nitride nanodots. *Sci Rep*. **7** 4087 (2017).

[8] **Khanaki A.**, Tian H., Xu Z., Zheng R., Cui Z., He Y., Yang J. and Liu J. Effect of high carbon incorporation in Co substrates on the epitaxy of hexagonal boron nitride/graphene heterostructures. *Accepted in Nanotechnology* (2017). https://doi.org/10.1088/1361-6528/aa9c58

[9] Tian H., **Khanaki A. (co-first author)**, Das P., Zheng R., He Y., Cui Z., Shi W., Xu Z., Lake R. and Liu, J. The role of carbon interstitials in transition metal substrates on controllable synthesis of high-quality large-area two-dimensional hexagonal boron nitride layers. *Under review in Nanoletter* (2017).